Magneto-inductive wave data communications systems

Christopher W. T. CHAN

St. Catherine's College

Supervised by Prof. Christopher J. STEVENS

Department of Engineering Science

University of Oxford

A thesis submitted for the degree of

Doctor of Philosophy

Hilary 2014

MAGNETO-INDUCTIVE WAVE DATA COMMUNICATIONS SYSTEMS

Christopher W. T. CHAN

St. Catherine's College

Thesis submitted for the degree of Doctor of Philosophy

Hilary 2014

ABSTRACT

Metamaterials display unusual electromagnetic properties, such as, a negative effective permeability and negative effective permittivity. This has sparked much interest due to possibility of negative refraction which was later confirmed by experiments.

The ability of magnetically coupled resonant circuits to display an effective permeability lead to the discovery of magneto-inductive waves. These waves are only supported on arrays of magnetically coupled resonant circuits. Research into magneto-inductive waves has been largely concentrated on their use in filters and their potential use in magnetic resonance imaging.

However, some work has proposed the use of magneto-inductive waveguides as a data transfer medium. This report builds on previous work which found that an optimum existed for terminal-waveguide coupling, and aims to investigate the application of magneto-inductive waves in data transfer systems.

A brief overview of the topic is given along with a description of the underlying characteristics. Factors that affect the capacity of magneto-inductive wave data transfer systems, such as inter element coupling, were identified. Two novel structures, both with the intent of increasing the bandwidth via different methods, are studied. One, by making a pseudo one-dimensional channel from a two-dimensional structure, and the other by using a dual-layer design to increase the coupling between adjacent elements. Both systems are modelled, using simple circuit theory and the impedance matrix method, and a comparison between simulated behaviour and experimental observation was made. There is discussion about the differences between experiment and simulation as well as their limitations.

Magneto-inductive wave data transfer systems are eventually expected to support multiple terminals and as previous research only considered two-terminal systems, an investigation into the response of a one- and two-dimensional system with a blocking terminal was undertaken. The system was modelled, again using simple circuit theory and the impedance matrix method, and simulation and experiment were compared. As a whole, the simulations showed good agreement with experiments, after some initial adjustments. Both one- and two-dimensional systems showed that their performance was not severely effected by a blocking terminal. This suggests that magneto-inductive waveguides could support more terminals.

ACKNOWLEDGEMENTS

The DPhil has been somewhat of a long struggle for myself, whilst I wish I could write something more cheerful here I wish it to serve as a reminder to myself of what I've come through and the many people that have helped me along the way. This has been a time filled with the happiest moments of my life, but also the saddest (and I'm sure future me will add "so far" on the end there). But one thing I can see is that I have spent too much time self-absorbed with my own emotions and many insecurities that I let many opportunities slip and I've not done myself justice nor have I done my best for those whom I love and have loved. For that I'm truly sorry.

The somewhat negative start shall now, hopefully, be countered by a more positive (yet probably with many melancholy) things to say. I am extremely fortunate that I can say that many many people have contributed greatly to not only my time during my DPhil, but also my life.

Firstly, I must thank the EPSRC for funding me during my DPhil, for otherwise this part of my life would've likely been very different for better or worse.

Then I must thank my mother and father, without their support and undying love I would not be here, I would not have got through university the first time, and I certainly would not have (hopefully) gotten through it the second time! Though we may not be most harmonious I'm glad of the evolution of our relationship and understanding of each other. To my brother, whom I love dearly, I must thank you for your time and understanding despite your limited time settling into your own life whilst having to listen to my troubles too. Whilst I know you wouldn't say it was necessary, I hope that I may repay that kindness one day.

There are many friends that I'm indebted to that I'd like to thank for the times we've shared at my greatest, and at my worst. Chris Chan—my friend by the same name—you've seen me at my happiest and my worst, always there for good "advice" (just get in the squat rack!) and contributed much to my life during my DPhil. Saul—one of my oldest friends, we've been through much in life all the way from school and even until now. Thank you for helping through some of the toughest times in my life. Tze—you've offered some wise words and very much made me feel less alone during my struggles. Yueyang—someone I've always respected, and it's been a pleasure to get to know you more in recent times despite going way back to school times! Thank you for being a "bro". Ben—literally my oldest friend, we've known each other for our whole lives (minus a few years!). It's been fun growing up together, and it'll be interesting to see how we grow old. Jee—all that table-football, the times we stayed up until some godforsaken hour in the morning talking about life. Pete—all the times we've shared during undergrad, we shall always remember that "there are no points for close." Tan—a good friend ever since I entered the office, being much more senior than myself, often offered your advice and many great times were had. 喜美—楽しい時間をありがとう！それて僕が作った料理を全部食べてくれありがとう! Pulcheria—even though we rarely talk, you always listen and everything feels the same. I'm sorry I don't do the same for you. Veronica—always cheerful and full of energy, never afraid to say some nonsense to lighten the mood. You have listened to many of my troubles and have never failed to cheer me up and clear my head. Emma—thank you for all the help you've given me, though I reckon I might still have those marks on my arm? Just kidding. Saff—thanks "plum" for being there when I really needed it. Scot—I only ever seem to talk to you when I'm having some trouble, you always help me out in times of need and I hope I get to repay the favour some day. Lewys—the many house projects we've

constructed, you got any more left? Cheers for being such a good mate/housemate/landlord, I hope the percentage of tweed increases as you progress through your career! Tim—the many computer game related conversations! And all the support through the tough times, you've been a true friend. 李越—很高兴认识了你，大家成为朋友，成为今天的我，我永远珍惜这段友谊。真的。 :') All the gym bros who helped me along my strength journey: Ali, "Bacon", Bailey, Ben, Big Jamie, Big John, Carlos, Danny, Dave, Dom, Elliot, Fraser, Freddie, Guy, Himmat, Ian, Jamie, James, Little John, Mark, Markus, Martin, Matt, Mike, Paul, Rich, Ross, Rossie, Scot, Shez, Stefan, Will. You've all helped me escape to a place where only one things matters: Do you even lift?

There were many more who have helped me along the way, some old, some new, I apologize for any oversight on my behalf.

Lastly, but definitely by no means least, I would like to thank my supervisor Prof. Chris Stevens, without whom this journey surely would not have started, nor without his endless enthusiasm, advice, and faith would I have managed to finish. Thank you for believing in my ability when I did not, and for clearing my mind and giving me direction when I could not.

Well, with all that aside, I guess I should now look to the future? There shall be many rocky roads ahead, of that I'm sure, but this time I shall traverse them unafraid of the outcome. So begins another journey, there are many uncertainties but if there is anything I'm sure of, it's that I'll meet many more great people ahead.

List of Acronyms

CCG Capacitor-Connected Grid

CMOS Complimentary Metal-Oxide Semiconductor

EAS electronic article surveillance

ESR equivalent series resistance

GPIB general purpose interface bus

ISO International Organization for Standardization

MCM Chip Stack Multi-chip Module

MI magneto-inductive

MRI magnetic resonance imaging

PCB printed circuit board

PVC Polyvinyl chloride

RF radio-frequency

RFID Radio-Frequency Identification

SiP System in Package

SNR signal-to-noise ratio

SRR split-ring resonator

UHF ultra high frequency

USB universal serial bus

VNA vector network analyser

CONTENTS

Abstract i

Acknowledgements ii

List of Acronyms iv

Contents v

1 Introduction 1

1.1 RFID: The precursor to contactless data transfer 4

2 The Beginning of Magneto-Inductive Waves 6

2.1 Metamaterial elements 6

2.2 Coupling Between Elements 8

2.3 Magneto-Inductive Waves 9

2.3.1 Two-Dimensional Magneto-Inductive Waves 13

2.3.2 Biperiodic Magneto-Inductive Waveguides 15

2.4 Capacity 19

3 Model Design 25

3.1 The Impedance Matrix 25

3.2 Terminals 28

3.2.1 Terminal Coupling Schemes 29

3.2.2 Terminal Modelling 31

3.2.3 Cable Modelling 34

3.2.4 Terminal Performance Assessment Method 41

4 Experiments and Analysis **46**

4.1 Element Characterization Methods 47

4.2 Square Element Conventional Magneto-Inductive Waveguide 53

4.2.1 Optimal Height 62

4.2.1.1 One-Dimensional Structures 63

4.2.1.2 Two-Dimensional Structures 69

4.2.1.3 Mobile Transmitter 70

4.2.1.4 Mobile Receiver 75

4.2.1.5 Mobile Transmitter and Receiver Comparisons 78

4.2.2 Terminal Blocking 83

4.2.2.1 One-Dimensional 83

4.2.2.2 Two-Dimensional 86

4.3 Bandwidth Expansion 91

4.3.1 Pseudo One-Dimensional Structure 92

4.3.1.1 Optimal Height 95

4.3.1.2 Comparison to Conventional One- and Two-Dimensional Structures 97

4.3.2 The Metamaterial “flower” 99

4.3.2.1 One-Dimensional 105

4.3.2.2 Two-Dimensional 107

5 Conclusions and Future Work **114**

Published Work **120**

A Flower Element Geometry **121**

Bibliography **123**

CHAPTER 1

INTRODUCTION

Most devices require internal physical electrical connections for the transfer of power and data. These connections are normally via a backbone with a mixture of soldered chips and connectors for peripheral devices, such as a motherboard in a personal computer. There has been a growing interest into chip stacking as a means to pack more functions or performance into a single package whilst reducing footprint. This is often known as System in Package (SiP) or Chip Stack Multi-chip Module (MCM). This has the advantage of reducing the package pin count, decreasing chip-to-chip distance and simplifying board design. The stacked chips are generally connected using wire bonds or solder bumps. However, these methods can be impractical if there are many connections to be made, either due to the complexity of the interconnection or the physical space required for the interconnects. There has been an increasing amount of interest in contactless inter-chip connections; the claimed advantages over wired methods are that of power, speed and cost [1]. These attempts have used either inductive [2, 3] or capacitive coupling [4–7]. However these methods only allow the transfer of data, and not power.

There have been prior attempts of wireless power transfer [8–17] and of the wireless transfer of both power and data [15, 18–20]. Apart from the work done by Tesla [8] and Vanderelli et al. [14], the other efforts have been by a form of magnetic induction; of these, [9, 10, 18–20] are limited in the placement of the two terminals to be coupled. Yuan et al. [15] successfully

implemented a 10% efficient wireless chip-to-chip power transfer system in 0.18 μm Complimentary Metal-Oxide Semiconductor (CMOS). Kurs et al. [16] and Karalis et al. [17] utilize resonant induction and both claim to be capable of efficient non-radiative "mid-range" power transfer[1]. The latter bearing most similarity to the type of system under investigation in this report due to its consideration of capacitively-loaded conducting-wire loops.

In 2010 a paper was published concerning the use of similarly capacitively-loaded loops as a means of contactless proximity data transfer and, potentially, power transfer [21]. These capacitively-loaded loops were placed in close proximity to each other such that each element magnetically coupled to its neighbours and thus allowed for the propagation of magneto-inductive (MI) waves [22]. This forms what is known as a metamaterial, an artificial media with unusual electromagnetic properties [23]. A data capacity of ≈60 Mb/s was determined from experiments with a signal-to-noise ratio (SNR) of 10^4 with 79% of the source power reaching the receiver using a ten-element one-dimensional magneto-inductive waveguide. However it was noted that higher capacities were possible and this compares favourably to existing contactless data transfer such as NFC which displays a capacity of 424 kb/s. With these, it could be possible to implement a two-dimensional MI waveguide as a form of wireless backbone for multiple terminals as shown in Figure 1.1.

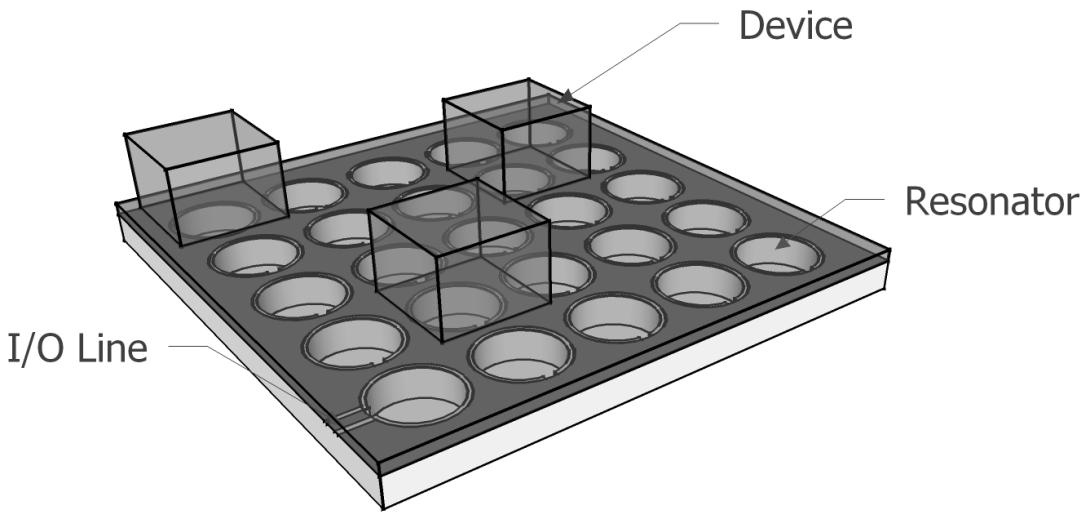


Figure 1.1 – An example system with three devices communicating through a two dimensional metamaterial array.

[1]Kurs states that by midrange he means "that the sizes of the devices that participate in the power transfer are smaller than the distance between devices by a factor of at least 2 to 3".

Whilst the current experimentally derived data rates may be comparable to some current wireless schemes, but not as high as those achievable in [1, 2, 5–7], these MI waveguides could offer a different advantage. Capacitive chip-to-chip coupling methods generally offer a higher data rate than inductive methods, as it's possible to have a higher interconnect density with less cross-talk than if implemented via inductive methods. This is due to, in part, by the nature of inductive and capacitive coupling, but also because the transmit and receive pads, in a capacitive coupling system, are smaller than the planar coils required for inductive chip-to-chip coupling. However, capacitive coupling methods require more precise alignment [24] than inductive coupling methods [25] and typically work at much closer distances. It should be noted that a single set of chip-to-chip capacitive links can only exist between two chips as the interconnect pads must be sufficiently close to each other, and that inductive links, whilst more chips could be daisy-chained on top, have also only been between two chips; a magneto-inductive waveguide could act as a bus between a stack of chips as it supports a wave-mode, rather than pure inductive coupling.

There also exists a novel structure referred to as the Capacitor-Connected Grid (CCG) [26–28], which bears similarity to the MI waveguide in structure, however the elements are not only coupled to their neighbours magnetically, but also capacitively.

This work studies the potential of these MI waveguides to act as data transfer channels with multiple terminals, in a fashion as depicted by Figure 1.1. The behaviour of two-dimensional MI waveguides with different terminal placements is investigated; the effect of a third "blocking" terminal upon the transmission between two terminals is also considered for both one- and two-dimensional MI waveguides. A novel structure that greatly improves upon the existing bandwidth of two-dimensional MI waveguides by increasing the inter-element coupling is also presented.

1.1 RFID: THE PRECURSOR TO CONTACTLESS DATA TRANSFER

Near-field contactless communication, arguably, started off with Radio-Frequency Identification (RFID) which, some say, originated from the concept of communicating via reflected power [29] which Stockman investigated in 1948 [30]. Stockman states that radar essentially behaves as a type of "on-off" modulation where only the presence of an object can be detected. Therefore, he modulated an incident microwave by physically rotating a corner reflector, thus controlling the amount of power reflected back to the source. One of the earliest RFID systems used so-called '1-bit' tags [31], where only the presence of a tag could be detected. Such technology found widespread commercial use in electronic article surveillance (EAS) equipment to counter theft. These tags rely on receiving an incoming signal and modifying it internally rather than by modulating the signal due to their physical geometry. These 1-bit tags operated in numerous ways but usually only exploited simple physical effects such as: oscillation stimulation, generation of harmonics or sub-harmonics, or by utilizing the non-linear hysteresis curve of metals or alloys.

RFID systems are always comprised of a reader and a transponder; the reader, depending on the system, is a read or write/read device, and the transponder is the device to be read. The transponder may contain either memory or a microprocessor for more security sensitive applications.

The various ranges of RFID systems can be placed into three main categories:

- *Close coupling*: Typically within 1 cm.
- *Remote coupling*: Ranges upto 1 m; always based upon magnetic coupling between reader and transponder. 90–95% of all RFID systems purchased are inductively coupled systems [31].
- *Long range*: Typically between 1–10 m, in most systems of this kind, the power supplied is not enough to operate the transponder so an auxiliary battery is required.

In close coupling systems the transponder is often placed into the reader, whereby the reader can supply the transponder with power via inductive coupling. Data transfer can also take place by load modulation of an induced carrier or by capacitive coupling.

In remote coupling systems the transponder is powered by inductive coupling to the reader alone, and data transfer takes place by load modulation or by the generation and modulation of a sub-harmonic.

Long range systems typically operate in ultra high frequency (UHF) or microwave frequencies and operate on the principle of electromagnetic backscatter.

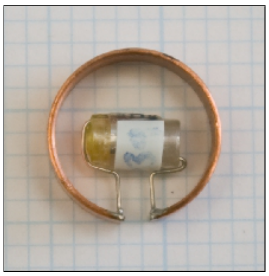
CHAPTER 2

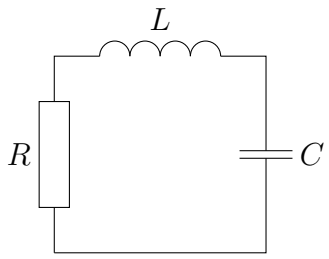
THE BEGINNING OF MAGNETO-INDUCTIVE WAVES

It is the ability of some metamaterials to display a μ_{eff} that is important to the discovery of MI waves. Wiltshire et al. [32] used a structure of hexagonally close-packed "Swiss rolls" as a flux-guiding medium in a magnetic resonance imaging (MRI) system. A MRI machine creates a constant homogeneous magnetic field which conventional magnetic materials would disturb; however, a metamaterial has a frequency dependent μ_{eff} close to unity at dc. Shamonina et al. [22] suggested that this densely packed structure may not be the best solution and that one consisting of a linear periodic array of magnetically-coupled elements would also suffice, if its purpose was to guide a magnetic field at a particular frequency. Shamonina et al. had decided to dub this array the "magneto-inductive waveguide".

2.1 METAMATERIAL ELEMENTS

The magneto-inductive waveguide is a magnetic metamaterial which is comprised of magnetically coupled resonant circuits. Figure 2.1 gives an example of a resonant circuit and its circuit equivalent. These elements are similar to 1-bit RFID tags that make use of resonance, briefly





(a) (b)

Figure 2.1 – A resonant element, the capacitvely-loaded split ring [33], a type of split-ring resonator (SRR) (a), made from a section of copper pipe with a polyester capacitor soldered across a sawn gap and its circuit diagram (b).

mentioned in Section 1. The forerunners to these elements are the SRR [34] and the Loop-Gap Resonator [35], the main difference between the aforementioned elements and the capacitively-loaded split ring, shown in Figure 2.1a, is that their capacitance is determined by the size of that gap rather than a physical element. It is worth noting that while most designs of SRR are circular, this does not have to be the case. Also, SRRs are not the only example of magnetic metamaterial elements, others include, but are not exclusive to, the swiss roll [32], the twin-split ring [36], and the singly-split double ring [37]. The SRR can usually be represented as a resonant LCR circuit as shown in Figure 2.1b. These are parametrized by L, the inductance, C, the capacitance, and R, the resistance. Two other important characteristics are the resonator's resonant frequency, ω_0 (angular frequency) and quality factor, Q:

$$\omega_0 = \frac{1}{\sqrt{LC}}, \tag{2.1}$$

$$Q = \frac{1}{\omega_0 CR}. \tag{2.2}$$

As these are reliant on the circuit parameters L, C, and R, one can determine these by design or through experimentation. When a voltage, $V(t)$, is induced externally, this excites current I in the element given by Kirchoff's law as

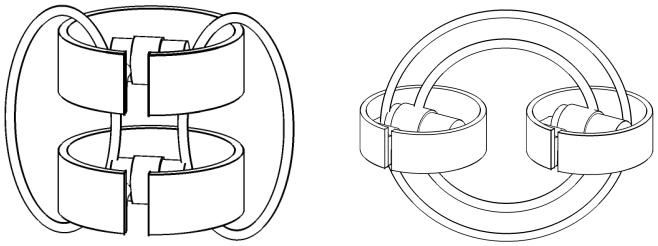
$$V(t) = RI + \frac{1}{C}\int I\,\mathrm{dt} + L\frac{\mathrm{d}I}{\mathrm{dt}}. \tag{2.3}$$

Thus the frequency depedent impedance of an element can be given by

$$Z(\omega) = R + \frac{1}{j\omega C} + j\omega L. \tag{2.4}$$

2.2 COUPLING BETWEEN ELEMENTS

The interaction between two metamaterial elements is key to the MI waveguide. Consider the cases displayed in Figure 2.2:



(a) *(b)*

Figure 2.2 – Two resonators magnetically coupled in the axial (a), and in the planar (b), configurations.

The current in one element generates a magnetic field and as this field passes through a neighbouring element, a voltage is induced to it. Thus the voltage of one element is dependent on the current in the other. This coupling between two elements is given the name mutual inductance, M, and is defined as

$$M = \frac{\mu_0}{4\pi} \oint_{element\,1} \oint_{element\,2} \frac{\mathbf{ds_1}.\mathbf{ds_2}}{|\mathbf{R_{12}}|}, \tag{2.5}$$

where $\mathbf{ds_{1,2}}$ are the current elements in each resonator and $\mathbf{R_{12}}$ is the vector between those current elements. Though not entirely obvious from (2.5) the value of mutual inductance in Figure 2.2b would be negative. This is because the flux crosses the plane of each resonator in opposite directions, but the current in each element would be in the same direction. This is in contrast to the axial case as depicted by Figure 2.2a where the flux lines cross both elements in

the same direction, but the currents flow in opposing directions, giving rise to positive mutual inductance. With this in mind, one can express the voltage-current relationship between two elements as:

$$\begin{cases} V_1 = ZI_1 + j\omega MI_2 \\ V_2 = j\omega MI_1 + ZI_1 \end{cases}, \tag{2.6}$$

$$\begin{pmatrix} V_1 \\ V_2 \end{pmatrix} = \begin{pmatrix} Z & j\omega M \\ j\omega M & Z \end{pmatrix} \begin{pmatrix} I_1 \\ I_2 \end{pmatrix}, \tag{2.7}$$

where the subscripts indicate the element the respective parameters belongs to. When this voltage-current relationship is expressed in a vector-matrix format as in (2.7); it can be seen that the determinant of the impedance matrix, $\boldsymbol{Z}$, has two eigenvalues (2.8) which indicates that there will be two resonances in the system

$$\lambda_{1,2} = Z \pm j\omega M. \tag{2.8}$$

Bearing in mind that resonance occurs when the impedance is at its minimum or at minima, then by substituting (2.1) and (2.4) into (2.8), one can determine at what frequencies these resonances occur, given by

$$\omega_{1,2} = \frac{\omega_0}{\sqrt{1 \pm \frac{M}{L}}}. \tag{2.9}$$

2.3 MAGNETO-INDUCTIVE WAVES

Mathematically, the solution for a system with an infinite number of degrees of freedom is a travelling wave, and in the case of magnetically coupled metamaterials this is termed a MI wave [22, 38, 39]. When considering an infinite number of elements that are coupled to their nearest neighbour in a one dimensional strip, the current in the n^{th} element is given by:

$$I_n = I_0 \mathrm{e}^{-jkdn}, \tag{2.10}$$

where d is the strip period (the spacing between elements) and k is the wave number, and is given by:

$$k = \beta - j\alpha, \tag{2.11}$$

where β is the propagation constant and α, the attenuation constant. Writing (2.3) with nearest-neighbour couplings gives the voltage-current relationship in the n^{th} element as:

$$0 = (R + \frac{1}{j\omega C} + j\omega L)I_n + j\omega M(I_{n-1} + I_{n+1}). \tag{2.12}$$

Substituting (2.1), (2.2) and (2.10) into (2.12) gives the dispersion equation:

$$1 - \frac{j}{Q}\frac{\omega_0}{\omega} - \frac{\omega_0^2}{\omega^2} + \kappa\cos(kd) = 0. \tag{2.13}$$

Thus k, the wave number is:

$$k = \beta - j\alpha = \frac{1}{d}\cos^{-1}\left(\frac{1}{\kappa}\left(\frac{\omega_0^2}{\omega^2} + \frac{j}{Q}\frac{\omega_0}{\omega} - 1\right)\right), \tag{2.14}$$

where κ is the coupling constant given by:

$$\kappa = \frac{2M}{L}. \tag{2.15}$$

However it is worth noting that in the literature [22, 38] and [39] ω_0/ω has been omitted. This is due to the fact that, in general, the frequencies of interest are near enough to ω_0 such that $\omega_0/\omega \approx 1$, but has been included here for mathematical accuracy. Figures 2.3c and 2.3d give examples of typical dispersion curves for axial and planar one-dimensional MI waveguides respectively.

By representing the dispersion equation given by (2.13) in Figures 2.3c and 2.3d, for axial and planar one-dimensional MI waveguides respectively, it can be seen that MI waves only propagate in a pass band around ω_0 given by:

$$\frac{1}{\sqrt{1+|\kappa|}} < \frac{\omega}{\omega_0} < \frac{1}{\sqrt{1-|\kappa|}}. \tag{2.16}$$

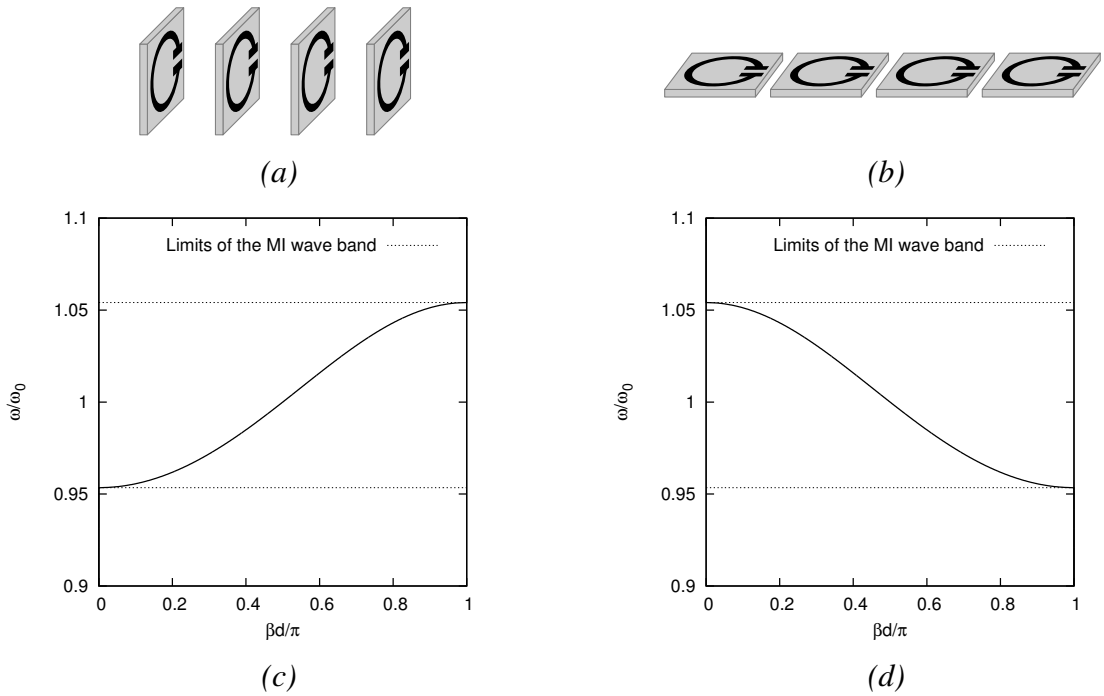


Figure 2.3 – Examples of an axial (a), and planar (b), one-dimensional MI waveguides. Typical dispersion curves for lossless infinite axial (c), and planar (d), one-dimensional MI waveguides where $|\kappa|$ is 0.1.

It can be seen from Figures 2.3c and 2.3db that MI waves are dispersive and as such, the group velocity, v_g, is frequency dependent and given by

$$v_g = \frac{\partial \omega}{\partial \beta}. \tag{2.17}$$

Another important feature of MI waves is that the type of propagated wave is dependent on the sign of the coupling constant [39]. This is evident from the slopes of the graphs in Figure 2.3, where the axially positively coupled strips support forward waves, while the planar negatively coupled strips support backward waves.

Real-world waveguides, of course, are finite. To allow waves in the form of (2.10), the waveguide should be terminated in the appropriate matching impedance. If only nearest neighbours are considered then this matching impedance is given by [38]

$$Z_T = j\omega M \mathrm{e}^{-jkd}. \tag{2.18}$$

This needs to be incorporated into the last element of the strip to make the voltage-current

relationship of the last element

$$0 = (Z + Z_T)I_n + j\omega M(I_{n-1}). \tag{2.19}$$

Unfortunately Z_T is frequency dependent and difficult to fabricate. Syms et al. developed a method to suppress these reflections by leading the wave into a graded absorber [40]. They realized that at $\omega = \omega_0$ that the ideal termination is resistive and Z_T becomes

$$Z_T = \omega_0 M. \tag{2.20}$$

However they noted that using single element termination was not sufficient to suppress reflection at the MI pass band edges; thus Syms et al. went on to investigate double element and multi-element termination and developed the geometrically graded resistive termination. Unfortunately (2.20) is negative for coplanar waveguides.

As metamaterials are being used as a transmissive media there has been research into the characterization of metamaterials. This has led to the dispersion equations [22, 38], though only the nearest neighbour coupling dispersion equation was shown in Section 2.3. This was experimentally verified by Wiltshire et al. for the nearest neighbour [41] and by Syms et al. for higher order interactions [42]. Shamonina et al. [38] give the dispersion equation as

$$\frac{\omega_0^2}{\omega^2} - 1 + \frac{j}{Q} = \sum_{s=1}^{u} \kappa_s \cos(skd), \tag{2.21}$$

where u is the number of neighbour couplings to take into account (with u=1 being nearest neighbour coupling), κ_s is $2M_s/L$ where M_s is the mutual inductance between two loops that are a distance sd from each other, d is the element period and k is the wavenumber. Syms et al. concluded that, in general, higher-order interactions may not be neglected for axially coupled resonant elements, though in the case of weak coupling [43], only taking into account nearest neighbour interactions is sufficient.

2.3.1 TWO-DIMENSIONAL MAGNETO-INDUCTIVE WAVES

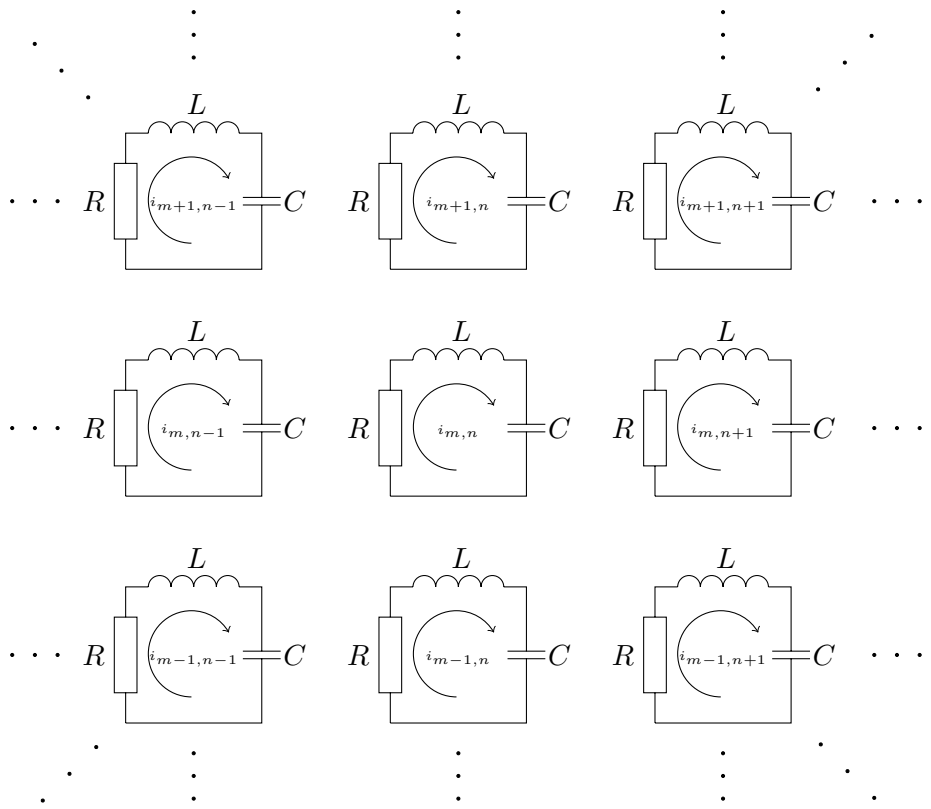


Figure 2.4 – Equivalent electrical circuit of an infinite two-dimensional magneto-inductive waveguide, where the equivalent circuit elements of inductance L, capacitance C, and resistance R are labelled. Coupling terms are omitted for clarity.

The dispersion equation for two-dimensional MI waveguides is not too different from that of one-dimensional waveguides, however evidently there are going to be waves in the x and y directions. Therefore, the wavenumber will be comprised of components in the x and y directions represented as k_x and k_y. As in (2.11), the wavenumber is composed of a propagation constant and attenuation constant. By looking at Figure 2.4, it can be seen that the voltage-current relationship in the element in the m^{th} row and n^{th} column, when only considering nearest neighbour coupling and assuming the same period d and coupling M in the x and y directions, would be given by

$$0 = ZI_{m,n} + j\omega M \left(I_{m,n-1} + I_{m-1,n} + I_{m+1,n} + I_{m,n+1}\right). \tag{2.22}$$

The form of the current in the m^{th},n^{th} element is taken to be of the form

$$I_{m,n} = I_0 \mathrm{e}^{(-jk_x dn - jk_y dm)}. \tag{2.23}$$

When (2.23) is substituted into (2.22), this will yield the dispersion equation [38, 44]

$$\frac{\omega_0^2}{\omega^2} + \frac{j}{Q}\frac{\omega_0}{\omega} - 1 = \kappa \left(\cos(k_x d) + \cos(k_y d)\right). \tag{2.24}$$

It is worth noting, given that κ and d are the same in both the x and y directions, that the bandwidth is effectively doubled in comparison to the one-dimensional waveguide giving [38]

$$\frac{1}{\sqrt{1+2|\kappa|}} < \frac{\omega}{\omega_0} < \frac{1}{\sqrt{1-2|\kappa|}}. \tag{2.25}$$

Figure 2.5 shows typical dispersion surfaces for lossless two-dimensional MI waveguides with positive coupling (Figure 2.5a), as would be the case in the novel structure presented in Section 4.3.2, and negative coupling (Figure 2.5b), displayed in a conventional MI waveguide such as the square element MI waveguide in Section 4.2.

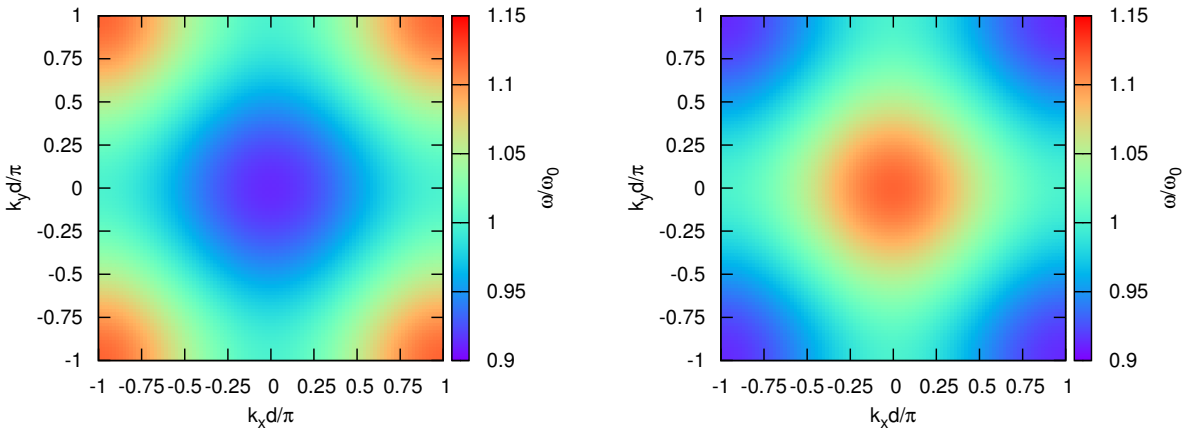
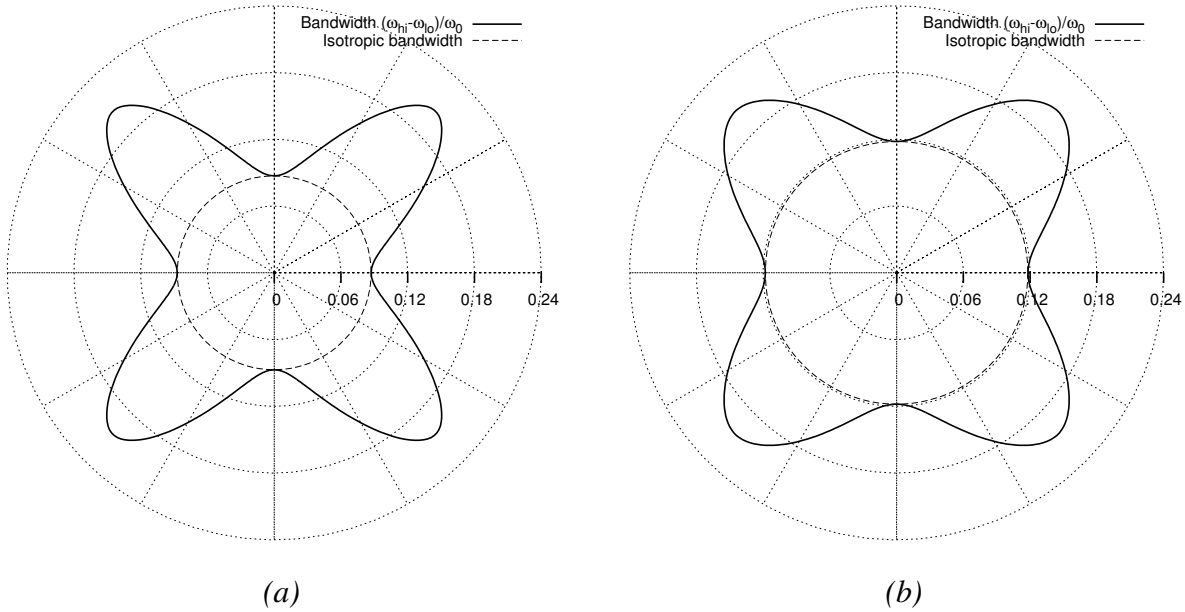


Figure 2.5 – Generic dispersion surfaces for lossless two-dimensional MI waveguides with $\kappa = 0.1$, (a), and $\kappa = -0.1$, (b).

Something noticeable in both Figure 2.5a and 2.5b, is that the relative frequency, ω/ω_0, varies along the perimeter of the figures. This is due (2.24) being composed of components in the x and y directions. This leads a bandwidth that varies with angle and Figure 2.6 shows this

variation.

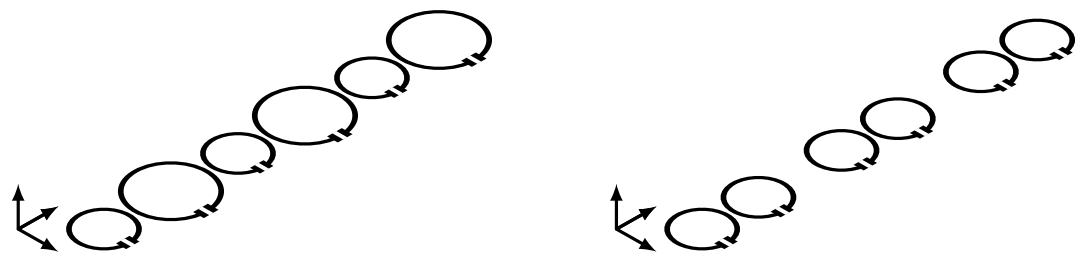


(a) *(b)*

Figure 2.6 – The bandwidth relative to ω_0 and angle for a two-dimensional MI waveguide with a κ of 0.1, (a), and -0.1, (b).

2.3.2 BIPERIODIC MAGNETO-INDUCTIVE WAVEGUIDES

Sydoruk et al. [45] investigated the potential of bi-periodic one dimensional arrays to widen the response of MI wave supporting metamaterials. This involved an array whereby there were two types of elements with different characteristics, or the distance between elements was varied; examples are given in Figure 2.7.



(a) *(b)*

Figure 2.7 – Examples of bi-periodic coplanar one-dimensional arrays with varied element size leading to varied resonant frequencies (a), and varied distance (b).

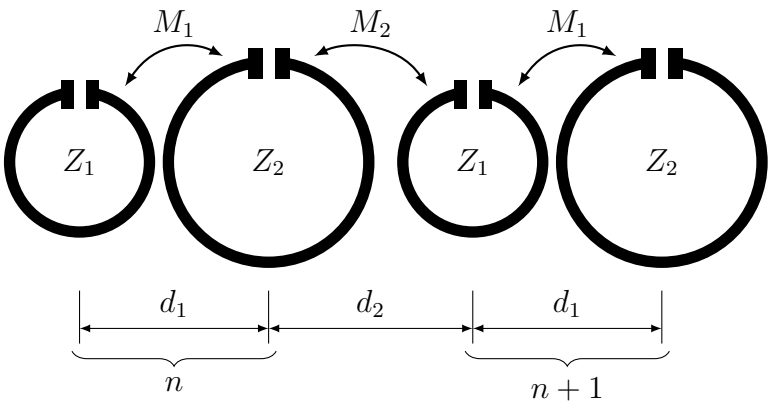


Figure 2.8 – Diagram demonstrating the layout of a bi-periodic coplanar one-dimensional array. $Z_{1,2}$ are the impedances of the elements, M_1 is the mutual inductance between elements of type 1 and 2 over the distance d_1, M_2 is the mutual inductance between elements of type 1 and 2 over the distance d_2 where the first two elements and last two elements are the n^{th} and $(n+1)^{th}$ cells respectively.

The dispersion equation for bi-periodic structures is a little harder to derive but it is still possible. Using the nomenclature shown in Figure 2.8 and using I and J to denote the currents in elements of the first and second type respectively, the voltage-current relationships for the n^{th} cell are given by

$$\begin{array}{l} Z_1 I_n + j\omega(M_1 J_n + M_2 J_{n-1}) = V_n^1 \\ Z_2 J_n + j\omega(M_1 I_n + M_2 I_{n+1}) = V_n^2 \end{array} . \tag{2.26}$$

Again, just as in Section 2.3 the solution is assumed to be in the form of a propagating wave; thus currents of the elements in the n^{th} cell are of a similar form to (2.10) and are given by

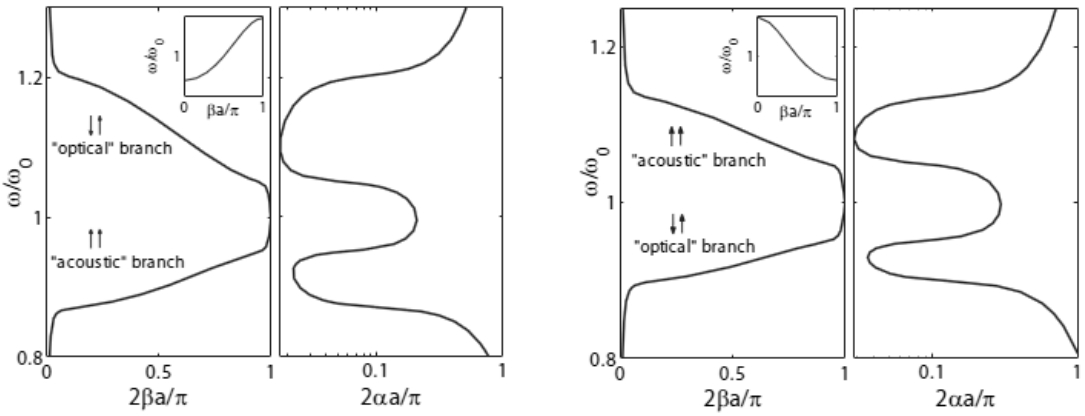
$$\begin{array}{l} I_n = I_0 \exp(-jk(d_1+d_2)n) \\ J_n = J_0 \exp(-jk(d_1+d_2)n - jkd_1) \end{array} , \tag{2.27}$$

$$\begin{array}{l} Z_1 I_0 + j\omega J_0(M_1 e^{-jkd_1} + M_2 e^{jkd_2}) = 0 \\ Z_2 J_0 + j\omega I_0(M_1 e^{jkd_1} + M_2 e^{-jkd_2}) = 0 \end{array} . \tag{2.28}$$

Where the $-jkd_1$ term in the exponential of J_n arises because the wave originated from the first element of the first cell, and V_n^1 and V_n^2 are zero due to Kirchhoff's voltage law. Substituting (2.27) into (2.26) leads to the intermediate step, (2.28) found in [39], before leading to the dispersion equation given by (2.29), and the curves in Figure 2.9, for biperiodic structures given

in [45]. These were later experimentally verified by Radkovskaya et al. [46] for the case where the element characteristics are varied by changing the value of the split ring loading capacitor.

$$\cos k\frac{d_1+d_2}{2} = \pm\frac{1}{2\sqrt{M_1M_2}}\sqrt{-\frac{Z_1Z_2}{\omega^2}-(M_1-M_2)^2}. \tag{2.29}$$

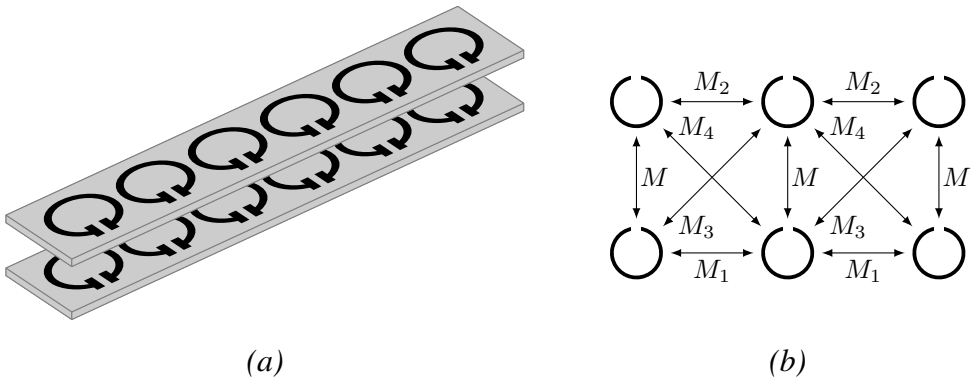


(a) *(b)*

Figure 2.9 – Dispersion curves for the bi-periodic axial (a), and planar (b), configurations using loops with the following parameters: radius 10 mm, wire thickness 2 mm, $L = 33$ nH, $C_1 = 208$ pF, $C_2 = 177$ pF. The resonant frequencies of the element of the first and second type are $0.95\omega_0$ and $1.05\omega_0$ respectively where ω_0 is 63.78 MHz. For the axial case $d_1 = d_2 = a = 10$ mm ($M/L = 0.149$) and $d_1 = d_2 = a = 20.5$ mm ($M/L = -0.104$) for the coplanar case. Currents within a cell are in anti-phase in the "optical" branch and in-phase for the "acoustic" branch. Inset figures are the dispersion curves of arrays with identical elements as seen in Figure 2.3. The labelling of the "optical" and "acoustic" branches is due to Sydoruk's analogy of MI waves to acoustic waves in solids. Taken from [45].

Another example of bi-periodic metamaterials, are bi-atomic metamaterials which have two elements per unit cell. One of the more simpler cases to imagine would be that of two coupled waveguides as shown in Figure 2.10a, and their coupling regime shown in Figure 2.10b.

These coupled waveguides don't necessarily have to be two planar waveguides with their centres aligned, Sydoruk et al. [47] explored the dispersion characteristics of two planar waveguides coupled together at differing vertical separations and with no shift and half a period of horizontal shift (as both lines were identical), and also that of a planar and axial waveguide coupled together varied in the same way. Figure 2.11 gives examples of the various layouts explored.



(a) *(b)*

Figure 2.10 – Example of coupled planar waveguides with element centres aligned (a), and their coupling regime (b).



(a) *(b)*

Figure 2.11 – Example of shifted planar-planar waveguides and shifted planar-axial waveguides.

The various ways in which two waveguides can be arranged means that the dispersion curves can be manipulated. Interestingly, when two identical planar waveguides are coupled together vertically, there is a maximum in the transmission when they are shifted by half a period horizontally, and a minimum when they are unshifted [48]. This characteristic could be particularly useful in power transfer.

The same two identical vertically coupled unshifted planar waveguides can also act as a magnetic lens. The two waveguides effectively have the same dispersion curves, but as a collective, when weakly coupled, will appear to exhibit a larger passband. When strongly coupled, two passbands appear, with a stop band in between them. This structure images the best during the stop band, as MI waves cannot propagate along the waveguides. This has been studied by Sydoruk et al. who also deemed imaging was best with a double layer, rather than a single layer MI waveguide [49]. This was because the magnetic field amplitude from a double layer magnetic lens was greater than that of a single layer, despite the similar contrast ratio.

2.4 CAPACITY

What is of interest for the system is the channel capacity and is given by

$$C = \int_B \log_2(1 + T \times SNR)\mathrm{d}B, \tag{2.30}$$

where the integral is performed over the bandwidth B, T is the transfer function, and SNR is the mean signal-to-noise ratio, referenced to the transmitter. Traditionally, the SNR is taken at the receiver (SNR_{out}), however as the noise power is unknown, by assuming a particular SNR at the transmitter (SNR_{in}) and multiplying by T, and by assuming the noise power is the same at both the transmitter and receiver, thus making $T \times SNR_{in}$ equal to SNR_{out}. In experiments, the transfer is given by the forward voltage gain (s_{21}) measured by the vector network analyser (VNA); in the simulations this is taken to be the square root of the power ratio: $\sqrt{P_{out}/P_{in}}$ where P_{out}, is the power out and P_{in}, the power in. This is because some cases are treated as 2-port networks. When these 2-port sections are cascaded, their overall s_{21} may be calculated by multiplying the s_{21} of each stage; though only if the reflections at each stage are negligible. This is not true in this case as the sections are not matched and so $\sqrt{P_{out}/P_{in}}$ must be used.

The SNR must also be known in order to calculate the capacity of the system. Predominantly, natural noise in analogue communications will take two forms; thermal noise and shot noise. Shot noise arises in semiconductors across p-n junctions and occurs because current flows across the junction in discrete quanta. As such, this is not a consideration for MI data transfer systems as they do not contain semiconductors. Thermal noise, however, is caused by the random motion of charged particles due to heat excitation inside an electrical conductor and happens regardless of any applied voltage. The effect of this noise is investigated by Stevens et al. [21] in a system utilizing a set of ten elements with a resonant frequency of 46 MHz. In this system, with an inter-element κ of -0.125 and with a 6 MHz bandwidth the thermal noise was only 46 pW.

Reduction of the SNR could also be caused by radio-frequency (RF) interference. However, this would have to be in the form of magnetic flux with sufficient coupling to the system to make an impact. It would also only apply to signals produced within the MI pass band given by (2.16) and (2.25) for one and two dimensional cases respectively.

Capacity is most likely to be affected by the properties of the elements themselves and by the appropriate coupling of terminals to the waveguide. The resonators have to be fabricated and, as such, are subject to the tolerances of manufacturing. A most obvious example would be the tolerances on discrete components. However, one could simply make numerous resonantors and hand-pick a selection with parameters given a desired tolerance; the alternative is to model the tolerance [38]. This is done by assuming the capacitance of an element to vary randomly leading to a variation of the resonant frequency of individual elements, and is given by

$$C = C_0(1 + r\delta), \tag{2.31}$$

where C_0 is the nominal capacitance, r is a random number between ± 1, and δ is the tolerance. Capacitor tolerances for the types of capacitor used in making these resonators is usually of the order of 5%. The effect of this in [38] was deemed to be quite moderate, a decline from 77% to 70% power transfer over a 21 element axially-coupled line. The resonators used had the following circuit parameters: $L = 33$ nH, $C = 187$ pF, $R = 20.5$ mΩ, $M_1/L = 0.149$, $M_2/L = 0.043$, $M_3/L = 0.0176$, $M_4/L = 0.0088$, and $M_5/L = 0.0042$. The terms M_{1-5}/L are the coupling terms of the first to fifth neighbours. A lower power transfer equates to a lower capacity, as this means that the transfer function T in equation (2.30) is reduced. It's conceivable that the inductance of individual elements could vary, however, element inductance is usually determined by the element's geometry. This depends on the method of constructing the elements, and most methods used do not lead to a significant variation from the desired shape given the scale of the majority of MI wave elements.

Another factor affecting channel capacity is the MI waveguide attenuation. For one di-

mensional strips, Stevens et al. [21] give the mid-band attenuation as

$$\alpha(\omega) = \frac{1}{d} \ln \left(\frac{1}{\kappa Q} + \sqrt{1 + \frac{1}{\kappa Q}} \right), \tag{2.32}$$

where Q and κ are defined in equations (2.2) and (2.15). It is evident that attenuation is minimized when κQ is maximized. There is little control over Q as both ω_0 and C are chosen, leaving only the element resistance, R, as a potential variable. However, the value of R is hard to determine analytically. The values determined by considering element resistance or the skin effect offer overestimates of the measured Q (and thus underestimates of R). Other factors that affect R are the loss tangent of the capacitor and solder joint resistance, if present. By far the easiest solution is to maximize the coupling, κ, between elements though this obviously has its limits as the maximum coupling is achieved when elements are almost in contact.

Given the examples of axial and planar one-dimensional MI waveguides in Figures 2.3a and 2.3b, it can be seen that the axial structure can attain a higher coupling between elements than the planar one, and that the planar structure is more capable of covering a further distance than an axial one. Initially, it would seem that there would have to be a trade-off between the coupling between elements, and therefore bandwidth, and the distance covered by the structure. However Syms et al. [50] managed to create a structure that achieves high inter-element coupling, whilst maintaining a planar geometry. An example of such a structure is given in Figure 2.12 and it can be seen that each element is comprised of two halves on opposite sides of a thin substrate. Adjacent elements couple to each other axially, with comparitively little separation, giving rise to a high inter-element coupling, and the two halves of each element are connected via two parallel-plate capacitors formed by capacitve pads, which also determine's the element's capacitance.

Finally, the system capacity is also affected by the coupling between terminals and the MI waveguide. We found previously that an optimum coupling to the waveguide exists and is given by [21]

$$|\kappa_x| \approx 2\eta_x|\kappa|, \tag{2.33}$$

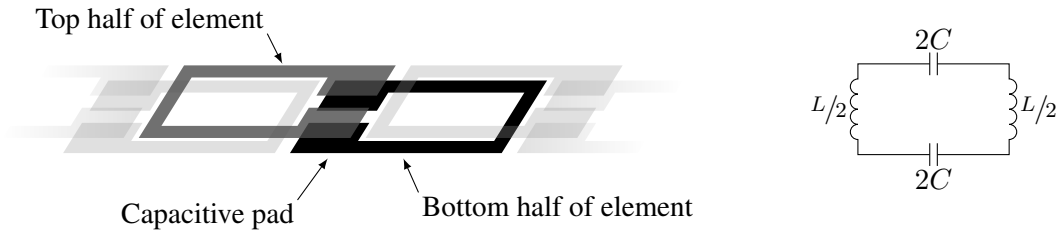


Figure 2.12 – An example that illustrates the structure proposed by Syms et al [50] (a), and a single element's equivalent circuit (b).

where κ_x is the coupling coefficient for the terminal-waveguide interaction, η_x is 1 or 2 depending on whether the waveguide is one- or two- dimensional, and κ is the nearest neighbour waveguide coupling coefficient. This arose from the observation that the frequencies of the edges of the MI passband, given by (2.16), could be equated to the split frequencies of two coupled resonators (the terminal, and the element directly underneath), given by (2.9). This effectively means that there is a specific height that a terminal should be above the waveguide for highest transmission, and thus capacity. This also means for a 2-D array with the same in-plane coupling as a 1-D strip, the terminals have to be closer to the waveguide for optimum coupling. Also it is worth noting, when taking into consideration higher order interactions, that for 2-D arrays there exist different values of optimum terminal-waveguide coupling for different nearest neighbour couplings.



Figure 2.13 – Example of a non-resonant probe (a), made from RG402/U semi-rigid coaxial cable with a 10 mm inner diameter coil made from its 1 mm thick inner wire. Resonant probe (b), made by soldering RG402/U cable across the gap of a capacitvely-loaded split ring.

The majority of previous work utilizes a non-resonant loop probe to excite the MI waveguide as shown in Figure 2.13a. The reason for their use was that by weakly coupling to the structure, it wouldn't be loaded by the probe and the load it was connected to, namely the 50 Ω of the VNA, so that the structure could be accurately characterized. However, as the desire is to effectively exchange signals between the waveguide and terminal, a better coupling is required.

It was thought that a resonant probe would make a better terminal as it would likely increase transmission within the comparatively narrow MI pass band.

One of the original attemps at resonant terminals, shown in Figure 2.13b, was made by simply by attaching a length of 50 Ω cable across the gap of a capacitively loaded split-ring [51]. Syms et al. [52] have a slightly different approach, whereby the load of the VNA is attached in series to the resonator's elements. Though by the nature of Syms's thin-film cable, the probe was composed of half of a resonator, halving the inductance, and thereby requiring a capacitor of double the capacitance to be soldered in series to the SMA termination. This particular version of MI transducer has an improved version comprised of three parallel LC circuits in order to approximate the perfect terminating impedance given by equation (2.18) [53].

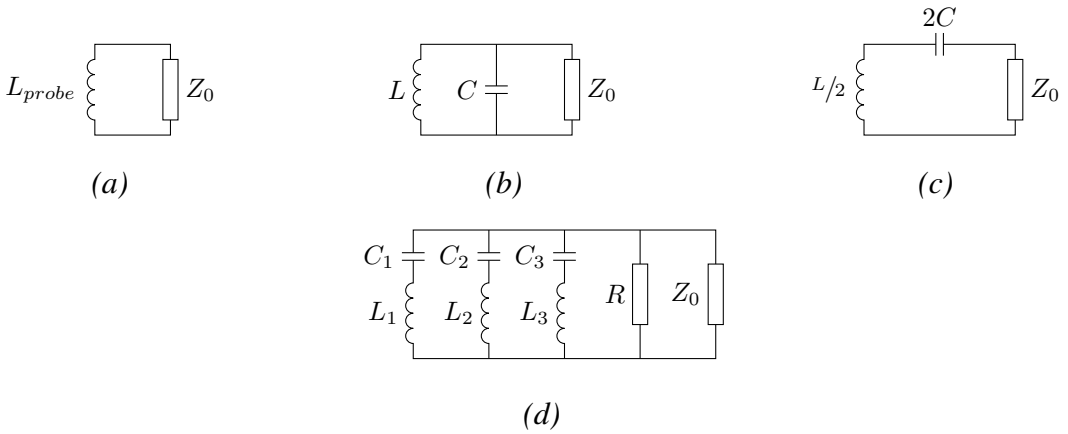


Figure 2.14 – Circuit diagram for a loop probe as shown in Figure 2.13a where L_{probe} denotes the inductance of the loop (a), a resonant probe with load connected in parallel as used by Stevens et al. with L and C being the inductance and capacitance of the resonator (b), a resonant probe with load connected in series with a half element used by Syms et al. (c), a triple resonant probe as suggested by Sydrouk et al. (d) one of the branches is formed of a half element, and the others by discrete components. Z_0 denotes the load presented by the VNA.

Figure 2.14, shows the equivalent circuit diagrams for the loop probe (Figure 2.14a), the parallel resonant probe (Figure 2.14b), the series resonant probe as used by Syms et al. (Figure 2.14c), and the triple-resonant probe as developed by Sydoruk (Figure 2.14d). The various parameters of the triple-resonant probe are calculated using various formulas derived in [53]. However it must be noted that much like the series-resonant probe used by Syms et al. [52], the triple-resonant probe is designed to be on the same substrate as the rest of the MI waveguide,

thus the terminal-waveguide coupling is the same as the inter-element coupling. Whilst this improved transducer design provides lower reflection across the whole band, the transmission shows no improvement over previous attempts[1].

[1] Sydoruk states that this "triple-resonant" transducer shows no improvement for the loss that is achievable in pratical MI waveguides.

CHAPTER 3

MODEL DESIGN

In the previous Chapter, a brief history of metamaterials was given along with an introduction to the metamaterial element. The interaction between two elements was covered, and the dispersion relationship of one- and two-dimensional MI waveguides was given which also lead to an expression for the achievable bandwidth. In this chapter, the approach for simulating finite one- and two-dimensional waveguides, along with terminal modelling and interaction, is covered.

3.1 THE IMPEDANCE MATRIX

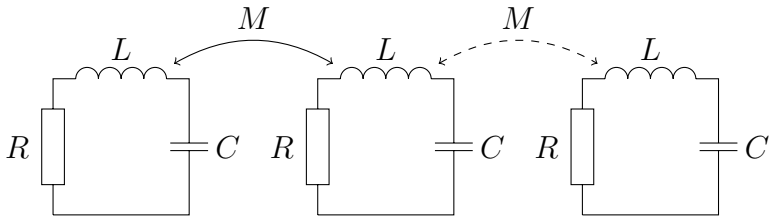


Figure 3.1 – Equivalent electrical circuit of a finite SRR strip

When considering a finite strip of length N as depicted in Figure 3.1, the impedance matrix for two-elements, presented by (2.7), can simply be expanded to accommodate more

terms. Therefore a strip of length N has its impedance matrix described by an N by N square matrix as shown in (3.1)

$$\boldsymbol{Z} = \begin{pmatrix} Z & j\omega M & 0 & \cdots & \cdots & \cdots & 0 \\ j\omega M & Z & j\omega M & 0 & \cdots & \cdots & \vdots \\ 0 & j\omega M & Z & j\omega M & 0 & \cdots & \vdots \\ \vdots & \ddots & \ddots & \ddots & \ddots & \ddots & \vdots \\ \vdots & \cdots & 0 & j\omega M & Z & j\omega M & 0 \\ \vdots & \cdots & \cdots & 0 & j\omega M & Z & j\omega M \\ 0 & \cdots & \cdots & \cdots & 0 & j\omega M & Z \end{pmatrix}. \tag{3.1}$$

It can be seen that (3.1) is a diagonal matrix with the element impedances, Z, on the leading diagonal and the coupling terms, $j\omega M$, on the off-diagonals. Additional nearest neighbour couplings will simply add more off-diagonals; a second neighbour coupling will fill the second off-diagonal with coupling terms, the third neighbour coupling, the third off-diagonal, and so on.

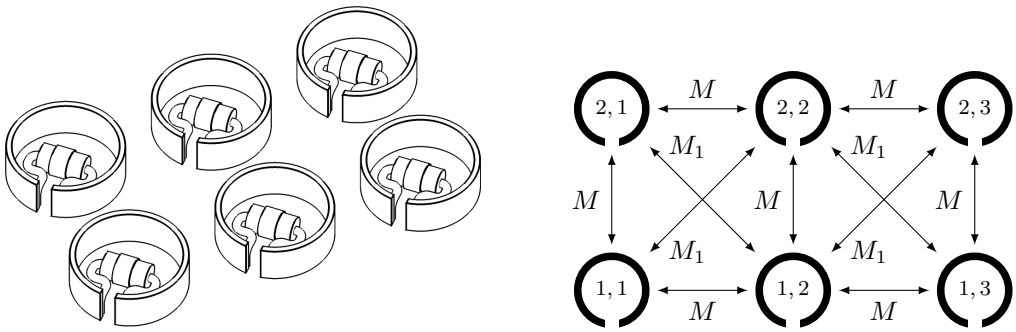


Figure 3.2 – A 3 by 2 metamaterial array (a), and its coupling nomenclature (b).

The 2-D case shown in Figure 3.2a is a little different as there are new coupling terms as shown in Figure 3.2b and its element voltage-current relationships are given by (3.2) and given in matrix form by (3.3)

$$\begin{cases} V_{1,1} = ZI_{1,1} + j\omega M(I_{1,2} + I_{2,1}) + j\omega M_1 I_{2,2} \\ V_{1,2} = ZI_{1,2} + j\omega M(I_{1,1} + I_{1,3} + I_{2,2}) + j\omega M_1(I_{2,1} + I_{2,3}) \\ V_{1,3} = ZI_{1,3} + j\omega M(I_{1,2} + I_{2,3}) + j\omega M_1 I_{2,2} \\ V_{2,1} = ZI_{2,1} + j\omega M(I_{2,2} + I_{1,1}) + j\omega M_1 I_{1,2} \\ V_{2,2} = ZI_{2,2} + j\omega M(I_{2,1} + I_{2,3} + I_{1,2}) + j\omega M_1(I_{1,1} + I_{1,3}) \\ V_{2,3} = ZI_{2,3} + j\omega M(I_{2,2} + I_{1,3}) + j\omega M_1 I_{1,2} \end{cases}. \tag{3.2}$$

$$\begin{pmatrix} V_{1,1} \\ V_{1,2} \\ V_{1,3} \\ V_{2,1} \\ V_{2,2} \\ V_{2,3} \end{pmatrix} = \begin{pmatrix} \boxed{\begin{matrix} Z & j\omega M & 0 \\ j\omega M & Z & j\omega M \\ 0 & j\omega M & Z \end{matrix}} & \boxed{\begin{matrix} j\omega M & j\omega M_1 & 0 \\ j\omega M_1 & j\omega M & j\omega M_1 \\ 0 & j\omega M_1 & j\omega M \end{matrix}} \\ \boxed{\begin{matrix} j\omega M & j\omega M_1 & 0 \\ j\omega M_1 & j\omega M & j\omega M_1 \\ 0 & j\omega M_1 & j\omega M \end{matrix}} & \boxed{\begin{matrix} Z & j\omega M & 0 \\ j\omega M & Z & j\omega M \\ 0 & j\omega M & Z \end{matrix}} \end{pmatrix} \begin{pmatrix} I_{1,1} \\ I_{1,2} \\ I_{1,3} \\ I_{2,1} \\ I_{2,2} \\ I_{2,3} \end{pmatrix}. \tag{3.3}$$

The outlined terms highlight the basic building blocks for the generic 2D impedance matrix and are given by (3.4)

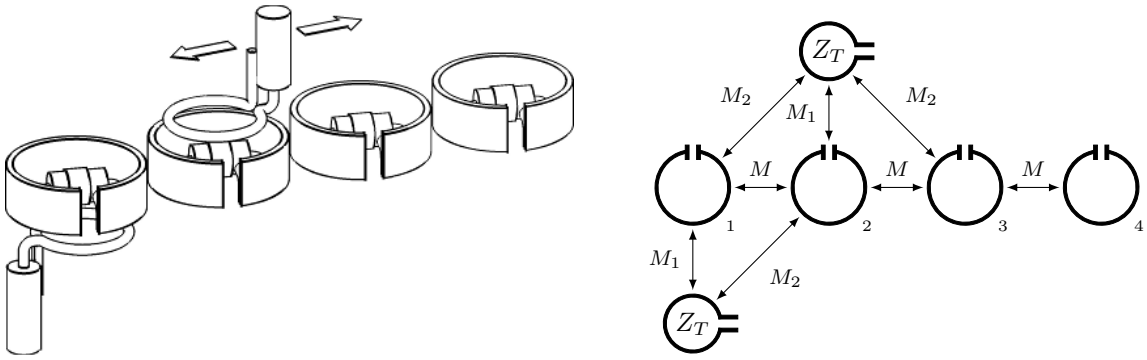
$$\boldsymbol{A} = \begin{pmatrix} Z & j\omega M & 0 & \cdots & \cdots & \cdots & 0 \\ j\omega M & Z & j\omega M & 0 & \cdots & \cdots & 0 \\ 0 & j\omega M & Z & j\omega M & 0 & \cdots & 0 \\ \vdots & \ddots & \ddots & \ddots & \ddots & \ddots & \vdots \\ \vdots & \cdots & \cdots & 0 & j\omega M & Z & j\omega M \\ 0 & \cdots & \cdots & \cdots & 0 & j\omega M & Z \end{pmatrix}$$

$$\boldsymbol{B} = \begin{pmatrix} j\omega M & j\omega M_1 & 0 & \cdots & \cdots & \cdots & 0 \\ j\omega M_1 & j\omega M & j\omega M_1 & 0 & \cdots & \cdots & 0 \\ 0 & j\omega M_1 & j\omega M & j\omega M_1 & 0 & \cdots & 0 \\ \vdots & \ddots & \ddots & \ddots & \ddots & \ddots & \vdots \\ \vdots & \cdots & \cdots & 0 & j\omega M_1 & j\omega M & j\omega M_1 \\ 0 & \cdots & \cdots & \cdots & 0 & j\omega M_1 & j\omega M \end{pmatrix}. \tag{3.4}$$

It is clear that both $\boldsymbol{A}$ and $\boldsymbol{B}$ are of the same form as (3.1) but $\boldsymbol{B}$ has different terms on its leading and off diagonals. The sizes of $\boldsymbol{A}$ and $\boldsymbol{B}$ are determined by the number of columns n. $\boldsymbol{A}$ describes the coupling inside a row and $\boldsymbol{B}$ describes the inter-row coupling. Following (3.3) and using (3.4), the general form for the 2D impedance matrix is expressed in (3.5) and the number of times $\boldsymbol{A}$ is repeated on the leading diagonal is determined by the number of rows m.

$$\boldsymbol{Z} = \begin{pmatrix} \boldsymbol{A} & \boldsymbol{B} & \boldsymbol{0} & \cdots & \cdots & \boldsymbol{0} \\ \boldsymbol{B} & \boldsymbol{A} & \boldsymbol{B} & \boldsymbol{0} & \cdots & \boldsymbol{0} \\ \boldsymbol{0} & \boldsymbol{B} & \ddots & \ddots & \ddots & \vdots \\ \vdots & \ddots & \ddots & \ddots & \boldsymbol{B} & \boldsymbol{0} \\ \vdots & \ddots & \ddots & \boldsymbol{B} & \boldsymbol{A} & \boldsymbol{B} \\ \boldsymbol{0} & \cdots & \cdots & \boldsymbol{0} & \boldsymbol{B} & \boldsymbol{A} \end{pmatrix}. \tag{3.5}$$

3.2 TERMINALS



(a) *(b)*

Figure 3.3 – Two terminals with one scanning above a one-dimensional MI waveguide composed of SRRs (a), and its schematic representation (b), where Z_T is the terminal impedance, M is the coupling between elements and $M_{1,2}$ are the coupling terms between the terminals and the MI waveguide.

The MI waveguide itself only serves as a communications medium, to form a communications system, input and output terminals, referred to as 'terminals', need to be characterized and modelled along with the MI waveguide; a case where two terminals are coupled to a one-dimensional MI waveguide composed of SRRs is displayed in Figure 3.3a. If one assumes the coupling scheme described in 3.3b, then its impedance matrix is given by (3.6)

$$\boldsymbol{Z} = \begin{pmatrix} Z & j\omega M & 0 & 0 & j\omega M_1 & j\omega M_2 \\ j\omega M & Z & j\omega M & 0 & j\omega M_2 & j\omega M_1 \\ 0 & j\omega M & Z & j\omega M & 0 & j\omega M_2 \\ 0 & 0 & j\omega M & Z & 0 & 0 \\ j\omega M_1 & j\omega M_2 & 0 & 0 & Z_T & 0 \\ j\omega M_2 & j\omega M_1 & j\omega M_2 & 0 & 0 & Z_T \end{pmatrix}. \tag{3.6}$$

The last two rows and columns are due to the terminals and their coupling to the MI waveguide. One can see that terminals coupled to the MI waveguide just extend the impedance matrix, Z, whilst filling the appropriate rows and columns with coupling terms. This gives the general form of the impedance with terminals as (3.7)

$$\boldsymbol{Z} = \begin{pmatrix} \boldsymbol{Z_{mat}} & \boldsymbol{M_{ext1}} & \boldsymbol{M_{ext2}} & \cdots & \boldsymbol{M_{extn}} \\ \boldsymbol{M_{ext1}}^T & Z_{ext1} & M_{1,2} & \cdots & M_{1,n} \\ \boldsymbol{M_{ext2}}^T & M_{1,2}^T & Z_{ext2} & \cdots & M_{2,n} \\ \vdots & \ddots & \ddots & \ddots & \vdots \\ \boldsymbol{M_{extn}}^T & M_{1,n} & M_{2,n} & \cdots & Z_{extn} \end{pmatrix}, \tag{3.7}$$

where $\boldsymbol{Z_{mat}}$ is the impedance matrix of a MI waveguide, $Z_{ext1,ext2,...,extn}$ are the impedances for the first, second to n^{th} terminals respectively. $\boldsymbol{M_{ext1,ext2,...,extn}}$ are the vectors that describe how the terminals couple to the MI waveguide, and the elements $M_{1,n}$ to $M_{n-1,n}$ are the coupling terms for the interaction between terminals as applicable.

3.2.1 TERMINAL COUPLING SCHEMES

It has been shown that the terminal's coupling to the waveguide is represented by terms in the corresponding column or row of the impedance matrix, but the number of terms has yet to be specified. Clearly, the amount of terms to include depends on the location of the terminal relative to elements, nearby or otherwise. A basic example based on nearest neighbour coupling is given in Figure 3.4.

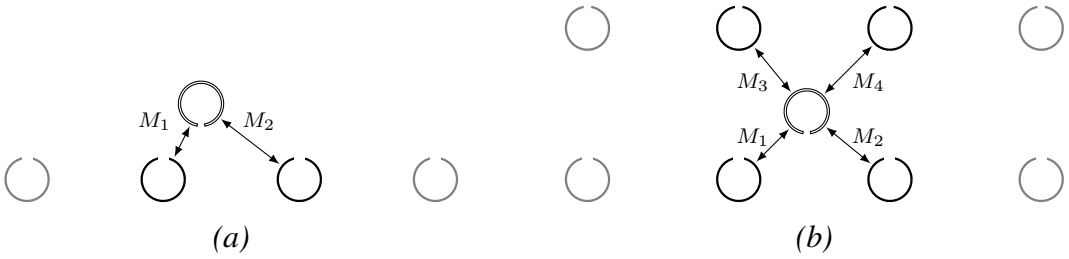


Figure 3.4 – An example of nearest neighbour coupling for a 1-D line and two neighbours (a), and 2-D array and four neighbours (b), where the outlined ring represents the terminal, and the grey rings represent elements for which the coupling is not considered.

This method would initially appear to be adequate, however, consider the case shown in Figure 3.5.

Suddenly, when moving over an element, a third coupling term is introduced. The effect of this sudden 'extra' coupling will depend on how strong the new coupling is relative to the

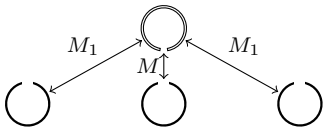


Figure 3.5 – A situation when using a 1-D line whereby the terminal, represented by an outlined ring, couples to an element below it with coupling M, and to two adjacent elements with an equal coupling of M_1.

existing coupling and this will depend on the distance of the terminal from the waveguide and the distance between elements. Should the 'extra' term be strong relative to the existing coupling, this will create a noticeable difference between the transfer functions in the cases shown in Figure 3.5. This type of coupling regime, that uses a fixed number of nearest neighbours, has a more pronounced effect in two-dimensional waveguides.

In order to minimise the effect of considering differing amounts of coupling terms when varying terminal location, a different coupling scheme must be used, three of which shall be outlined below.

One could simply consider coupling the terminal to all elements in the array, though computational time would rise significantly compared to the previous method with more elements in the array. This is partly due to having to calculate the coupling between the terminal and all elements for each unique terminal location, and also filling the impedance matrix with more off-diagonal terms. Whilst this method does eliminate the issue caused by using nearest neighbour coupling, it can potentially be very inefficient as the coupling between the terminal and elements decreases dramatically with increased terminal-waveguide separation.

The next two methods are probably equal in complexity: couple to a set amount of elements or couple to all elements within a radius of the terminal. The first method would entirely eliminate the problem associated with introducing extra coupling terms as the amount of coupling terms does not change whatever the terminal location. However, consider the case shown in Figure 3.6 where the terminal will always couple to a 3-by-3 square of elements.

Clearly, when the terminal is at the midpoint between the second and third columns, the choice of what 9 elements to couple to becomes ambiguous as the terminal is equidistant from

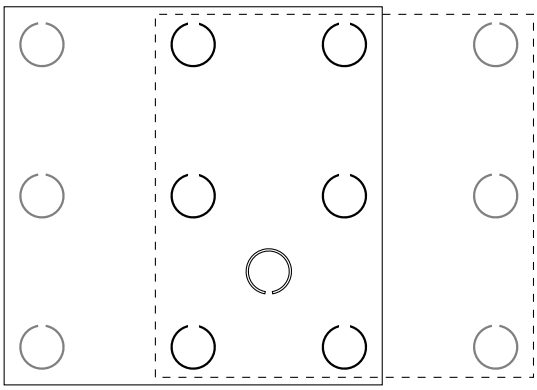


Figure 3.6 – A single terminal is situated on the midpoint between two columns, this presents a case whereby if the terminal were to couple to a 3-by-3 square, there are two possible choices of which 9 elements are to be coupled to: the grey set on the left, outlined by a solid box), or the right, outlined by a dashed box.

the elements in the first and fourth columns. This problem is mitigated by using the latter of the last two methods in which the terminal-element couplings are considered within a radius of the terminal. Though this also has the problem of the original nearest neighbour coupling scheme where the number of elements coupled to varies with terminal location.

In both the aforementioned coupling schemes, the height of the terminal above the elements has to be considered; the relative strength of terminal-element coupling varies with the physical distance between the two, thus when the terminal is further away from the waveguide, the greater the difference between the coupling of the terminal to the nearest neighbour and the coupling of the terminal to the second nearest neighbour and so forth. With this in mind, the effect of the varying number of couplings considered in the second scheme can be mitigated if the radius is such that the contribution of the coupling is negligible with increased radius. A similar effect would be achieved if one were to simply couple to more elements in the first of the last two schemes, however this scheme would still suffer from ambiguous coupling cases.

3.2.2 TERMINAL MODELLING

As shown in Figure 3.3, the system being simulated consists of at least two terminals and a MI waveguide. The matrix given by (3.6) in Section 3.2 shows the basics of integrating the probes into the impedance matrix that is required for the simulation of the MI data system. Figure

2.14 gives examples of terminals, and by inspection it is trivial to deduce what impedance term should be added to the impedance matrix. However, the power ratio is needed to infer system capacity. This is done by calculating the current that flows through the VNA's load Z_0. This current is obtained by inverting the impedance matrix and multiplying it by the vector representing the voltages within each element.

Consider the case where there is a simple series-type terminal such as the one given in Figure 3.7.

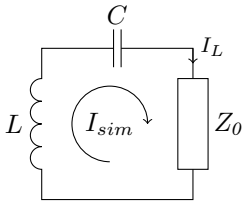


Figure 3.7 – An example of a series-type terminal with an inductance L, a capacitance C, and where Z_0 represents the VNA load. I_{sim} represents the current in the terminal that is given by the simulation, and I_L is the current that flows through the load.

It would be trivial to calculate the power extracted as the terminal impedance is simply the sum of the VNA load and the discrete elements, hence I_L is equal to I_{sim}. Thus the power input and extracted by a series-type terminal is given by (3.8) and (3.9) respectively.

$$P_{in} = V_s \times \mathrm{Re}(I_{sim}), \tag{3.8}$$

$$P_{out} = I_{sim}^2 \times Z_0. \tag{3.9}$$

Where V_s is the source of the VNA and would be represented as a voltage source in series with VNA load.

However, there are also parallel-type terminals such as those given in Figure 3.8, and upon its inspection, the calculation of the impedance term to be inserted into the impedance matrix is trivial. However, the current that corresponds to this element, is not the current that flows through the VNA load, I_{out}, or the current given by the VNA, I_{in}, but the impedance of the VNA load in parallel with other lumped elements, I_{sim}. There are two ways to deal with

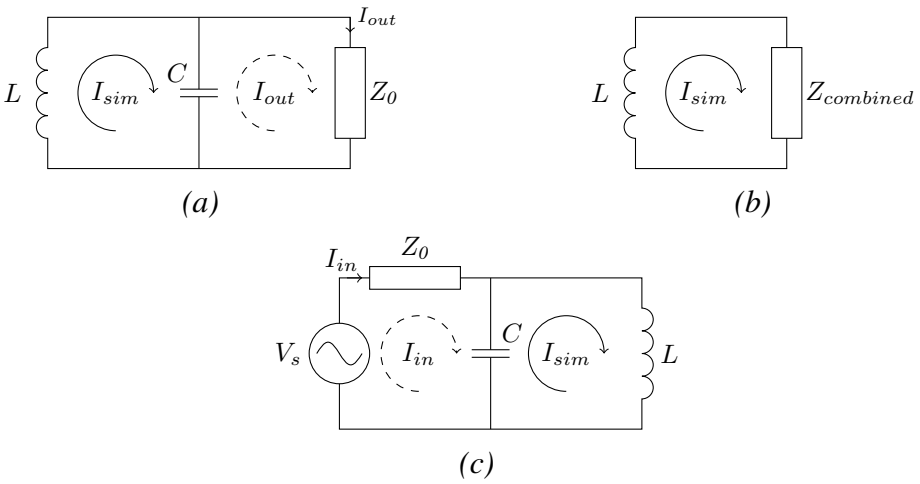


Figure 3.8 – An example of a parallel-type terminal (a), with inductance L, a capacitance C, and where Z_0 represents the load presented by the VNA. I_{sim} is the current given through simulation, and the dashed loop I_{out} is the current that flows through the load. Where the capacitance C and Z_0 are combined in parallel to make $Z_{combined}$, the parallel circuit is collapsed into series circuit (b). (c) shows the equivalent circuit of the VNA's input side where I_{sim} is the current given through simulation, and I_{in} is the current that is generated by the VNA.

this, the first would be to perform some mesh analysis on the circuits shown in Figures 3.8a and 3.8c. This will yield the two preliminary equations shown in (3.10) and (3.11) for the input and output terminals respectively

$$V_s = I_{in}\left(Z_0 + \frac{1}{j\omega C}\right) - \frac{I_{sim}}{j\omega C}, \tag{3.10}$$

$$0 = I_{out}\left(Z_0 + \frac{1}{j\omega C}\right) - \frac{I_{sim}}{j\omega C}. \tag{3.11}$$

(3.10) and (3.11) will rearrange to (3.12) and (3.13) respectively to yield expressions for the input, I_{in}, and output, I_{out} current respectively

$$I_{in} = \frac{I_{sim} + j\omega C V_s}{1 + j\omega C Z_0}, \tag{3.12}$$

$$I_{out} = \frac{I_{sim}}{1 + j\omega C Z_0}. \tag{3.13}$$

Another is by keeping the current loops of the branches of the parallel circuit separate, and adding an extra element to the diagonal of the impedance matrix, then add the appropriate coupling terms which relate the two loops together; (3.14) shows a typical impedance matrix

with the terminal shown in Figure 3.8b included into the matrix, and (3.15) shows its expansion into separate branches.

$$\begin{pmatrix} Z & j\omega M & 0 & \dots & 0 \\ j\omega M & Z & j\omega M & 0 & \vdots \\ 0 & \ddots & \ddots & \ddots & \vdots \\ \vdots & 0 & j\omega M & Z & j\omega M_t \\ \vdots & \dots & \dots & j\omega M_t & \boxed{j\omega L + Z_{combined}} \end{pmatrix}, \tag{3.14}$$

$$\begin{pmatrix} Z & j\omega M & 0 & \dots & \dots & 0 \\ j\omega M & Z & j\omega M & 0 & \ddots & \vdots \\ 0 & \ddots & \ddots & \ddots & \ddots & \vdots \\ \vdots & 0 & j\omega M & Z & j\omega M_t & 0 \\ \vdots & \ddots & \ddots & j\omega M_t & \boxed{j\omega L + \frac{1}{j\omega C} \quad -\frac{1}{j\omega C}} & \\ 0 & \dots & \dots & 0 & \boxed{-\frac{1}{j\omega C} \quad \frac{1}{j\omega C} + Z_0} & \end{pmatrix}. \tag{3.15}$$

Using the method presented by (3.15), one can see that current in the load, I_L, corresponds to the last element in the matrix.

3.2.3 CABLE MODELLING

Lastly, the previous transducers have not taken the length of the coaxial cable into account. It should be noted that in some cases, this is unimportant, as the wavelength is large in comparison to the length of the coaxial used thus there is a negligible phase change along the length of the cable. First consider the cable as a transmission line as the circuit in Figure 3.9 illustrates.

Of course, this is not in the desired form, so it is necessary to first obtain the Thévenin equivalent to the circuit. For a series-type probe, as shown in Figure 3.9a, the Thévenin equivalent must be obtained after the transmission line section as shown in Figure 3.10.

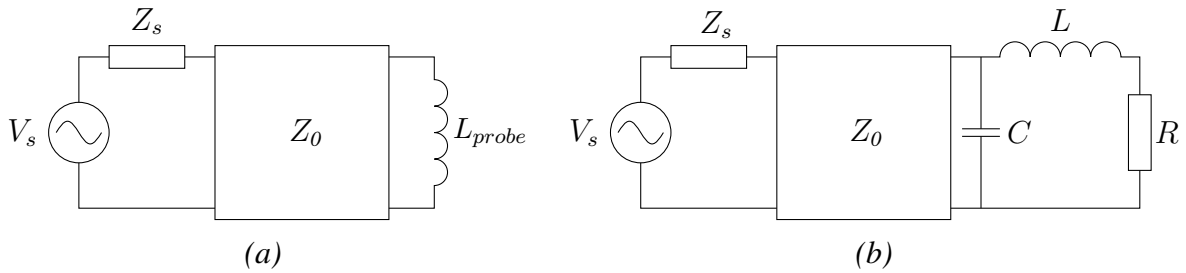


Figure 3.9 – An example of a series-type (a), and parallel-type (b), terminal with cable model where Z_s is the load impedance of the VNA, Z_0 is the characteristic impedance of the cable, L_{probe} is the probe inductance, L, C, and R are the inductance, capacitance, and resistance of the resonant terminal.

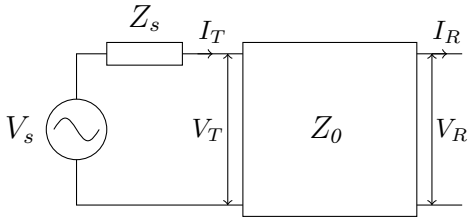


Figure 3.10 – Series-type probe with cut after cable section with the transmit voltage and current, V_T, I_T, and receive voltage and current, V_R, I_R, displayed.

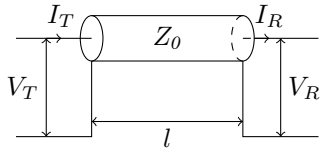


Figure 3.11 – Illustration of a transmission line of length l and characteristic impedance Z_0 with the transmit voltage and current, ,V_T, I_T, and the receive voltage and current, V_R, I_R, indicated.

Using the matrix for a transmission line as given by Figure 3.11 and (3.16).

$$\begin{pmatrix} V_T \\ I_T \end{pmatrix} = \begin{pmatrix} A & Z_0 B \\ \frac{B}{Z_0} & A \end{pmatrix} \begin{pmatrix} V_R \\ I_R \end{pmatrix}, \qquad where \begin{cases} A = \cosh \gamma l \\ B = \sinh \gamma l \end{cases}. \tag{3.16}$$

It can be seen that the voltage dropped over Z_s in Figure 3.10 is $Z_s I_T$, so (3.16) can be modified to

$$\begin{pmatrix} V_s - Z_s I_T \\ I_T \end{pmatrix} = \begin{pmatrix} A & Z_0 B \\ \frac{B}{Z_0} & A \end{pmatrix} \begin{pmatrix} V_R \\ I_R \end{pmatrix}. \tag{3.17}$$

The Thévenin equivalent can then be calculated by determining the open circuit voltage, V_{oc}, and the short circuit current, I_{sc}. This is done by setting I_R and V_R in (3.17) to zero for V_{oc} and I_{sc} respectively, and these are given by (3.18) and (3.19),

$$V_{oc} = \frac{V_s}{A+B}, \tag{3.18}$$

$$I_{sc} = \frac{V_s}{Z_0(A+B)}, \tag{3.19}$$

where, of course, Z_s is equal to Z_0 as the cable and source impedance are matched. The effective impedance is of course V_{oc}/I_{sc} which is the cable impedance, Z_0. Thus the Thévenin equivalent of a the series-type probe given by Figure 3.9a is given by Figure 3.12.

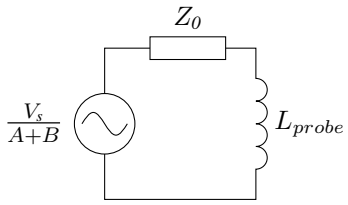


Figure 3.12 – The Thévenin equivalent to the series-type probe, with cable section, presented in Figure 3.9a

For the parallel-type probe shown in Figure 3.9b, one can simply take the Thévenin equivalent circuit from Figure 3.12 but add a shunt capacitor, and then calculate the Thévenin equivalent of that circuit. In this case, V_{oc} and I_{sc} are given by (3.20) and (3.21) respectively

$$V_{oc} = \frac{V_s}{(A+B)(1+j\omega C Z_0)}, \tag{3.20}$$

$$I_{sc} = \frac{V_s}{Z_0(A+B)}. \tag{3.21}$$

Thus the Thévenin resistance is given by dividing (3.20) by (3.21) and the equivalent circuit for the parallel-type probe shown in Figure 3.9b is given by Figure 3.13.

When the cable is included into the model, the method for extracting both the input and output current from the simulation is not so trivial. Referring to (3.17), it can been seen that

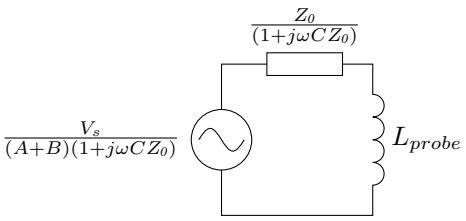


Figure 3.13 – The Thévenin equivalent of the parallel-type cable modelled probe, presented in Figure 3.9b

what needs to be calculated is I_T as this is the current in the source, however, in its current form this cannot be done without first determining V_R. First, consider the series-type probe shown in Figure 3.9a, using (3.17) it may be shown that

$$I_T = V_R \frac{B}{Z_0} + I_R A. \tag{3.22}$$

However to determine V_R, more information is needed. The form currently shown in Figure 3.9a is of an unloaded terminal, that is to say that this does not include coupling to the MI waveguide. A terminal coupled to a MI waveguide of length n is shown in Figure 3.14.

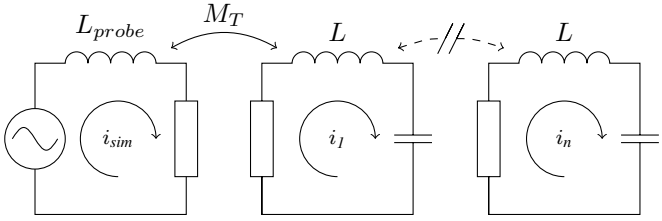


Figure 3.14 – The Thévenin equivalent of the terminal with cable model, connected to the first element of an MI waveguide via the mutual inductance M_T.

In Figure 3.14, it can be seen that I_{sim} is actually I_R, and remembering how the Thévenin equivalent was derived using Figure 3.10, V_R is given by

$$V_R = j\omega L_{probe} I_R + j\omega M_T I_1, \tag{3.23}$$

by substituting (3.23) into (3.22), the full formula for I_T can be obtained

$$I_T = \left(A + \frac{B}{Z_0} L_{probe} \right) I_R + j\omega \frac{B}{Z_0} I_1, \tag{3.24}$$

where $I_R = I_{sim}$, and I_1 is the current in the first element. Thus the power in is given by

$$P_{in} = V_s \times \mathrm{Re}(I_T). \tag{3.25}$$

The power out, P_{out}, is much easier to deduce, consider Figure 3.15.

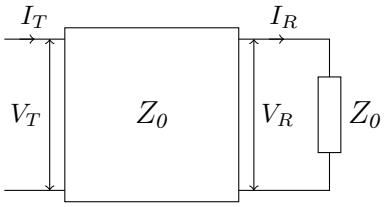


Figure 3.15 – The section of the VNA that is connected to the terminal (not shown), including a cable section and its load Z_0.

It can be seen that

$$\begin{pmatrix} V_T \\ I_T \end{pmatrix} = \begin{pmatrix} A & Z_0 B \\ \frac{B}{Z_0} & A \end{pmatrix} \begin{pmatrix} I_R Z_0 \\ I_R \end{pmatrix}. \tag{3.26}$$

As it is V_T that is the unknown quantity, and I_T is given by the simulation, one can use the formula for I_T that can be obtained from the bottom row of (3.26), and rearrange to get I_R

$$I_R = \frac{I_T}{A + B}. \tag{3.27}$$

Of course, it is now trivial to calculate what P_{out} is. However the method used to determine the power input from equations (3.23) and (3.24) only applies to the case shown in Figure 3.14 as the terminal is only coupled to one element in the waveguide. One can imagine that, dependent on the elements coupled to, the term V_R given in (3.23) would simply include the relevant terms. For example, if the terminal were to be coupled to the first and second elements, V_R would be modified to

$$V_R = j\omega L_{probe} I_R + j\omega M_{T1} I_1 + j\omega M_{T2} I_2, \tag{3.28}$$

where M_{T1} and M_{T2} are the mutual inductances between the terminal and the first and second elements respectively. One can imagine that the more elements that the terminal is coupled to, the more terms that would be included into (3.28).

There is a method that only requires knowledge of the current in the terminal given by the simulation. First of all, the transmission matrix given in (3.17) has to be inverted

$$\begin{pmatrix} V_R \\ I_R \end{pmatrix} = \begin{pmatrix} A & -Z_0 B \\ -\frac{B}{Z_0} & A \end{pmatrix} \begin{pmatrix} V_s - I_T Z_s \\ I_T \end{pmatrix}. \tag{3.29}$$

This gives an expression for the current in the probe given by (3.30)

$$I_R = -\frac{B}{Z_0}(V_s - I_T Z_s) + I_T A. \tag{3.30}$$

Which can be rearranged in terms of I_T, giving an equation where the current given by the VNA can be determined only by the current flowing in the probe section of the terminal, I_R, which is determined through simulation

$$I_T = \frac{I_R + V_s \frac{B}{Z_0}}{A + B}. \tag{3.31}$$

Deriving the analogous currents for the parallel-type probe involves only a little more complication. Following the example terminal shown in Figure 3.9b, the shunt capacitor has to be added to the transmission matrix and this is done with the knowledge of its transmission matrix, and this is given by (3.32)

$$\begin{pmatrix} V_R \\ I_R \end{pmatrix} = \begin{pmatrix} 1 & 0 \\ -j\omega C & 1 \end{pmatrix} \begin{pmatrix} V_T \\ I_T \end{pmatrix}. \tag{3.32}$$

Given where the Thévnin equivalent is taken, the matrix shown in (3.32) is first inverted,

then put after the matrix for a transmission line, giving (3.33)

$$\begin{pmatrix} V_T \\ I_T \end{pmatrix} = \begin{pmatrix} A & Z_0 B \\ \frac{B}{Z_0} & A \end{pmatrix} \begin{pmatrix} 1 & 0 \\ j\omega C & 1 \end{pmatrix} \begin{pmatrix} V_R \\ I_R \end{pmatrix}. \tag{3.33}$$

Again, in order to find I_T, one must first know V_R, but in order to determine V_R, the knowledge of the terminal-waveguide couplings must be known. So it is simpler, instead, to invert the transmission matrix presented by (3.33) as I_R is known, and V_T can be changed to $V_s - I_T Z_s$

$$\begin{pmatrix} V_R \\ I_R \end{pmatrix} = \begin{pmatrix} A & -Z_0 B \\ -\left(\frac{B}{Z_0} + j\omega C A\right) & A + j\omega C Z_0 B \end{pmatrix} \begin{pmatrix} V_s - Z_s I_T \\ I_T \end{pmatrix}. \tag{3.34}$$

This gives an expression for I_R

$$I_R = -\left(\left(\frac{B}{Z_0} + j\omega C A\right)(V_s - Z_s I_T)\right) + (A + j\omega C Z_0 B I_T), \tag{3.35}$$

and from (3.35), an expression for I_T can be derived

$$I_{in} = I_T = \frac{I_R + V_s\left(\frac{B}{Z_0} + j\omega C A\right)}{(A+B)(1 + j\omega C Z_0)}. \tag{3.36}$$

Deriving the power absorbed by the VNA is relatively simple, a similar method is adopted whereby the transmission matrix for a capacitor is placed before the transmission line matrix giving (3.37) and recognising that for the load, $V_R = I_R Z_0$

$$\begin{pmatrix} V_T \\ I_T \end{pmatrix} = \begin{pmatrix} 1 & 0 \\ j\omega C & 1 \end{pmatrix} \begin{pmatrix} A & Z_0 B \\ \frac{B}{Z_0} & A \end{pmatrix} \begin{pmatrix} I_R Z_0 \\ I_R \end{pmatrix}, \tag{3.37}$$

which gives

$$\begin{pmatrix} V_T \\ I_T \end{pmatrix} = \begin{pmatrix} A & Z_0 B \\ j\omega C A + \frac{B}{Z_0} & j\omega C Z_0 B + A \end{pmatrix} \begin{pmatrix} I_R Z_0 \\ I_R \end{pmatrix}. \tag{3.38}$$

From (3.38) one can obtain an expression for I_T, (3.39), and thus derive I_R, (3.40)

$$I_T = \left(j\omega CA + \frac{B}{Z_0} \right) I_R Z_0 + \left(j\omega C Z_0 B + A \right) I_R, \tag{3.39}$$

$$I_{out} = I_R = \frac{I_T}{(A+B)(1+j\omega C Z_0)}. \tag{3.40}$$

One can see how the expressions for the current provided and absorbed by the VNA, (3.36) and (3.39) respectively, for the parallel-type probe, as shown in Figure 3.9b, differ from the analogous expressions for the series-type probe presented in Figure 3.9a.

A crucial test is whether the equations for input and output current derived for the cable model, (3.36) and (3.40), match the expressions for I_{in} and I_{out} derived without the cable model, (3.12) and (3.13), when the cable length, l, is zero. From (3.16), it can be seen that as when $l = 0$, $A = \cosh 0 = 1$ and $B = \sinh 0 = 0$ and thus the expressions for I_{in} and I_{out} do indeed equate to the derived without considering the cable when $l = 0$.

3.2.4 TERMINAL PERFORMANCE ASSESSMENT METHOD

There a few ways in which terminal performance could be assessed. One might initially expect that measuring the reflection, s_{11}, of the terminal would suffice, but this only affords information of the terminal in isolation. What should be considered is the s_{11} of the terminal coupled to a waveguide. Figure (3.16) shows the circuit equivalent of a terminal coupled to a waveguide.

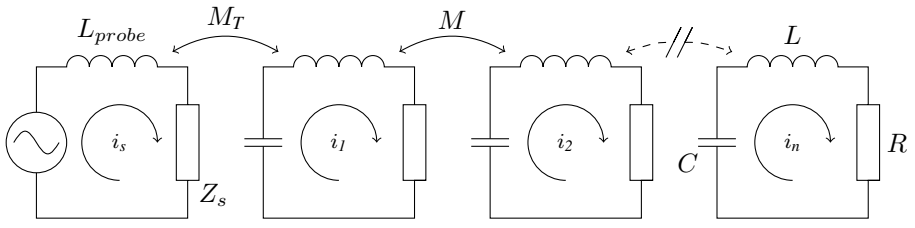


Figure 3.16 – A MI waveguide with n elements with each containing an inductance L, a capacitance C, and resistance R. The first element is coupled to a probe of inductance L_{probe} by a coupling M_T. The probe itself contains a source, V_s, and a resistive load Z_s.

Syms et al. have already devised a method to estimate the s_{11} between a MI waveguide and its termination [50]. This is done by first calculating the reflection coefficient, ρ, which for traditional transmission lines is given by

$$\rho = \frac{Z_L - Z_0}{Z_L + Z_0}, \tag{3.41}$$

whereby, of course, Z_L is the impedance of the load and Z_0, the characteristic impedance of the transmission line. However, (3.41) does not suffice in this situation as ρ is given by the ratio of the reflected current to incident current and the expression for these is different to that of traditional transmission lines. For MI waveguides, ρ is given by

$$\rho = \frac{-(Z_L - Z_0)}{Z_L + {Z_0}^*}, \tag{3.42}$$

where Z_L is still the impedance of the load, Z_0 is the characteristic impedance of a MI waveguide given by (2.18), and ${Z_0}^*$ its complex conjugate.

Following the example given in Figure 3.16, the voltage-current relationships in the probe and first loop are

$$ZI_1 + j\omega M_T I_s + j\omega M I_2 = 0, \tag{3.43}$$

$$(Z_s + j\omega L_{probe})I_s + j\omega M_T I_1 = 0, \tag{3.44}$$

where Z is the impedance of an element, composed of R, L, and C. By rearranging (3.44) to get I_s in terms of I_1, the reason for this shall be evident later, one gets

$$I_L = -\frac{j\omega M_T}{Z_s + j\omega L_{probe}} I_1. \tag{3.45}$$

Then by substituting (3.45) in to (3.43), to eliminate I_s, one arrives at

$$ZI_1 + j\omega M_T (I_2 - \frac{j\omega M_T}{Z_s + j\omega L_{probe}} I_1), \tag{3.46}$$

which can be rearranged as

$$(Z + \frac{\omega^2 {M_T}^2}{Z_s + j\omega L_{probe}})I_1 + j\omega M I_2. \tag{3.47}$$

Where one can see that the current loop associated with the source load, Z_s, has been transformed into an impedance that can be considered as part of its adjacent (the last element in the MI waveguide) loop. The load, Z_L, can now be defined as

$$Z_L = \frac{\omega^2 {M_T}^2}{Z_s + j\omega L_{probe}}. \tag{3.48}$$

Now when (3.48) is substituted into (3.47), and by taking the current in the n^{th} element to be formed of two travelling waves, just as in the case for a conventional transmission line, to be

$$I_n = I_I e^{-jnkd} + I_R e^{jnkd}, \tag{3.49}$$

where I_I and I_R are the magnitudes of the incident and reflected waves respectively. Syms et al. arrive at the expression for the reflection for MI waveguides given in (3.42).

So the probe has been transformed into an impedance within the first element as shown in Figure 3.17.

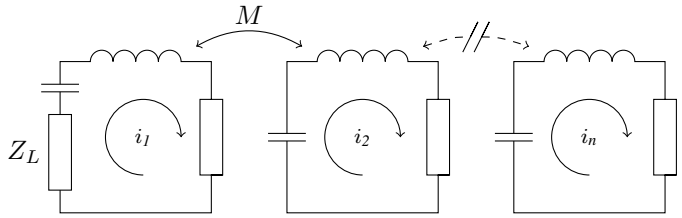


Figure 3.17 – A MI waveguide composed of n elements, with the input probe modelled as an impedance, Z_L, within the first element.

By using the above method, one can also create an effective impedance for an infinite MI waveguide, and use expression (3.41) to estimate the reflection as seen from the VNA.

The method follows a similar route, however instead of converting the loop containing the source load into an effective impedance in the first element of the MI waveguide, one converts

the MI waveguide into an effective impedance for the current loop containing the source load. In circuit element terms, the goal is to turn Figure 3.16 into Figure 3.18.

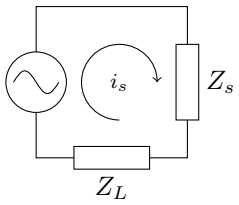


Figure 3.18 – Diagram showing a probe with a MI waveguide modelled as an impedance, Z_L, within the source's current loop.

At first, one may think this to be complicated, however it must be remembered than an infinite MI waveguide has a characteristic impedance that is given by (2.18). Thus, Figure 3.16 can be simplified to Figure 3.19.

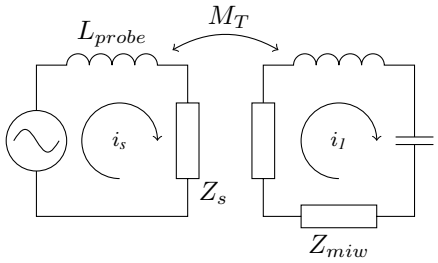


Figure 3.19 – A simplification of Figure 3.16 whereby the characteristic impedance of a MI waveguide, Z_{miw}, replaces the discrete elements making up the waveguide.

Again, just as in (3.43) and (3.44), the current-voltage relationships are written for the loop containing the VNA load and the element it couples to giving (3.50) and (3.51) respectively

$$0 = (Z_s + j\omega L_{probe})I_s + j\omega M_T I_1, \tag{3.50}$$

$$0 = (Z + Z_{miw})I_1 + j\omega M_T I_s, \tag{3.51}$$

where Z_{miw} is the characteristic impedance of a MI waveguide given by (2.18). Again, applying the previous method, express I_1 in terms of I_s by rearranging (3.51)

$$I_1 = -\frac{j\omega M_T}{Z + Z_{miw}} I_s, \tag{3.52}$$

then substituting (3.52) into (3.50)

$$0 = Z_s + j\omega L_{probe} + \frac{\omega^2 {M_T}^2}{Z + Z_{miw}}, \tag{3.53}$$

whereby it can be seen that the load impedance, Z_L, that one would use in (3.41) would be

$$Z_L = j\omega L_{probe} + \frac{\omega^2 {M_T}^2}{Z + Z_{miw}}. \tag{3.54}$$

CHAPTER 4

EXPERIMENTS AND ANALYSIS

It can be imagined that a high capacity would be desirable from the system. As discussed in Section 2.4, there are a few main factors which affect the capacity of an MI data transfer system. The equation for the capacity of a MI waveguide is given by

$$C = \int \log_2(1 + s_{21} \times SNR_{in})\mathrm{d}B, \tag{4.1}$$

where C is the capacity, s_{21} is the transfer function, SNR_{in} is the SNR at the transmitter, and the integral is taken over a chosen bandwidth, usually the MI passband given by (2.16) and (2.25) for one- and two-dimensional MI waveguides respectively.

As discussed in Section 2.4, the reason why $s_{21} \times SNR_{in}$ is used is because this is equal to the SNR at the receiver, as the latter quantity cannot be deduced from experiment, so a SNR at the transmitter has to be assumed. So from equation (4.1) it can be seen that the factors that affect the channel capacity are the bandwidth, and s_{21}. The factors that affect bandwidth are the inter-element coupling, κ, and the resonant frequency, ω_0.

One might initially think that an arbitrarily high ω_0 would be desirable, however it is vital that the effects of radiation be insignificant as retardation has a substantial effect on MI waves

[54]. Thus it is important that the resonators remain electrically small, so that radiation losses are minimized according to the radiation resistance, R_{rad}. For a circular loop of radius a, R_{rad} is given by [55]

$$R_{rad} \approx 197 \left(\frac{a}{\lambda}\right)^4. \tag{4.2}$$

The majority of previous work has ignored the effect of retardation as the resonators used are sufficiently electrically small to allow this [54, 56, 57].

The s_{21} is affected by the terminal coupling κ_x, and the MI waveguide attentuation α, which is in turn affected by the the inter-element distance d, the inter-element coupling κ, and the quality factor of the individual resonantors Q.

Evidently, to achieve the greatest channel capacity, one wishes to maximise both bandwidth and s_{21}, and hence all the above factors must be taken into consideration when designing an MI waveguide for data communications.

4.1 Element Characterization Methods

It was decided that element characteristrics, ω_0 and Q, would be obtained by measuring the transmission characteristics. This was initially due to the simplicity of the original method used to determine the aforementioned characteristics.

To measure an element, it was placed between two loop probes, made from semi-rigid RG402/U microwave cable, connected to ports on a HP 8753ES VNA which were separated from the board or the plane of the element by various heights. The VNA is controlled by a computer via a general purpose interface bus (GPIB) to universal serial bus (USB) interface. The printed circuit board (PCB) used has a thickness of 1.6 mm, and balsa wood spacers of 1.9 mm, or 3.8 mm thicknesses were used to space the element being measured from the loop probes. The layout is demonstrated in Figure 4.1

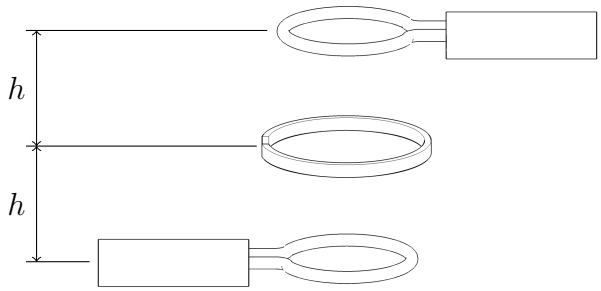


Figure 4.1 – An example configuration used when measuring resonator parameters. The resonator is placed in between two loop probes, by the same distance h to each probe, that are conneted to a VNA (omitted).

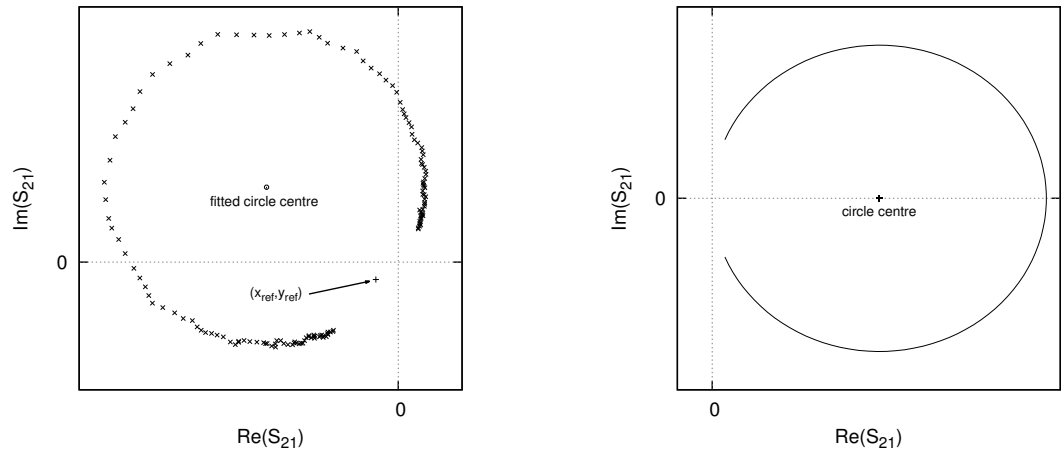
The VNA then either measured the log magnitude or the real and imaginary components of the s_{21} with 1601 points in a frequency range that encompassed the expected resonant frequency, f_0.

The first method used was the 3dB method [58], whereby the frequency of the peak s_{21} was used as the f_0. To get the Q, first the frequencies at -3dB (half power) either side of ω_0 (peak transmission) were also measured, and their difference taken giving Δf_{3dB}, and Q was derived according to equation (4.3),

$$Q = \frac{f_0}{\Delta f_{3dB}}. \tag{4.3}$$

Whilst simple, this particular method does have its drawbacks as one cannot couple too strongly with the element as the VNA load will load the element, causing a lower Q than reality or coupling too weakly will have the opposite effect [59]. Another issue is the limited resolution with which the frequency range is taken, this can lead to the 3dB points being in between measured frequency points. This issue can be crudely accounted for by making a linear interpolation of the 3dB point should it lie between two measured frequency points. But as one can imagine this method is subject to noise also.

Another method adopted is the Phase versus Frequency fit [58–60]. This requires the measurment of the real and imaginary frequency response, and a typical set of data is given in Figure 4.2a.



(a) *(b)*

Figure 4.2 – Typical complex s_{21} data, with reference point and fitted circle centre (a). Illustration of ideal s_{21} data (b).

The ideal set of data is shown in Figure 4.2b, the actual data is different to this due to the cables that are attached between the loop probes and VNA creating a phase shift, and the coupling between the probes offsets the centre of the circle.

First the data must be shifted into the canonical position, this is done by fitting a circle to the data. However, as the data is more subject to noise further away from resonance, a weighting is assigned to the data points. A reference point is taken, (x_{ref},y_{ref}), between the first and last data points, this is used to weight points closer to resonance more than those further away. These weights are given according to (4.4)

$$w = [(x_{ref} - x_i)^2 + (y_{ref} - y_i)^2], \tag{4.4}$$

whereby (x_i,y_i) are the data points. Then the data is fitted to a circle of the form (4.5),

$$r^2 = (x - x_c)^2 + (y - y_c)^2, \tag{4.5}$$

where r is the circle radius and (x_c,y_c) is the coordinate of the circle centre. This is done by a weighted least squares fit using the weights given by (4.4). From the fitted curve, the circle

centre and its angle to the origin are used to rotate the data such that it its centre now lies on the real axis much like the curve shown in Figure 4.2b. Now, a weighted non-linear least squares fit of its phase versus frequency is taken according to (4.6),

$$\theta(f) = \theta_0 + \tan^{-1}\left[Q\left(\frac{f}{f_0} - \frac{f_0}{f}\right)\right], \tag{4.6}$$

whereby the phase at resonance, θ_0, f_0, and Q are estimated by the fit. This was achieved using MATLAB's `lsqnonlin` function. Example data and its fit are shown in Figure 4.3.

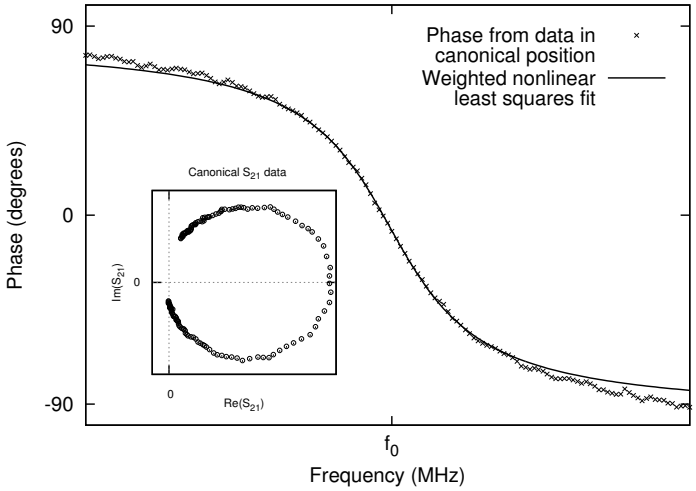


Figure 4.3 – Example phase versus frequency data, and its fit, the complex s_{21} data from which the phase versus frequency data is derived (inset).

The last method used was one which involves the Impedance matrix as discussed in Section 3.1. The arrangement of Figure 4.1 can be modelled as Figure 4.4 and its impedance matrix is given by (4.7),

$$\begin{pmatrix} Z_s + j\omega L_{probe} & j\omega M_T & j\omega M_{probe} \\ j\omega M_T & R + \frac{1}{j\omega C} + j\omega L & j\omega M_T \\ j\omega M_{probe} & j\omega M_T & Z_s + j\omega L_{probe} \end{pmatrix}. \tag{4.7}$$

Evidently (4.7) requires some initial estimates of all the parameters involved. Those being the element characteristics, R, L, and C, the resistance, inductance and capacitance respectively,

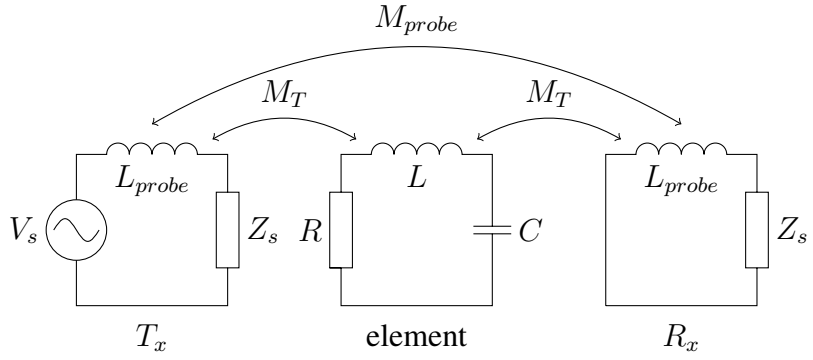


Figure 4.4 – The equivalent circuit layout of Figure 4.1, with two loop probes of inductance L_{probe}, and loads of Z_s each, coupled to each other by coupling M_{probe}, and a source in one probe of V_s. Each probe is coupled to M_T to the element which has and inductance of L, capacitance of C, and resistance of R.

and the couplings between the probes and the probe to the resonator, M_{probe} and M_T respectively. As the s_{21} is desired, the square root of the ratio of the power out to power in must be known. As much as V_s is unknown, it is the ratio of the power taken out by the Z_s in the receiver to the power given by V_s that matters, so for the purpose of simulation, V_s is set as 1 V. The inverse of the impedance matrix given by (4.7) is then found for the frequency range considered and multiplied by the voltage vector to get the currents in each of the loops. The power out and power in are then calculated according to (3.9) and (3.8).

The factors L, M_T, and M_{probe} can be estimated with the program FastHenry [61]. FastHenry is a program that calculates the frequency-dependent self inductance and mutual inductances of three-dimensional structures. One has to specify the geometry of objects as nodes connected by parallelepipeds of any given height and width, along with the conductance for the material. The frequencies at which the self and mutual inductances are to be determined must also be specified. Unfortunately circular objects, such as the loop probe, must be approximated with numerous parallelepipeds. However, there is a trade off between the number of parallelepipids to approximate circular objects and the speed with which FastHenry can calculate the objects' self or mutual inductances.

Another method to obtain the mutual inductances between two wires would be to use the double integral formula given by (2.5). However this method assumes that the elements are composed of infinitely thin wires, however when elements are close to each other, this can

give higher than expected values of mutual inductance. Revisiting the equation for mutual inductance (2.5)

$$M = \frac{\mu_0}{4\pi} \oint_{element\,1} \oint_{element\,2} \frac{\mathbf{ds_1}.\mathbf{ds_2}}{|\mathbf{R_{12}}|}, \qquad \text{(2.5 revisited)}$$

one can see that as the distance between the current elements, $\mathbf{R_{12}}$, decreases, the fraction $\mathbf{ds_1}.\mathbf{ds_2}/\mathbf{R_{12}}$ increases in magnitude. This is an issue as the physical elements cannot be considered to be infinitesimally thin, and the paths that the current elements, $\mathbf{ds_1}$ and $\mathbf{ds_2}$, can take can vary. A simple example would be the mutual inductance between two square split rings such as the one shown in Figure 4.5.

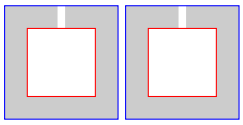


Figure 4.5 – Two square SRRs in close proximity, the outer most current element in blue, and the inner most in red.

In such an example, if it was assumed that the current were to travel predominantly along the outer surface of the rings, as shown in blue, then this would lead to a higher calculated mutual inductance via (2.5) than if one were to assume that current travels along the inner surface, shown in red. The effects of this are negligible when objects are sufficiently far apart, and can also be ignored should the wire, or track, be sufficiently thin in comparison to any other length. However for the typical element separations of interest the effect is still significant, and so the path along which the current travels should be either decided upon or calculated. Again, there is a trade off here between accuracy and speed, so an intermediate solution can be used whereby FastHenry is used to calculate the mutual inductance at several elements separations, and then finding an element radius to match those values using (2.5).

In the past, the resonators used for MI waveguides have either had their capacitance dictated by discrete components [21, 41, 46, 62] or geometry [50, 63, 64]. For resonators that utilize discrete components to make up their capacitance, a tolerance is associated with their

value and this typically depends on the dielectric used. For resonators that derive their capacitance from their geometry, the tolerance will be based upon the method of fabrication.

As discussed in Section 2.4, the resistance of a resonator is most likely to come from the skin effect and the equivalent series resistance (ESR), this arises due to dielectric losses, of the capacitive element.

4.2 SQUARE ELEMENT CONVENTIONAL MAGNETO-INDUCTIVE WAVEGUIDE

As discussed in Section 2.4, the easiest way to increase channel capacity is to maximise the inter-element coupling, κ. Previous work [21] utilized circular SRRs with a f_0 of 45 MHz. The structure used was composed of a 10-element line with resonant terminals as shown in Figure 4.6. The elements were spaced such that they were nearly in contact, giving a κ of -0.125. The terminals coupled to the array with a κ_x of 0.23 in accordance to (2.33) leading to a peak s_{21} of -7.74 dB.

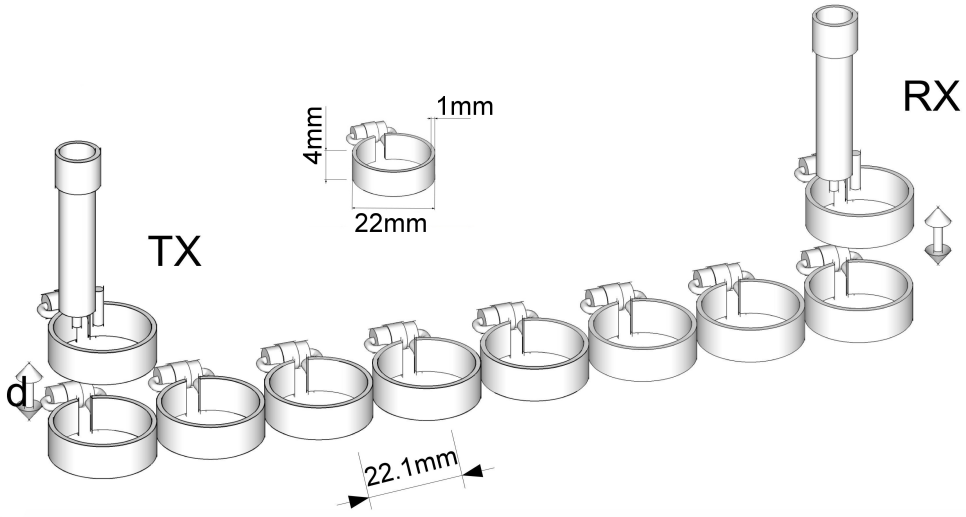


Figure 4.6 – A 10-element MI waveguide composed of SRRs that are in near contact with each other. Each element has the dimensions shown and both terminals are of the parallel resonant type and share the same height, h, above the waveguide. Taken from [21].

As the in-plane coupling of such circular SRRs cannot be improved upon compared to this previous work, it was decided that a square element be used, as it is more space filling and would thus yield a higher κ. The dimensions of this element are given in Figure 4.7.

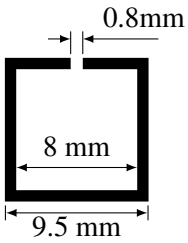


Figure 4.7 – Schematic of a square ring resonator with its dimensions. A 0603 surface-mount capacitor is designed to be soldered accross the 0.8 mm gap.

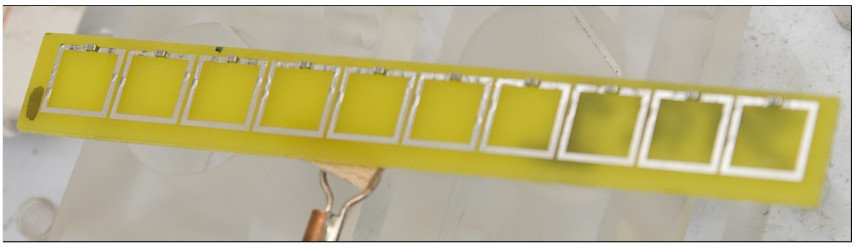
It was decided that the structure would be fabricated on PCB for convenience, and surface-mount capacitors soldered across the gap to the reduce the potential for variance of element characteristics due to the use of capacitors with leads [65]. Using FastHenry, the inductance is estimated to be 20.49 nH, and the capacitor had a value of 22 pF $\pm$ 5%, with the resultant resonant frequency expected to be between 231.34–243.21 MHz.

The goal here is to first investigate the optimum terminal-waveguide coupling for peak $|s_{21}|$ for a system with two terminals and a one-dimensional MI waveguide, and also to make a comparison to the coupling that gave rise to the highest capacity. Then to do the same for various transmitter and receiver configurations for a two-dimensional MI waveguide. Then to assess the affect of a third "blocking" terminal on both one- and two-dimensional MI waveguides.

A 10-element one-dimensional MI waveguide, with 10 mm spacing between element centres (0.5 mm between edges), and a 36-element two-dimensional MI waveguide, with element centres spaced at 10 mm between both rows and columns, was made.

In order to extract the parameters of the individual resonators, they had to first be sufficiently isolated from each other. To that end, adjacent resonators were de-tuned by soldering a wire temporarily across the capacitor. This was deemed sufficient to minimize the effects coupled resonators would have upon the element being measured. However, to save time, not all the other resonators would be de-tuned at once, instead, the resonators to be measured would have at least two de-tuned resonators in between them as shown in Figure 4.9.

(a)



(b)

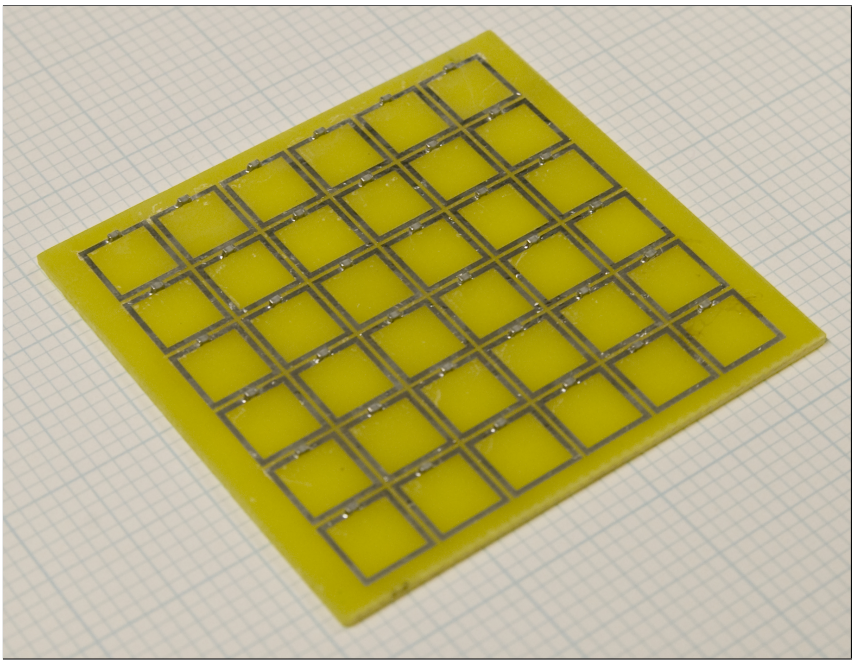


Figure 4.8 – Photograph of a 10-element MI square element waveguide fabricated on PCB (a) with 10 mm between element centres, photograph of a 36-element in a 6-by-6 arrangement fabricated on PCB (b) with 10 mm spacing between both row and column centres, both with surface-mount capacitors soldered onto each element. All copper track was also tinned.

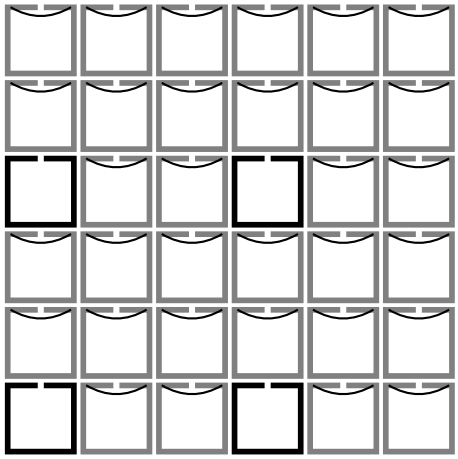


Figure 4.9 – 6-by-6 square element two-dimensional MI waveguide with the elements to be measured in black, and the grey elements have their capacitors shorted via wire shown in black.

To measure the parameters, the element being characterized was placed between two loop probes of 7.25 mm diameter, the wire of the probes had a diameter of 0.036 in (0.9144 mm). These probes were held in place by perspex clamps and acrylic rods which were screwed into a perspex backboard. The backboard has an array of holes, tapped out for M6 threads specified by the International Organization for Standardization (ISO) 261 International Standard, spaced every 25 mm in the x and y directions. The MI waveguides would be kept above this backboard by either balsa wood or toy plastic bricks. The probes were placed 5.4 mm away from the suface of the element's copper track, this also took into account the 1.6 mm thickness of the PCB. This separation was chosen for convenience as there were balsa wood spacers that could be used to reliably ensure the correct probe-resonator separation. A HP 8753ES VNA was used to then measure the log magnitude s_{21} at 1601 points between 210–280 MHz.

It was decided that, for simulation, the variation of the resonators would also be modelled, not by applying a variance to any of the resonator parameters, but by including the data measured from the fabricated resonators. This was because if a parameter was to be varied according to (2.31) in simulation, either the simulations would not be consistent between runs as the resonator parameters vary each time, thus making it impossible to compare any two instances of simulation. If one were to create a static variation using (2.31), it was found that the exact placement of element variation was important as this would change the apparent behaviour of the MI waveguide [65].

The one-dimensional MI waveguide as shown in Figure 4.8a had its resonators numbered 1 to 10 starting from the left side. The two-dimensional waveguide as shown in Figure 4.8b had its resonators numbered in the matrix (row,$column$) style starting from the bottom left. Table 4.1 shows the characteristics for the elements of the one-dimensional MI waveguide, Tables 4.2 and 4.3 show the f_0 and Q for the resonators that make up the two-dimensional MI waveguide respectively.

Both these MI waveguides have an element centre to centre spacing of 10 mm, which means that there is a spacing of 0.5 mm between the edges of elements. As mentioned in Section 4.1, as the copper track that makes up the element is clearly not thin compared to the element's

Resonator	f_0 (MHz)	Q
1	237.96	84.58
2	242.03	76.76
3	240.41	80.98
4	236.56	85.78
5	240.58	82.06
6	236.78	84.66
7	239.62	81.34
8	242.90	78.03
9	240.10	81.42
10	237.69	84.65

Table 4.1 – Resonant frequency, f_0, and quality factor, Q, for each of the resonators in the one-dimensional MI waveguide.

f_0 (MHz)		Column					
		1	2	3	4	5	6
Row	1	241.33	239.49	242.59	240.71	239.49	237.26
	2	243.49	237.52	238.48	240.71	242.11	241.94
	3	241.33	238.58	243.56	239.05	242.38	239.49
	4	237.65	238.70	241.41	241.02	241.59	240.26
	5	239.09	241.15	238.70	240.71	243.73	241.59
	6	237.26	238.13	240.28	240.59	242.77	239.27

Table 4.2 – Table of the resonant frequency, f_0, of the individual resonators in the two-dimensional MI waveguide.

Q		Column					
		1	2	3	4	5	6
Row	1	75.70	71.76	73.61	70.40	72.89	85.12
	2	74.83	82.98	72.61	64.46	74.05	71.05
	3	77.80	78.74	77.40	75.23	75.98	76.70
	4	83.80	77.74	72.99	70.08	78.58	75.18
	5	76.66	79.24	73.23	63.84	73.62	72.67
	6	84.85	76.68	76.93	76.25	69.48	73.18

Table 4.3 – Table of the quality factor, Q, of the the individual resonators in the two-dimensional MI waveguide.

width; when using the double integral formula presented in (2.5) the path on which the current is taken to travel impacts the mutual inductance calculated despite the element centres remaining the same. Figure 4.10 shows how the coupling, κ, varies, for two elements spaced with their centres 10 mm apart, whilst the sides of the square elements (and thus the current path) vary between the smallest and largest value they can take (8–9.5 mm).

Figure 4.10 shows that whilst maintaining the same centre-centre spacing of 10 mm, κ

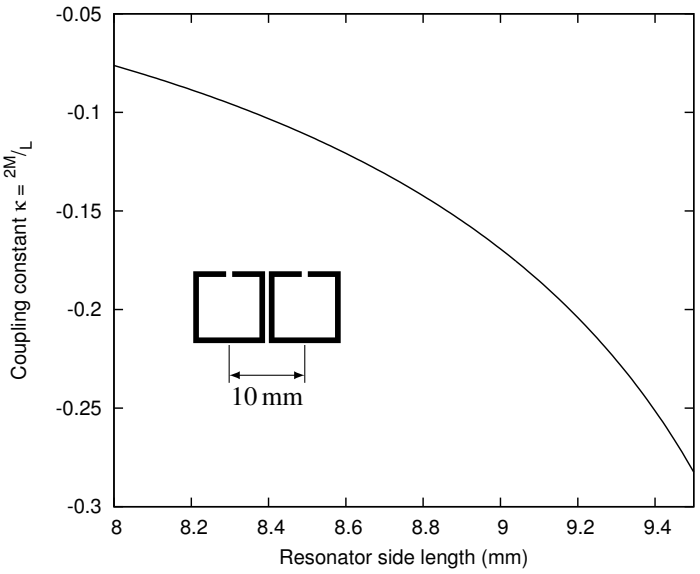


Figure 4.10 – The coupling calculated by using the double integral formula presented in (2.5) for two square elements with their centres spaced 10 mm apart, with the resonator's side length varied between 8–9.5 mm.

changes between -7.62×10^{-2} and -0.283 when the resonator side length is changed between 8 mm to 9.5 mm. If the in-plane coupling for the waveguide were taken to be in between these values, then according to the formula for the bandwidth of a one-dimensional MI waveguide given by (2.16), the expected bandwidth would be anywhere between 18.13–71.24 MHz.

In order to decide the appropriate side length of resonator for mutual inductance calculations, FastHenry was used to calculate the mutual inductance of two squares of the dimensions shown in Figure 4.7 with their centres spaced 10 mm apart. This gave a κ of -0.150 and it was found that when using (2.5), this would be equivalent to having a resonator 8.856 mm wide. This value of κ gives an expected one-dimensional MI bandwidth of 36.32 MHz and a 75.92 MHz two-dimensional MI bandwidth.

To compare calculated values of mutual inductance with experimentally derived ones, it was decided that only a few key co-planar two-element arrangements would be considered and a range of vertical resonator separations. The co-planar arrangements are shown in Figure 4.11, these were considered as they are the various neighbour-couplings that have to be considered in the one- and two-dimsional MI waveguides.

PCBs were made of each two-element arrangement, and whilst one element was being

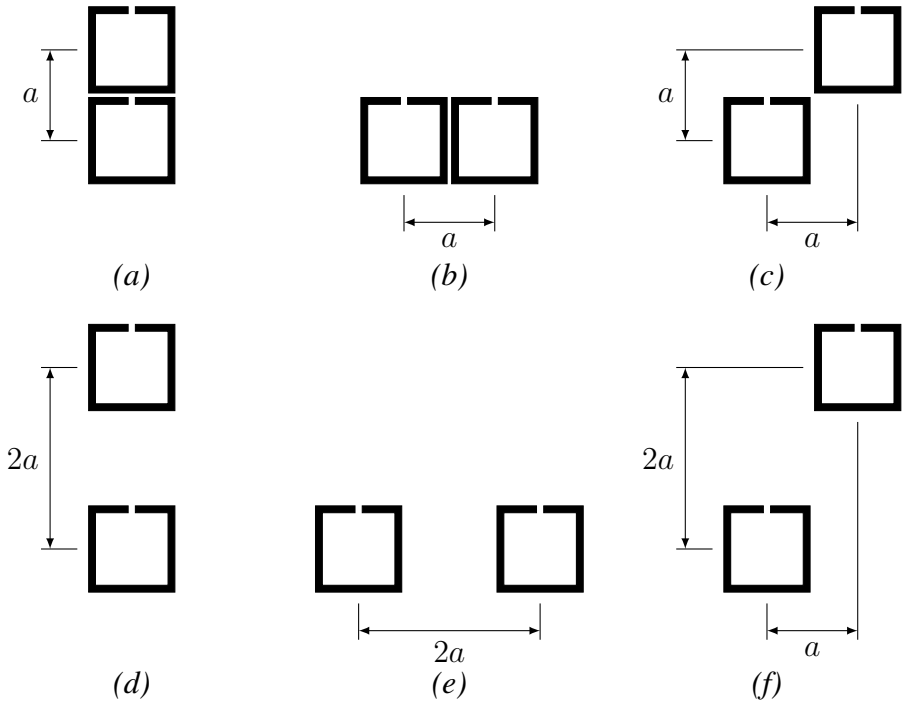


Figure 4.11 – Arrangement of the various neighbour couplings measured where a is the period and is equal to 10 mm.

measured, the other would have its capacitor shorted with a wire soldered across it in order to detune the element. The element being measured would then be placed between two loop probes of 7.25 mm diameter, each probe would be 5.4 mm away from the surface of the resonator. However, a thru calibration would be performed with just the probes in place, and then the element put into position. The calibrated s_{21} was then taken as the average of 16 scans of 1601 points between 210–280 MHz. The element parameters, f_0 and Q, were then extracted via the 3dB method described in Section 4.1. The measurement of the mutual inductance in each of the arrangements shown in Figure 4.11 was done in a similar fashion. The various arrangements were always orientated such that the capacitors were always the most northerly in the squares, then the element which was either the most southerly or easterly was numbered element 1 in the arrangement. The aforementioned loop probes were then placed 5.4 mm either side of the surface of the 1$^{\text{st}}$ element, then a thru calibration performed without the elements, and the elements replaced, with the centre of the loop probes and the centre of the 1$^{\text{st}}$ element aligned vertically by eye. As there are two resonators in the system, there are two expected resonances, and these can be put into (2.9) to get the mutual inductance.

For the arrangements presented in Figures 4.11e and 4.11f, it was not possible to derive the mutual inductance from experiment as it was not possible to distinguish two resonances from the s_{21} data. Table 4.4 compares the experimental and calculated values of mutual inductance for the arrangements depicted in Figures 4.11a–f.

		Configuration					
		a	b	c	d	e	f
							
κ	*Experimental*	-0.133	-0.130	-2.52×10^{-2}	-1.59×10^{-2}		
κ	*FastHenry*	-0.123	-0.150	-2.95×10^{-2}	-7.37×10^{-3}	-9.51×10^{-3}	-5.84×10^{-3}
κ	*Double integral*	-0.149	-0.149	-3.32×10^{-2}	-8.80×10^{-3}	-8.78×10^{-3}	-6.11×10^{-3}

Table 4.4 – Table comparing with the experimental and calculated values of κ for the nearest neighbour configurations a – f displayed in Figures 4.11a – f.

For FastHenry, there's a difference between between the first two configurations, this is most likely due to the gap that is left for the capacitor. As the main contributor to the magnitude of mutual inductance is from the wires that are closest to each other. The difference between the pairs of wires that are closest to each other in configurations a and b are that those in a feature a break for the capacitor. When using the double integral formula, the gap for the capacitor was not modelled, and so the κ for configurations a and b were calculated to be the same. That aside, there is clearly quite a significant difference between experimental and both forms of calculated κ values. These differences most likely occured due to the variance in resonator characteristics and probe-resonator interaction, but further study would be needed to ascertain the exact reason.

For the vertical separation comparison, the experiment was set up as shown in Figure 4.12. Each 7.25 mm diameter loop probe would be attached to a 5.8 mm balsa wood spacer via adhesive tape, and this in turn was attached to the PCB of a square resonator via the same method. The loop and resonator were centred upon each other by eye. One of the probes was attached to the arm of a computer-controlled electronic stage mover as shown in Figure 4.13, and the other held in place on the perspex backboard. The stage mover was configured to move in only two axes for any given experiment and is capable of moving in 25 μm steps. The surfaces of the opposing resonators were first separated by a spacer of known thickness so that their separation was known, then the mobile probe was moved such that their separation was

30 mm, and was brought to 1 mm separation in 0.1 mm steps. At each separation, the complex s_{21} was recorded at 1601 points between 150–350 MHz by a HP 8753ES VNA. The resonators had to be rotated 180° relative to each other in order to achieve the minimum vertical separation that was measured as otherwise the capacitors of the resonators would come into contact[1]. The mutual inductance was then found according to equation (2.9) by finding the two resonances via MATLAB's regional peak finding function.

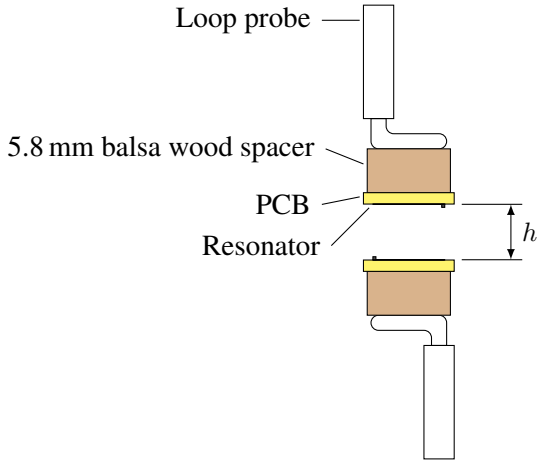


Figure 4.12 – Experimental layout of vertical mutual indutance. Two loop probes are attached to square resonators via double sided adhesive tape and 5.8 mm balsa wood spacers. The surfaces of the two resonators are separated by a height h.

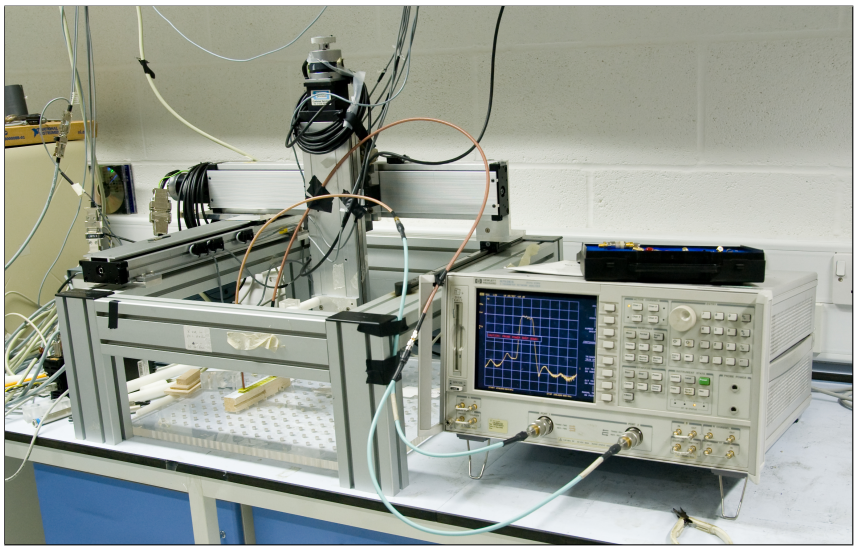


Figure 4.13 – Photograph of the computer-controlled electronic stage motor, configured to move in two axes at a time with a HP 8753ES network analyzer connected to two probes or terminals via 50 Ω coaxial cables.

Figure 4.14 compares the values of measured and calculated terminal-waveguide coupling

[1]The capacitors were 1.6 mm in length, 0.8 mm deep and 0.8 mm high.

constant κ_x for a vertical separation between 1.5–10 mm via (2.5). This range is shown as it best highlights the change in κ_x and it becomes difficult to discern the two resonances required to utilize equation (2.9) for greater vertical separations. The values of κ_x derived from experiment for vertical separations below 1.5 mm appeared to be the same, and were thus omitted. It is believed that the two resonators came into contact with each other as the spacers used for the initial calibrating separation were made of balsa wood, along with the spacers attached to the probe, and are slightly compressible. A discrepancy of approximately 10% can be seen between the calculated κ and that derived from experiment.

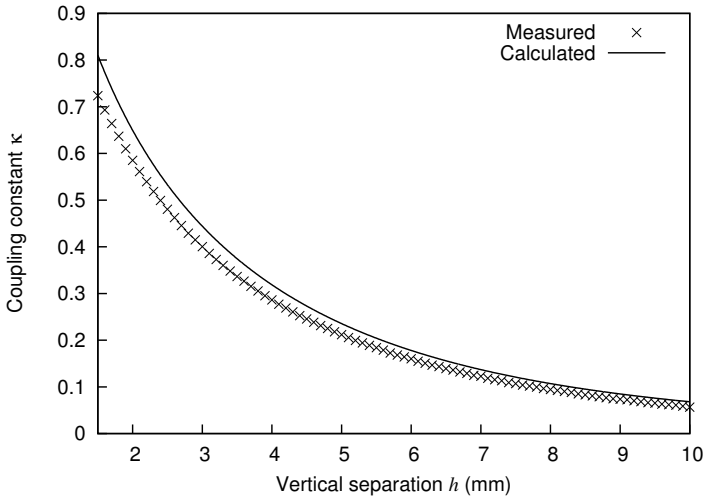


Figure 4.14 – Comparison between the measured and calculated, via the double intregal method (2.5), values of the terminal-waveguide coupling constant κ, against terminal height h.

4.2.1 OPTIMAL HEIGHT

Before making an assessment of the suitability of MI waveguides for multi-terminal set ups, the terminal-waveguide coupling must be decided upon. This is because, as stated in Section 2.4, there exists an optimum terminal-waveguide coupling in order to obtain the greatest transmission. It is also possible that the height at which maximum capacity is achieved may not be the same as that when the peak $|s_{21}|$ is achieved. Wherever capacity is calculated, a discrete verstion of equation (2.30) is used, and an SNR of 20 dB is assumed. This value was chosen as it was deemed to a be conservative minimum, and although the system itself is not similar to Wi-Fi, 20 dB is considered to be a minimum for good service.

4.2.1.1 ONE-DIMENSIONAL STRUCTURES

The experiment was set up according to Figure 4.15 where there are two resonant terminals, T_x and R_x, connected to a HP 8753ES VNA held above a 10-element one-dimensional MI waveguide. The terminals were fixed at the same height relative to each other, and were moved in 0.1 mm steps from 30 mm to 1 mm above the strip by a computer-controlled electronic stage motor as shown in Figure 4.13. The terminals were centred on elements at opposite ends of the MI waveguide.

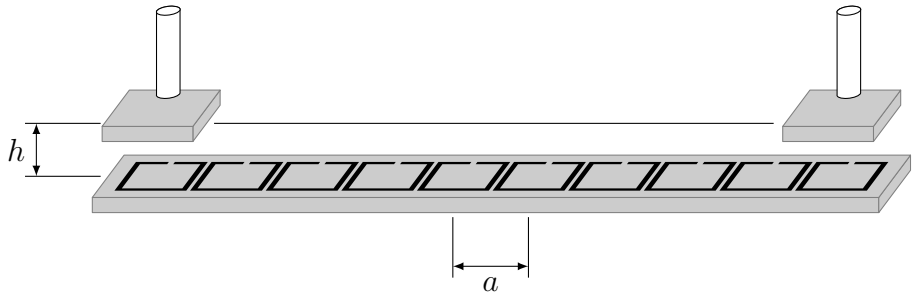
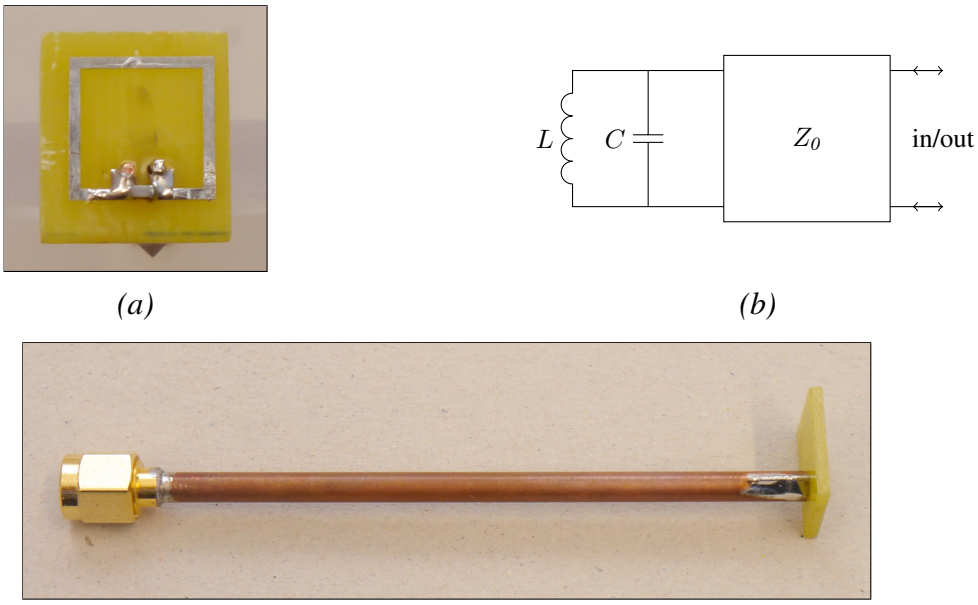


Figure 4.15 – A 10-element one-dimensional MI waveguide with a period of a, with terminals T_x and R_x above the waveguide by height h (capacitors omitted).

The resonant terminal, Figure 4.16, was composed of a square resonator with extra small tabs either side of the capacitor gap (Figure 4.16a) to provide extra space for holes to accommodate wires that connect the resonator to a length of RG402/U semi-rigid coaxial cable, terminated by a male SMA connector. Through one hole was the central conductor of the semi-rigid cable, and through the other was a wire of the same diameter as the central conductor, soldered onto the outer jacket of the semi-rigid cable. The terminals were rotated 180° relative to the resonators in the waveguide in order to allow the terminals to get to within 1 mm from the waveguide surface, as the surface mount capacitors of the elements and terminals would otherwise prevent this.

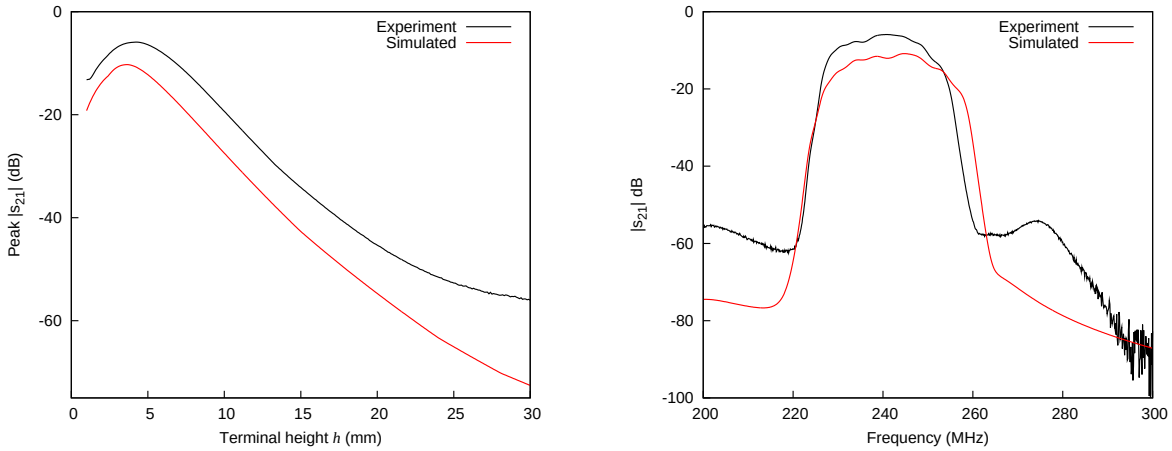
According to equation (2.33), the magnitude of the terminal-waveguide coupling, $|\kappa_x|$, should be approximately double the magnitude of the inter-element coupling, $|\kappa|$, for peak $|s_{21}|$. This gives $|\kappa_x|$ as 0.260 and 0.300 which, by consulting Figure 4.14, gives the optimum heights as 4.83 mm and 4.21 mm for the measured and calculated values of κ respectively.



(a) *(b)*

(c)

Figure 4.16 – Photograph of the end of the resonant square terminal (a), with the surface mount capacitor clearly displayed. Equivalent circuit diagram of the resonant square terminal (b), whereby L and C are the inductance and capacitance of the terminal and equal to that of an element, Z_0 is the characteristic impedance of the transmission line equal to 50 Ω. Photograph of the whole square resonant terminal showing the attachment of the resonant loop to a length of RG402/U semi-rigid coaxial cable terminated by a male SMA connector.



(a) *(b)*

Figure 4.17 – A comparison between experimental and simulated peak $|s_{21}|$ versus terminal height h, (a). The experimental and simulated transfer function for h = 4.3 mm, the experimentally determined height for peak $|s_{21}|$.

Figure 4.17a shows a comparison between the simulated and experimental variation of peak $|s_{21}|$ with terminal height h. It can be seen that, while their slopes agree until $h = 15$ mm, there is difference in magnitude. The decrease in slope at larger values of h is thought to be

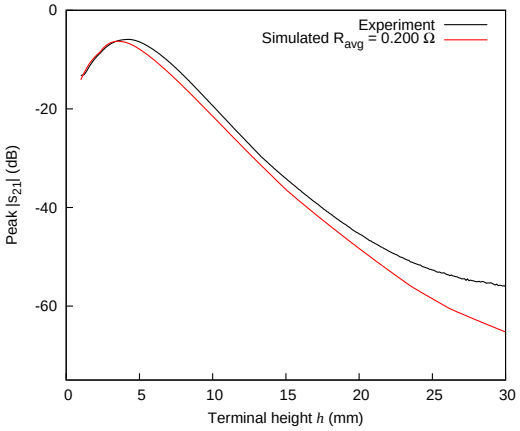
due to coupling of the terminals, but this is unlikely given the significant distance between the transmitter and receiver. The simulated curve is also shifted left in relation to the experimental curve. As the calculated inter-element coupling, κ, was higher than the experimental κ; the terminal-waveguide coupling, κ_x, would have to be larger, and thus the terminal would have to be closer to the waveguide. The higher calculated κ is also reflected in the broader simulated transfer function as shown in Figure 4.17b. The reduction in the simulated transfer function could potentially have been caused by incorrect resonator characterization. This is because the greatest cause of attenuation is due to the waveguide element resistances, R. These can be calculated from the measured quality factor of each resonator, Q, as given in (2.2). Figure 4.19c shows how R affects the peak $|s_{21}|$. The average R determined from resonator characterization is 0.376 Ω, but Figure 4.19c implies that it should be $\approx$0.200 Ω. This, in turn, implies a Q of $\approx$154 rather than the average Q of 82 obtained through experiments. This could potentially be due to the probe loading the element.

Figure 4.19a and Figure 4.19b show similar information to Figure 4.17, but with an adjusted value of element resistance. It can be seen that, with this change, the agreement between simulation and experiment is good. The differences are caused by the slightly different values of κ between experiment and simulation.

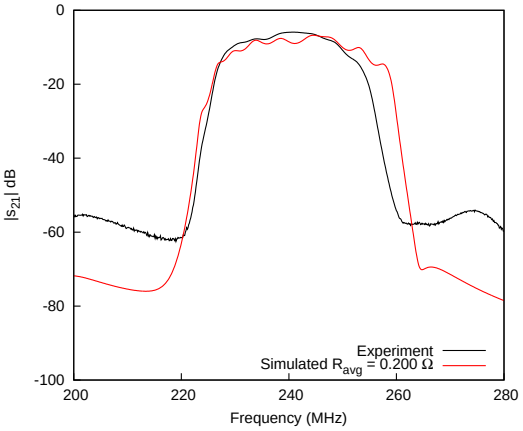
Figure 4.20 shows a comparison between the experimentally determined peak $|s_{21}|$ and capacity. It can be seen that the peak data capacity of the system does not have to correspond with the peak $|s_{21}|$. Figure 4.21a and Figure 4.21b show that, as they only have a difference in peak $|s_{21}|$ of only $\approx$0.5 dB, the transfer function at 3.3 mm is flatter and wider, leading to a higher capacity as the area under the transfer function is greater.

These findings, however, confirm the work of Stevens et al. [21] that optimum coupling for peak $|s_{21}|$ occurs when $|\kappa_x| \approx 2|\kappa_c|$ for the one-dimensional case. Figure 4.22 and Figure 4.23 help explain how the optimum coupling for peak $|s_{21}|$ arises and how it does not necessarily correspond to the maximum capacity.

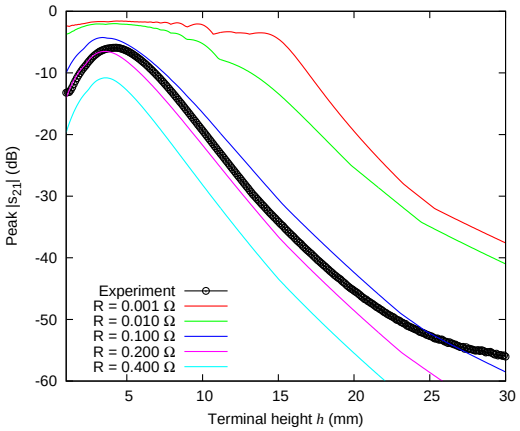
In Figure 4.22, it is very clear that MI waves only propagate in a pass band around a centre frequency. A peak $|s_{21}|$ of -5.90 dB was achieved with a terminal height of 4.3 mm.



(a)



(b)



(c)

Figure 4.19 – A comparison between experiment and simulated peak $|s_{21}|$ versus terminal height, h, with an adjusted value of element resistance, R, (a). The experiment and simulated adjusted transfer function for h = 4.3 mm, (b). Plot of peak $|s_{21}|$ against h, a comparison between experiment and simulations with varying values of R, (c).

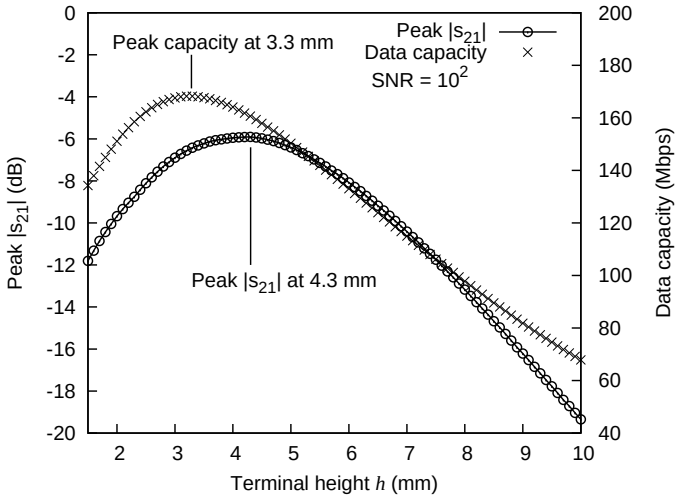
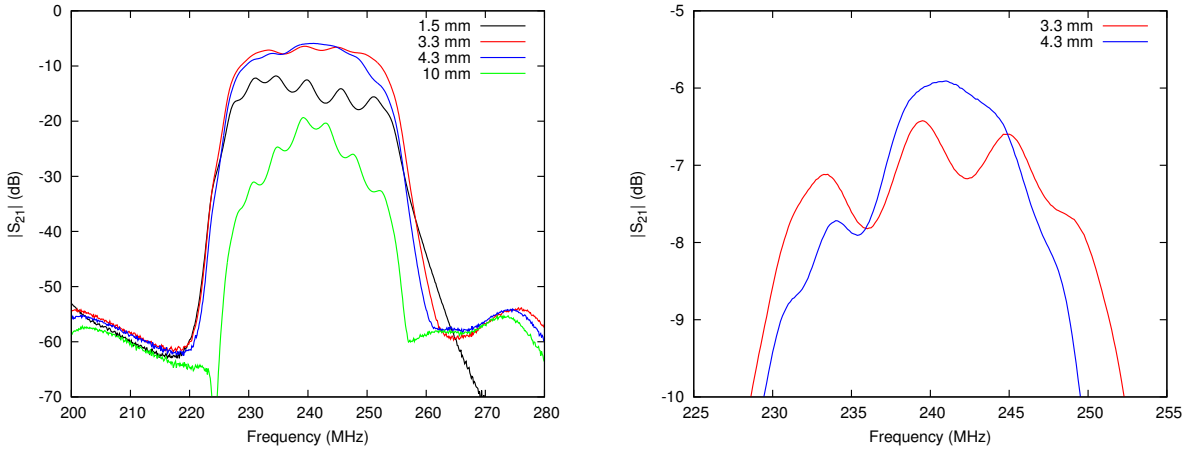


Figure 4.20 – A graph of experimentally obtained peak $|s_{21}|$ versus terminal distance h, and data capacity, with an SNR of 10^2 and a 37 MHz bandwidth centred around 239.46 MHz, versus terminal distance.



(a) *(b)*

Figure 4.21 – Graphs of $|s_{21}|$ versus frequency. (a) shows the transfer functions when the terminal height is 1.5 mm, 3.3 mm, 4.3 mm, and 10 mm. (b) is a subset of (a) showing the transfer functions at a terminal height of 3.3 mm and 4.3 mm in a reduced frequency and $|s_{21}|$ range.

This occurred at the point which the split resonances, due to axial coupling, and the MI wave band nearly coincide. Of course, the transmit or receive terminals do not couple exclusively to the terminal below. The transfer function over the ten-element strip and probes probably bears similarity to the response of the strip multiplied by the response of two axially coupled elements. This is most likely the reason that the transfer function when the terminal height is 3.3 mm is greater than when the terminal height is 4.3 mm. It can be seen from the dotted lines in Figure 4.22 that the split resonances grow further apart as the terminals get closer together.

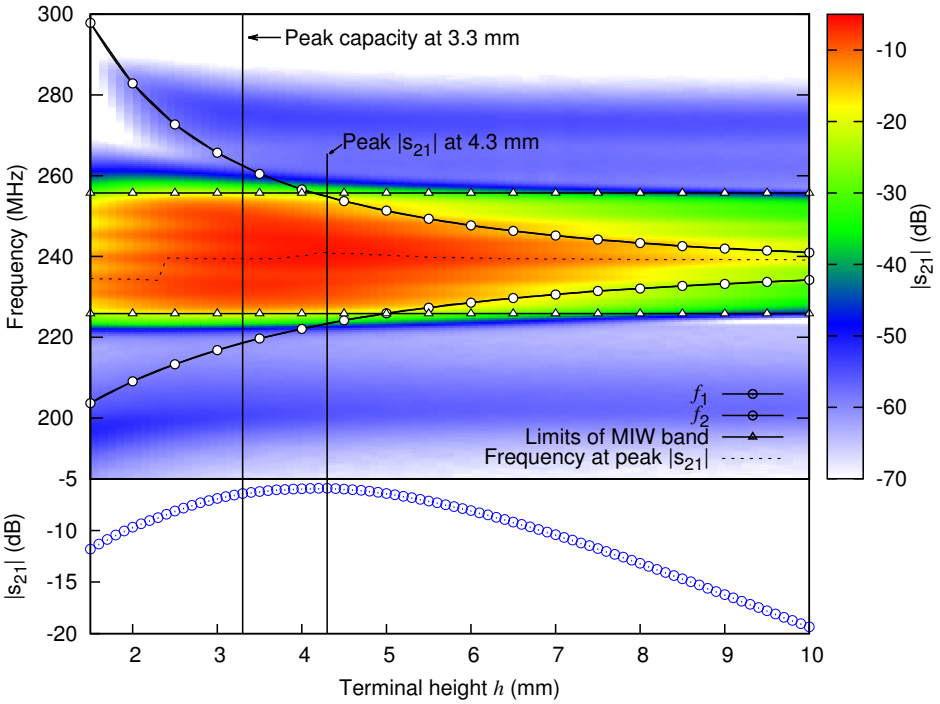


Figure 4.22 – A colour-map of experimentally obtained $|s_{21}|$ against frequency and terminal height h. The dotted lines correspond to the split resonances that occur due to two resonators coupling axially as discussed in Section 2.2. The triangularly dotted lines indicated the upper and lower limits of the MI wave band. The dashed line corresponds to the frequency at which peak $|s_{21}|$ was achieved at a given h. The lower graph displays peak $|s_{21}|$ against terminal height.

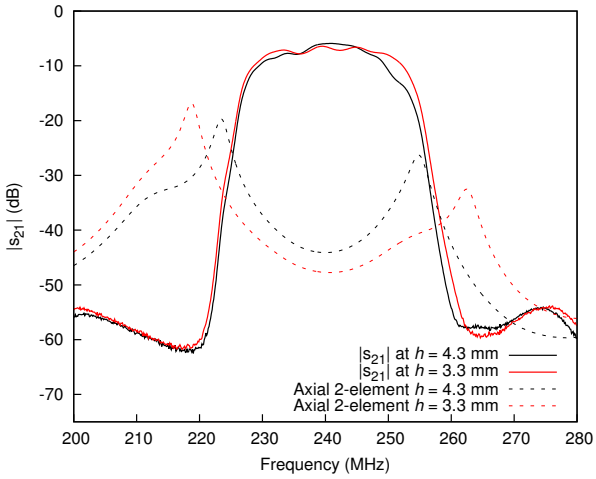


Figure 4.23 – A comparison between the transfer functions through a system with ten elements and the transfer function for two axially coupled elements where their vertical separation is 3.3 mm and 4.3 mm.

The transfer functions for these at 3.3 mm and 4.3 mm are given in Figure 4.23 by the green and blue lines respectively. It is likely that the greater split would result in a slight broadening of the response. While two elements in isolation would display these split resonances, so when

multiple elements couple together, multiple peaks are formed that are closer together; referring to Section 2.2, a system with two elements would show two resonances, thus a system with N elements may display N resonances [38]. The terminals however, do not couple with the same coupling as the elements in the strip, and this is likely to be the cause of the response broadening.

4.2.1.2 TWO-DIMENSIONAL STRUCTURES

For a two-dimensional MI waveguide, the variation of terminal placements is much greater than for a one-dimensional waveguide. For all configurations, terminal T_x was connected to port 1 of the VNA and terminal R_x was connected to port 2 of the VNA, both terminals were centred above an element of choice. Two sets of experiments were carried out, one where R_x was fixed above (6,6), and T_x was mobile, the other T_x was fixed above (1,1) and R_x mobile.

The s_{21} was measured at 1601 points between 150–350 MHz for terminal heights of 1–30 mm in 0.1 mm steps. For each configuration, the terminals were first brought to a known height above the MI waveguide by a spacer, then brought to 30 mm before proceeding with the measurements. The experimental layout is shown in Figure 4.24. In simulation the terminals were coupled to all the elements in the waveguide and this was done via the double integral method as given by (2.5).

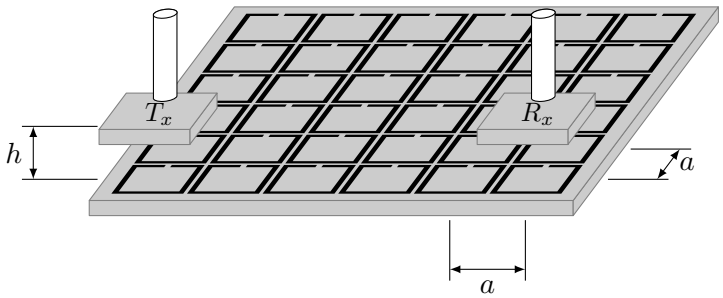


Figure 4.24 – Diagram showing experimental setup, two terminals, T_x and R_x connected to port 1 and 2 of the VNA respectively, are held at the same height h from the surface of the two-dimensional MI waveguide of period a in the x and y directions.

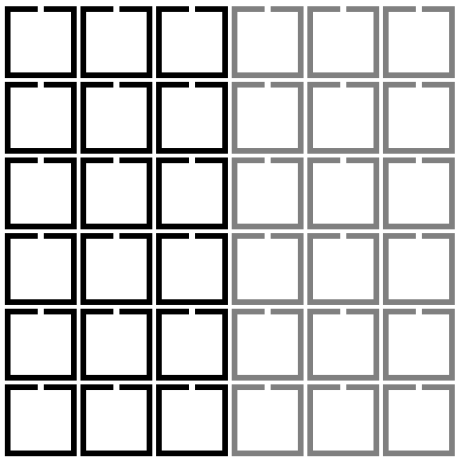


Figure 4.25 – With the receiver R_x at (6,6), the considered T_x positions are shown as the solid elements.

4.2.1.3 MOBILE TRANSMITTER

Figure 4.25 shows the T_x positions considered. Due to the physical layout of the experiment, it was not possible to bring the terminals within a couple of elements to each other. As the receiver, R_x was to remain in the corner, symmetry was expected around the diagonal, to ascertain this some measurements were taken on both sides of the diagonal. At the time, it was only decided a block from (1,1) to (6,3) was to be considered so that some symmetry, end to end performance, the effect of the proximity of the terminals to each other, and the anisotropic bandwidth might be observed.

The optimum terminal-waveguide coupling, $|\kappa_x|$, doubles in comparison to the 1-D case; for an in-plane κ of -0.123, this equates to a $|\kappa_x|$ of 0.492, and corresponds to a terminal height of 2.7 mm from the experimental points in Figure 4.14.

Figure 4.26 bears some interesting results. When the element resistances are $0.200\,\Omega$, there is good agreement with the experiment until 15 mm. The plateau of the experimental curve is most likely due to far field coupling. However, between 1–5 mm, both the red and dotted curves exhibit a second peak and looking at Figure 4.29, the dashed line shows which frequency is responsible for the peak $|s_{21}|$ at a given terminal height. It is possible that, as the transmitter gets closer to the array, the coupling to the off-axis nearest-neighbours changes from

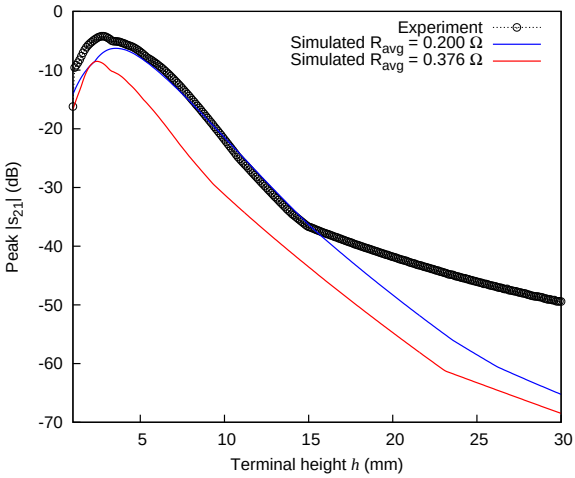
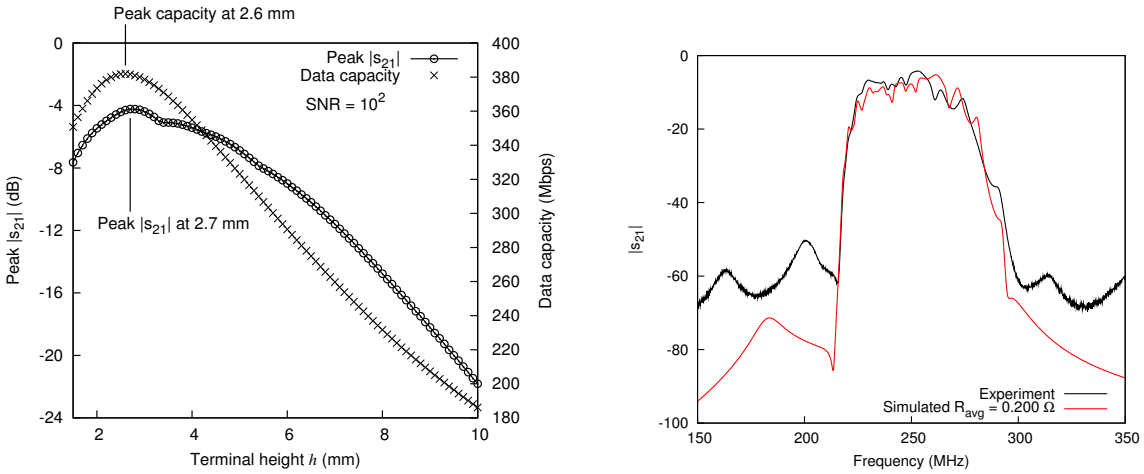


Figure 4.26 – A comparison between experimental and simulated peak $|s_{21}|$ against terminal height with the transmitter at (1,1) and the receiver at (6,6). Just as in Figure 4.19c, adjusting the simulated element resistance to 0.200 Ω gives a closer agreement with experiment.



(a) *(b)*

Figure 4.27 – A graph of experimentally obtained peak $|s_{21}|$ versus terminal height, h, with the transmitter at (1,1), and an SNR of 10^2, with the receiver at (6,6), (a). A comparison between the experimental and simulated transfer functions for $h = 2.7$ mm.

being positive, to negative. This makes the coupling to the terminal via the nearest-neighbours in-phase with the coupling of the terminal and the element underneath it.

Figure 4.27a shows that the peak $|s_{21}|$ and capacity were almost achieved at the same terminal height. Just as with the one-dimensional MI waveguide, one might expect that the edges of the MI passband, at the height at which peak $|s_{21}|$ was achieved, approximately corresponds to the frequencies of the split resonances of two-axially coupled elements at the same height. From Figure 4.29, the set of lines displaying the edges of the MI passband, and the set of lines

showing the split resonances of two axially-coupled elements

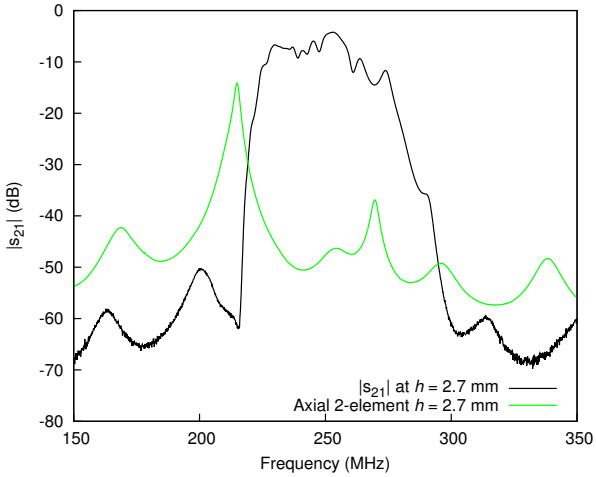


Figure 4.28 – A comparison between the transfer function for a 6 by 6 element array with the transmitter at (1,1), and the receiver at (6,6), with a terminal height, h, of 2.7 mm and the corresponding transfer function through two isolated axially-coupled loops with the same vertical separation.

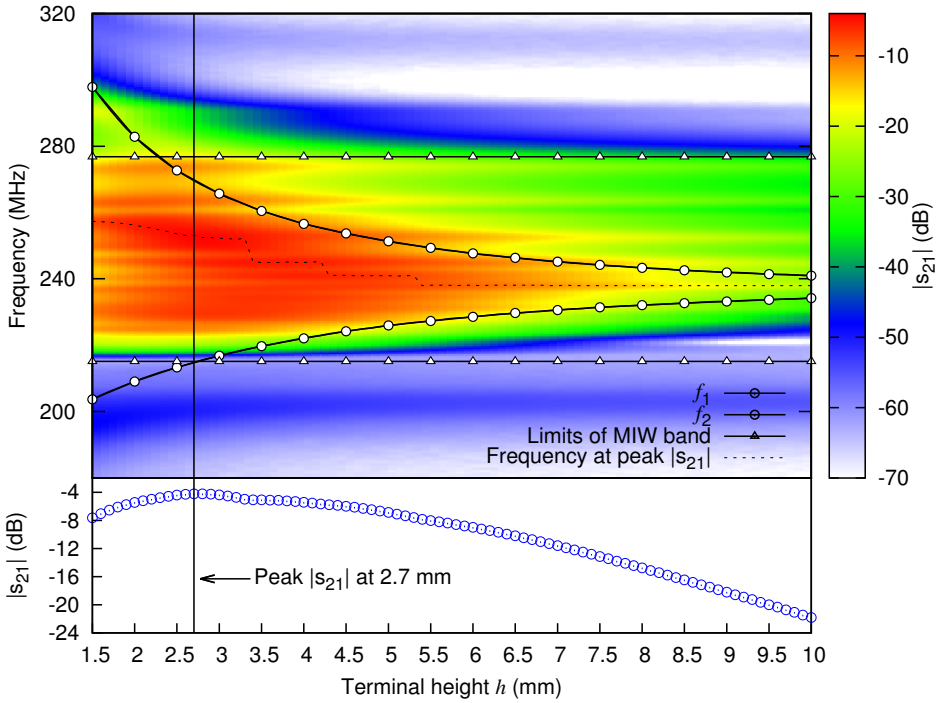


Figure 4.29 – The colour-map of experimentally obtained $|s_{21}|$ against frequency and terminal height, h, for the 2-D array where the transmitter is located at (1,1), and the receiver at (6,6). The dotted lines correspond to the split resonances that occur due to two resonators coupling axially as discussed in Section 2.2. The triangularly dotted lines indicated the upper and lower limits of the MI wave band for 2-D arrays. The dashed line corresponds to the frequency at which peak $|s_{21}|$ was achieved at a given h. The lower graph displays peak $|s_{21}|$ against terminal height.

As the receiver was held in a corner of the array, one would expect some symmetrical behaviour. Figure 4.30 gives an example of this symmetry. The minor differences are most likely caused by the variation of resonator characteristics, and the slight difference in κ due to the split in the loop.

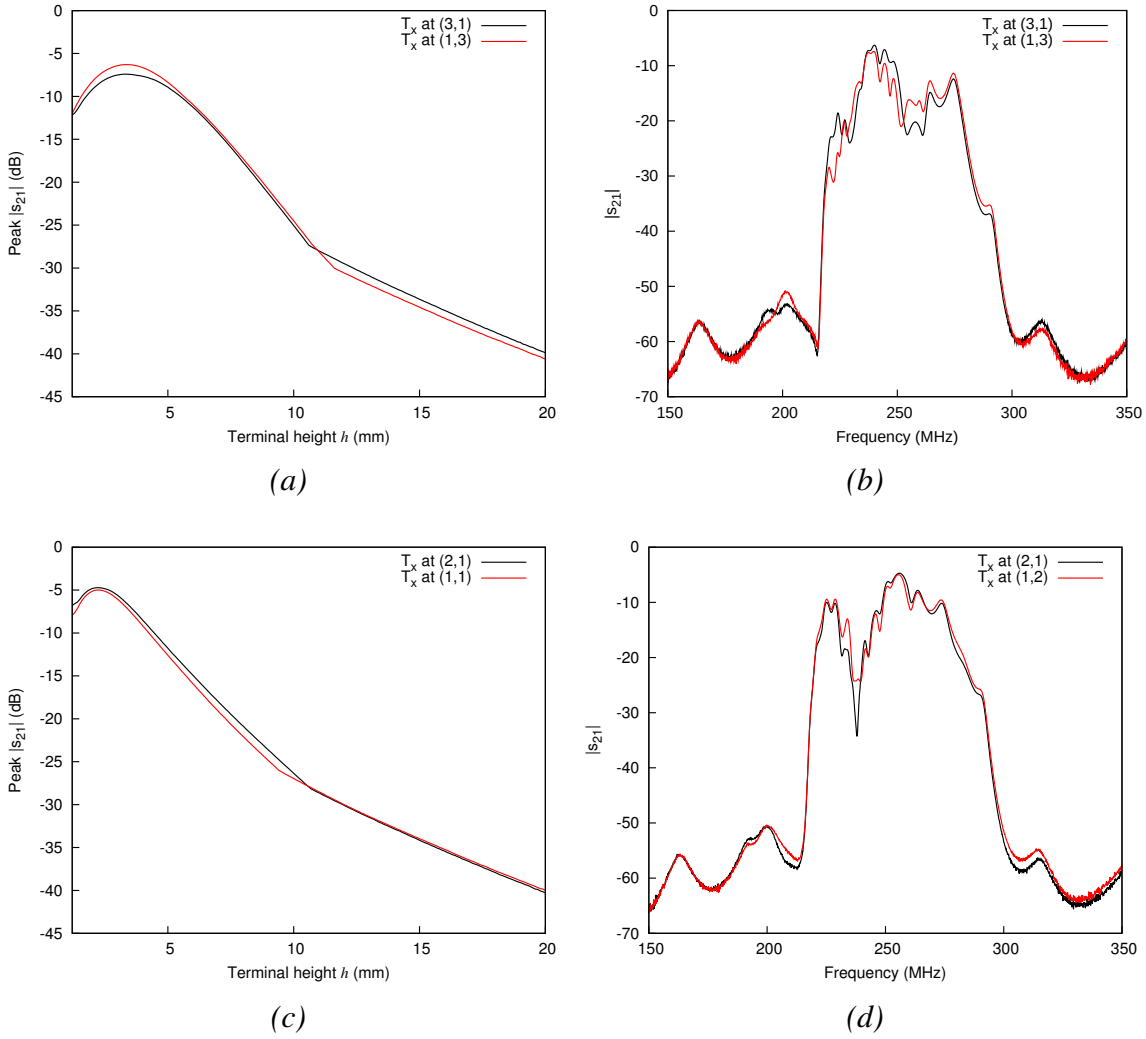


Figure 4.30 – Comparison between the experimental peak $|s_{21}|$ against terminal height curves when the transmitter is placed at (3,1), and (1,3), with the receiver at (6,6) (a), and their respective transfer functions at a h of 3.4 mm, (b). Comparison between the experimental peak $|s_{21}|$ against terminal height curves when the transmitter is placed at (2,1), and (1,2), with the receiver at (6,6) (c), and their respective transfer functions at a h of 2.2 mm, (d). The heights used were the heights at which the configurations attained their respective peak $|s_{21}|$.

Figure 4.31 contains tables which show the peak $|s_{21}|$, the terminal height h at which peak $|s_{21}|$ occurred, and the h at which peak capacity occurred for both experiment and simulation for the T_x-R_x configurations considered. Looking at Figure 4.31a and Figure 4.31b, counter-intuitively, the peak $|s_{21}|$ was achieved at the greatest T_x-R_x separation ((1,1)-(6,6)), and the

lowest with T_x at (6,5).

EXPERIMENT

Row	Peak $\lvert s_{21}\rvert$ (dB)	1	2	3
	6	-8.88	-8.76	-6.31
	5	-9.00	-6.32	-6.67
	4	-5.77	-6.29	-5.80
	3	-6.30	-6.88	-4.62
	2	-4.72	-6.18	-7.67
	1	-4.23	-4.99	-7.41
		Column		

(a)

SIMULATION

Row		1	2	3
	6	-7.75	-8.87	-9.37
	5	-8.02	-7.48	-6.88
	4	-6.29	-6.62	-7.64
	3	-7.52	-8.14	-6.63
	2	-6.87	-6.39	-7.52
	1	-6.03	-6.28	-7.20
		Column		

(b)

Row	h at peak $\lvert s_{21}\rvert$ (mm)	1	2	3
	6	3.7	2.7	2.5
	5	1.5	1.5	2.3
	4	2.5	2.5	1.8
	3	3.4	3.2	2.1
	2	2.2	1.9	3.4
	1	2.7	2.2	3.3
		Column		

(c)

Row		1	2	3
	6	2	2	2.3
	5	2	3	2.2
	4	2.4	2.1	2.4
	3	2.8	1.6	1.9
	2	2.1	1.8	1.6
	1	2.4	2.2	1.9
		Column		

(d)

Row	h at peak capacity (mm)	1	2	3
	6	2.6	2.5	2.3
	5	2.5	2.2	2.2
	4	2.3	2.4	2.2
	3	2.5	2.3	2.3
	2	2.4	2.4	2.4
	1	2.6	2.4	2.6
		Column		

(e)

Row		1	2	3
	6	1.8	1.8	1.8
	5	1.8	1.8	1.8
	4	1.8	1.8	1.8
	3	1.8	1.8	1.8
	2	1.8	1.8	1.8
	1	1.9	1.8	1.8
		Column		

(f)

Figure 4.31 – Tables comparing peak $\lvert s_{21}\rvert$ attained in experiment and simulation, (a) and (b) respectively, the heights at which peak $\lvert s_{21}\rvert$ was achieved for experiment and simulation, (c) and (d) respectively, the heights at which peak capacity was achieved for experiment and simulation, (e) and (f) respectively, when R_x remained at (6,6) and T_x was placed on each element within (1,1)–(6,3).

From Figure 4.31, it can be seen, especially from Figures 4.31c–4.31f, that in simulation the terminal heights at which peak $\lvert s_{21}\rvert$ was achieved are much lower than those obtained during experiment. It is believed that this translates to a weaker element-element coupling in the waveguide than through calculation as equation (2.33) suggests that a higher element-element coupling requires a higher terminal-waveguide coupling to achieve optimum coupling. The

findings in Table 4.4 supports this, as it was seen that the double integral method consistently over-estimated the various couplings compared to both those from experiment and FastHenry.

Interestingly, though more noticeable in simulation than experiment, there is more or less a fixed height at which peak capacity an be obtained. This height is 1.8 mm for simulation and 2.4 mm for experiment, it is believed, that similar to the one-dimensional case presented in Section 4.2.1.1, that a broader $|s_{21}|$ would have been responsible for the difference in h for when peak $|s_{21}|$ and peak capacity occurred.

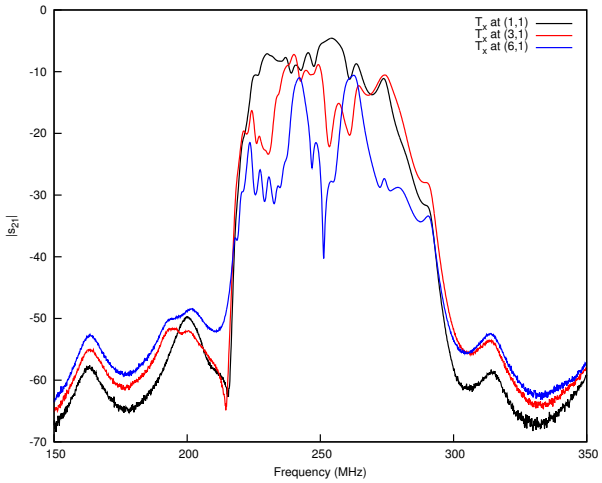


Figure 4.32 – The $|s_{21}|$ curves when T_x is at (1,1), (3,1), and (6,1), black, red, and blue lines respectively, all taken at a terminal height of 2.4 mm.

As mentioned in Section 2.3.1, it is expected that a two-dimensional MI waveguide should display an anisotropic bandwidth as shown in Figure 2.6. Thus one might expect the $|s_{21}|$ curves to narrow when T_x moves from being 45° diagonally to being inline with R_x. This can be seen to an extent in Figure 4.32, as the reduction in width between the T_x at (1,1) and (6,1) curves is evident, however response broadens somewhat between (1,1) and (3,1). It is possible that as a 6-by-6 array is a small environment where the attentuation is not sufficient to absorb reflections, that these reflections lead to the effects seen in Figure 4.32.

4.2.1.4 MOBILE RECEIVER

In this set of experiments, the transmitter, T_x, remained above (1,1) and the receiver, R_x, was moved. The considered T_x positions are shown in Figure 4.33. The terminals were only brought

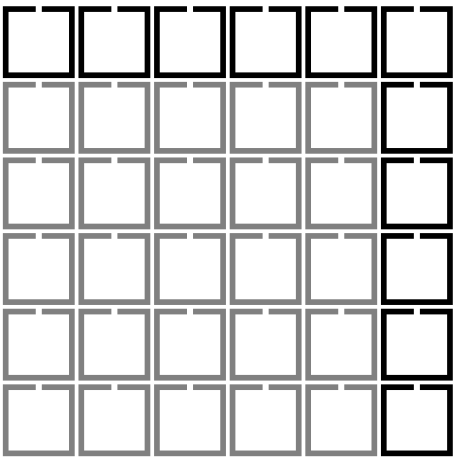
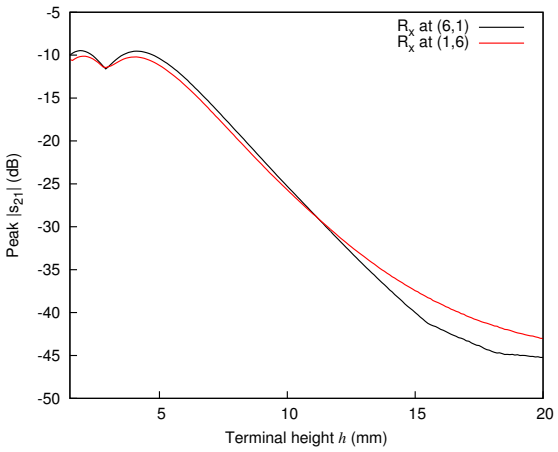


Figure 4.33 – R_x positions considered in solid black. T_x remained at (1,1) throughout.

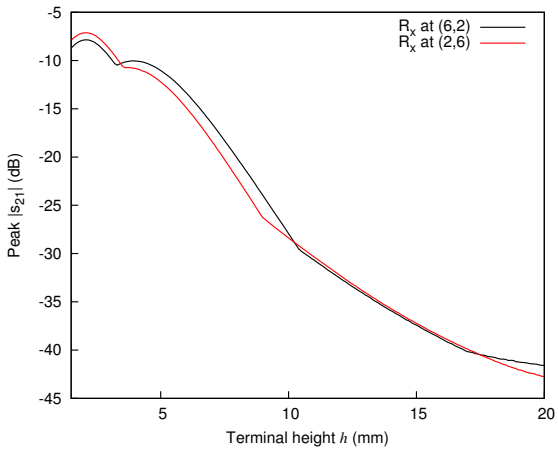
to 1.5 mm above the surface of the MI waveguide as it was found that previously, it was possible for the terminals to come in contact with it when h was close to 1 mm. This was reckoned to have been due to the construction of the terminals; looking at Figure 4.16c, it was thought that the two wires that protrude from the resonator's surface came into contact with the resonators in the waveguide. The wires were carefully filed down, though given the small scale of the protrusion, and the somewhat awkward position for filing, it was not possible to eliminate entirely.

As T_x is to stay at (1,1), a symmetry around the diagonal from (1,1) to (6,6) is expected, just as in Section 4.2.1.3. Figure 4.34 compares the peak $|s_{21}|$ curves of equivalent terminal configurations.

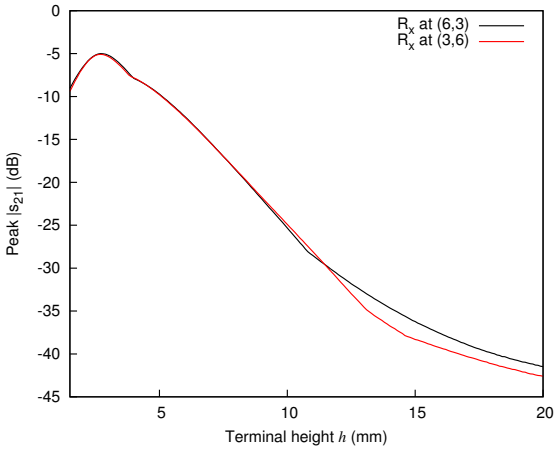
Of the graphs of peak $|s_{21}|$ versus h shown in Figure 4.34, Figures 4.34a–c have noticeable kinks before $h = 5$ mm, and Figure 4.34d has only a slight kink in the curve. Curiously, this kink appears to occur at slightly lower and lower heights as R_x gets further and further away from T_x. Figures 4.36a–d reveals what features in the $|s_{21}|$ curves causes this; in Figure 4.36a, it's clear that there are two frequency peaks, at approximately 260 MHz and 245 Mhz, that cause the first and second local maxima respectively in the peak $|s_{21}|$ versus h curve. Another interesting feature is that, by grouping Figures 4.36a–c, and Figures 4.36d–f together, one can see that for the former group, the majority of transfer appears to be limited to frequencies above 240 MHz, but for the latter group, this band appears to merge with another, extending it to 220 MHz. It is believed that this is caused by the bandwidth anisotropy mentioned in Section 2.3.1, whereby



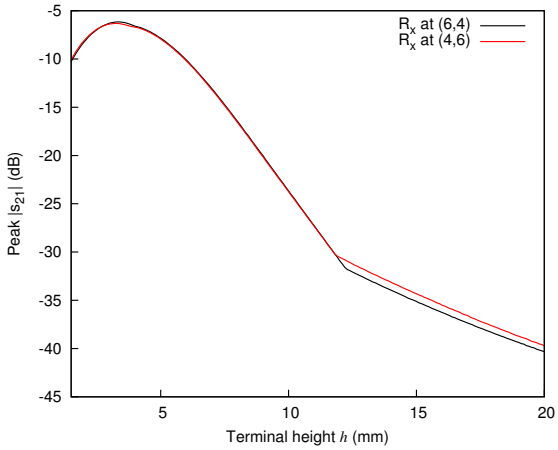
(a)



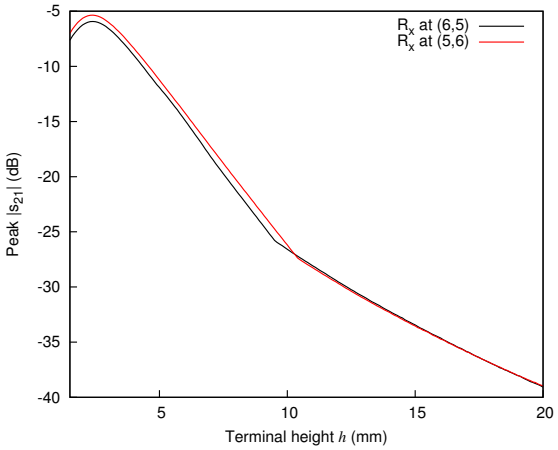
(b)



(c)



(d)



(e)

Figure 4.34 – Comparison of peak $|s_{21}|$ versus terminal height h for equivalent T_x-R_x placements. T_x at (1,6) and (6,1), (a), (2,6) and (6,2), (b), (3,6) and (6,3), (c), (4,6) and (6,4), (d), (5,6) and (6,5), (e), with R_x at (6,6).

there is a certain amount of bandwidth available to every angle, but more available when the angle to either the x or y direction is 45°. Of course, one can also see a decent degree of transmission in this "extra" bandwidth region, this is believed to be due to reflections in the array as the waveguide's attenuation is not sufficient to diminish the reflections.

Figure 4.35 provides a summary of the terminal height at which peak s_{21} and capacity is achieved in both experiment and simulation. Just as in Section 4.2.1.3, the heights at which peak capacity are approximately the same for all R_x positions and occur at the same heights as before, 1.8 mm for simulation and 2.4 mm for experiment.

4.2.1.5 MOBILE TRANSMITTER AND RECEIVER COMPARISONS

Evidently, some of the T_x-R_x configurations considered in Sections 4.2.1.3 and 4.2.1.4 are similar to each other in terms of layout, especially in the angle of the terminals to each other. The particular configurations considered have equivalent T_x-R_x angles, and the peak $|s_{21}|$ versus terminal height, h, comparisons are shown in Figure 4.37 and the $|s_{21}|$ versus frequency at an h of 2.4 mm. This particular height was chosen as, in Sections 4.2.1.3 and 4.2.1.4 this was found to be the height at which maximum capacity would occur for most T_x-R_x configurations.

In Figure 4.37, it can be seen that there are similarities between the configurations considered in Section 4.2.1.3 and 4.2.1.4, however in Figure 4.37c, it can be seen that the result from Section 4.2.1.4 displays a noticeable kink compared to the result from Section 4.2.1.3. It is possible that due to the fact that as T_x was held in the same place for all experiments in Section 4.2.1.4 that similar standing wave patterns were set up for each of the configurations that were considered. For the experiments in Section 4.2.1.3, R_x was fixed, and so as T_x was moved into various positions, it would set up differing wave patterns in the MI waveguide. Thus, for the former situation, R_x would be in different positions of the same pattern, but for the latter, the opposite would be true.

Figure 4.38 shows the similarities between equivalent T_x-R_x angle configurations, this implies that the wave patterns in the MI waveguide for equivalent T_x-R_x angle configurations are similar, despite how h affects the terminal coupling to the MI waveguide.

EXPERIMENT

1.9	2.1	2.7	3.4	2.4	2.7
					2.4
					3.2
					2.7
					2.1
					2.1

Terminal height h when peak s_{21} is achieved (mm)

(a)

SIMULATION

2.1	2.1	2.5	1.7	1.8	2.4
					1.8
					1.7
					2.4
					2.1
					2.0

(b)

−9.47	−7.86	−5.00	−6.16	−5.93	−4.01
					−5.36
					−6.39
					−5.81
					−7.13
					−10.12

Peak $|s_{21}|$ (dB)

(c)

−8.19	−7.44	−7.36	−7.77	−5.90	−6.03
					−5.80
					−6.88
					−7.42
					−7.28
					−8.24

(d)

2.4	2.4	2.4	2.4	2.4	2.5
					2.4
					2.4
					2.4
					2.4
					2.4

Terminal height h when peak capacity is achieved (mm)

(e)

1.9	1.8	1.8	1.8	1.8	1.9
					1.8
					1.8
					1.8
					1.8
					1.8

(f)

Figure 4.35 – Figures in the left column represent values from experiments, and those on the right from simulation. The first row, (a) and (b) shows the terminal height, h, at peak s_{21} in mm. The second row, (c) and (d), shows the peak s_{21} in dB. The h at which peak capacity is achieved in experiment and simulation, (e) and (f).

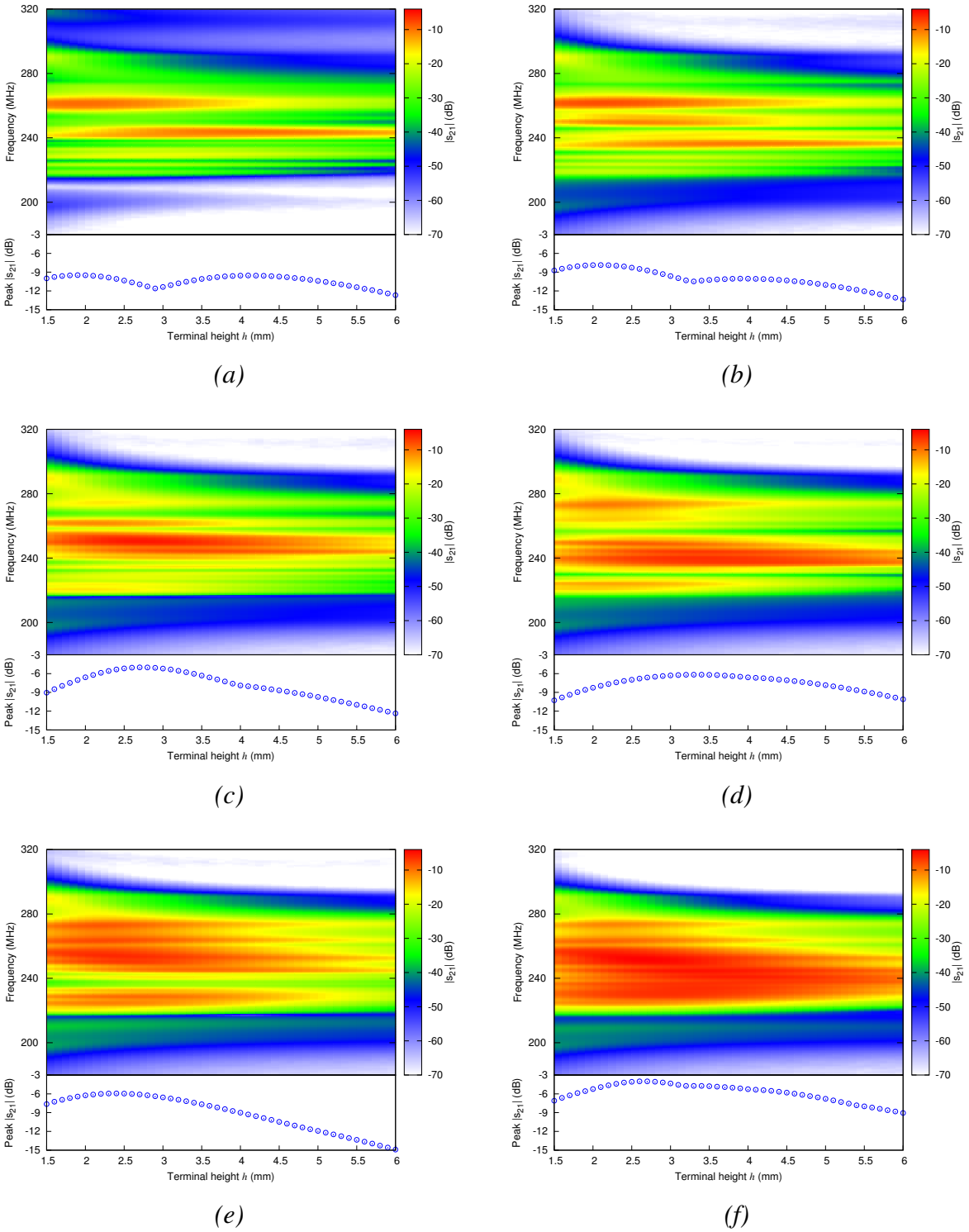
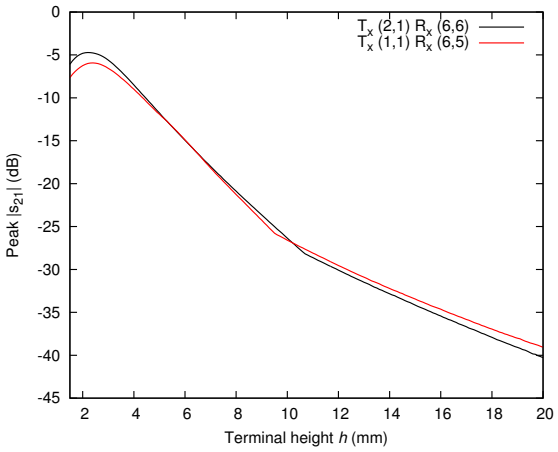
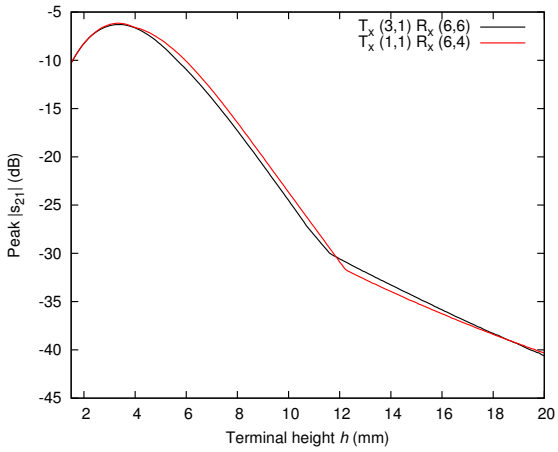


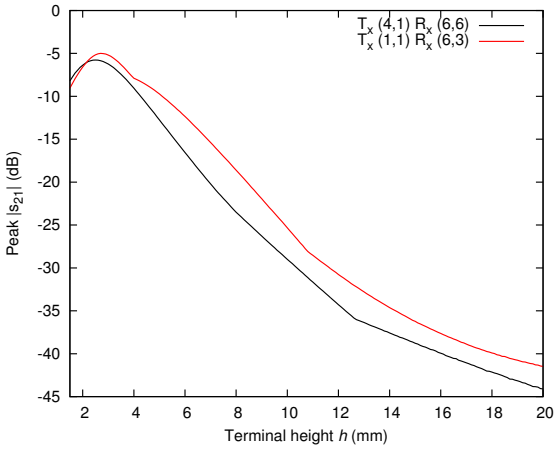
Figure 4.36 – Colour-maps of experimentally obtained $|s_{21}|$ against frequency and accompanying peak $|s_{21}|$ versus terminal height, h, graphs with the transmitter T_x fixed at (1,1) and the receiver R_x at (6,1) (a), (6,2) (b), (6,3) (c), (6,4) (d), (6,5) (e), (6,6) (f), and h varying between 1.5–6 mm.



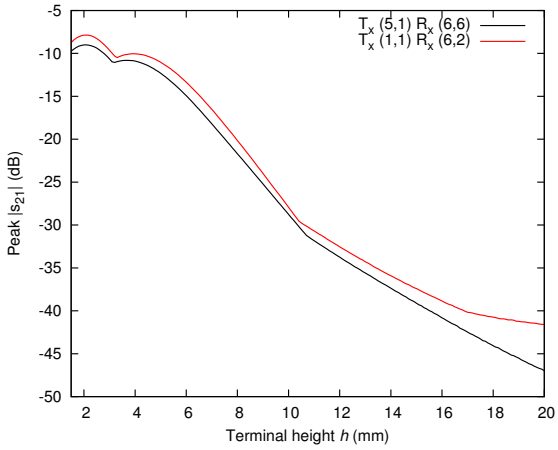
(a)



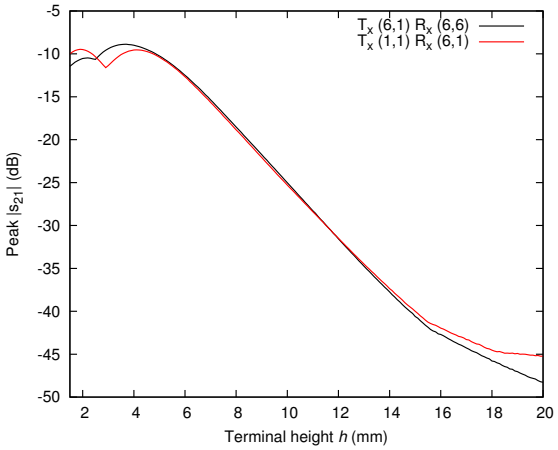
(b)



(c)

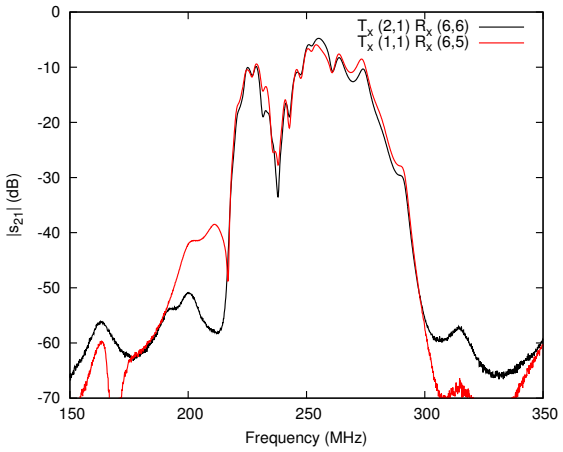


(d)

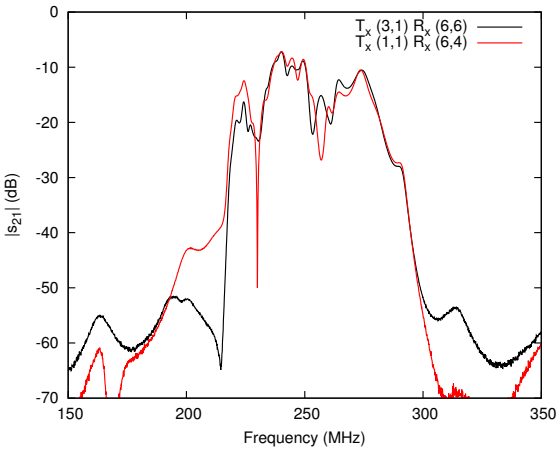


(e)

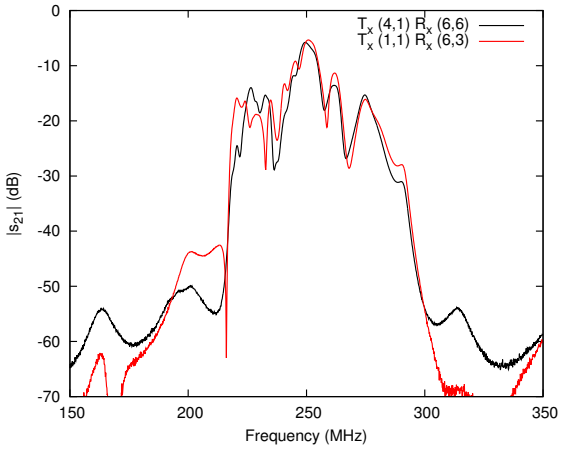
Figure 4.37 – Comparisons of peak $|s_{21}|$ versus terminal height h, for various configurations of equivalent T_x-R_x angle. Results from mobile transmitter in black and results from mobile receiver in red.



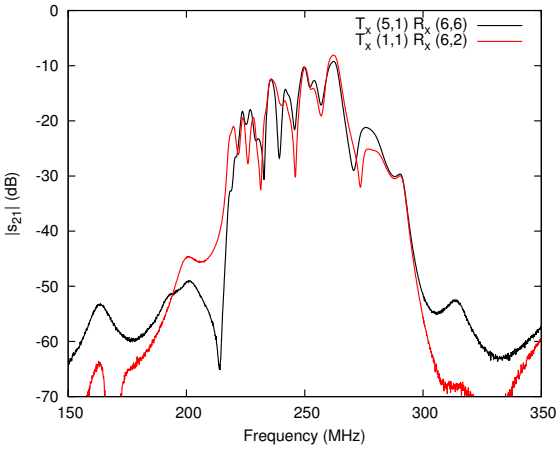
(a)



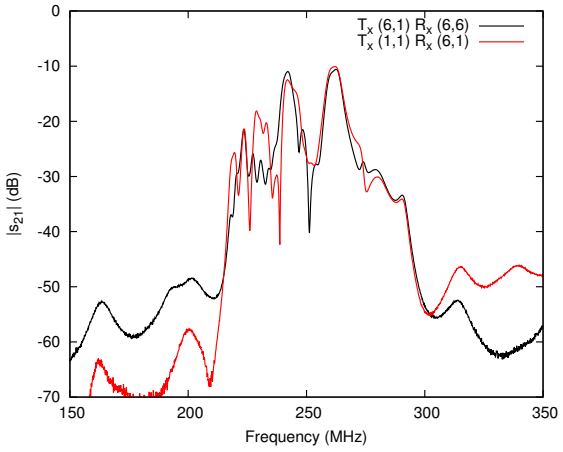
(b)



(c)



(d)



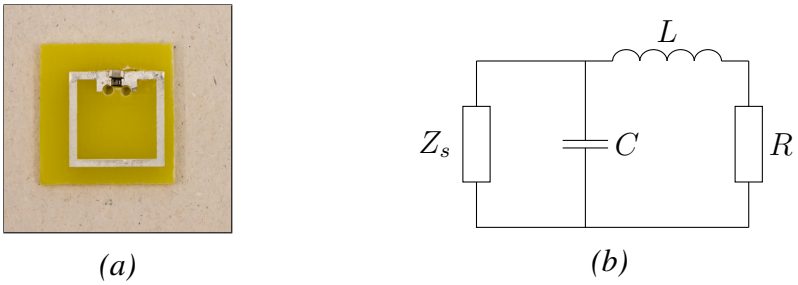
(e)

Figure 4.38 – Comparisons of $|s_{21}|$ response versus frequency at a terminal height, h, of 2.4 mm, for various configurations of equivalent T_x-R_x angle.

4.2.2 TERMINAL BLOCKING

In the previous section and previous work [65], two-terminal one- and two-dimensional MI wave data communcation systems have been investigated, however as the aim is to develop a system with more terminals, it is necessary to ascertain the impact of introducing further terminals. This was done by the addition of a third "blocking" terminal, so-called as it was expected to "block" the communciations between two terminals to some degree.

The blocking terminal is akin to a resonant probe, but without a cable between the resonator and the load. As such, it electrically resembles the resonant probe and its ciruit equivalent can be described by Figure 4.39. The terminal was made by soldering a 49.9 Ω surface mount resistor in parallel to a resonator's capacitor.



(a) (b)

Figure 4.39 – Photograph of the blocking terminal implementation (a), the circuit diagram for a blocking terminal (b).

The blocking terminal was attached to the stage mover (Figure 4.13) using electrical insulation tape. Its height above the waveguide was then set, and the terminal was scanned from one end to another in 0.1 mm increments, starting and ending centred above the first and last element respectively.

4.2.2.1 ONE-DIMENSIONAL

This section aims to make an assessment of the effect of a third "blocking" terminal on a two-terminal one-dimensional MI wave data system. In such a system, the lowest capacity between the two terminals, when limited to on-element positions, would be when the terminals are at

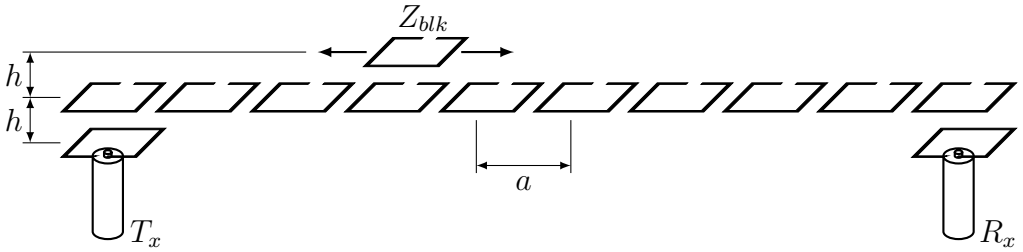


Figure 4.40 – A 10-element strip with a period of a, a blocking terminal impedance Z_{blk}, a transmit and receive terminal, T_x and R_x respectively, with terminals above the strip by height h (capacitors omitted).

either end of the waveguide [65]. As such, it was decided that this would be the arrangement to be tested. Figure 4.40 illustrates the experimental layout.

Two resonant probes were positioned under the strip, centred over the elements at opposite ends of the MI waveguide. Meanwhile, a blocking terminal scanned over the top, using the stage mover, starting centred over the first element and moving in 0.5 mm steps until being centred over the last element. T_x and R_x were connected to port 1 and 2 respectively of a HP 8753ES VNA, which was used to measure the complex s_{21} at 1601 between 210–280 MHz. The terminal height, h, was 4.3 mm, yielding the optimum coupling found in Section 4.2.1.1. All capacities were calculated assuming an SNR of 10^2 and a 37 MHz bandwidth centred around a frequency of 239.46 MHz. The SNR was chosen as it was believed it would provide a suitable magnitude for the purposes of calculating the capacity for comparison between scenarios and studying the waveguide's behaviour. It should be noted that, by observing that the mid-band is over 20 dB higher than the outer region in Figure 4.22, higher SNRs are certainly achievable. The bandwidth chosen marginally exceeds the MI bandwidth given by (2.16), in Section 2.3.

The simulations assumed the resonator characteristics obtained though characterization. Variation in quality factor was preserved when adjusting the values of R. This was achieved by equating the variations in Q to variations in R via equation (2.2). However, the values of mutual inductance between elements were still calculated using (2.5), with the effective length of one side of a resonator as 8.856 mm as determined by the method discussed in Section 4.2 giving a coupling of -0.149. The coupling of the terminals to the elements in the waveguide was done using (2.5) also, with T_x and R_x coupling to the first and second nearest neighbours, and the blocking terminal coupling to all the elements in the waveguide.

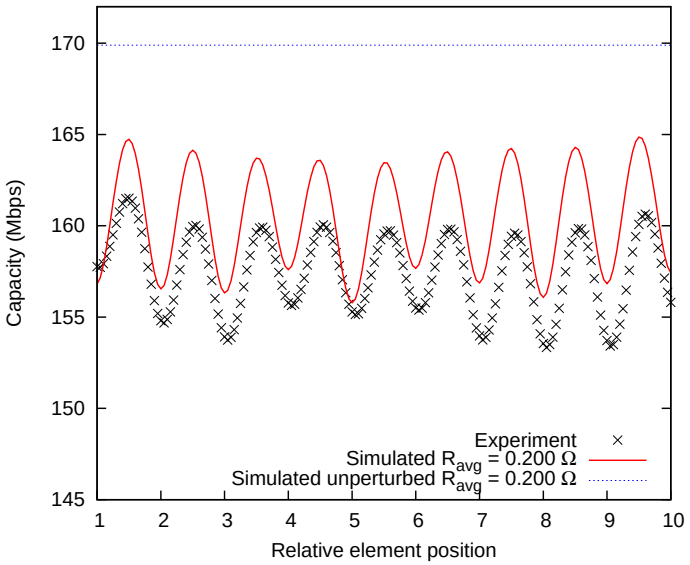


Figure 4.41 – A comparison between the experiment and simulated throughput of a 10-element strip. The transmit and receive terminals are placed at opposite ends of the strip whilst a blocking terminal is scanned from one end to the other. The terminal height, h, is 4.3 mm.

Figure 4.41 displays the effect of a blocking terminal on the strip throughput. The agreement between simulation and experiment is good; the discrepancy being caused by the higher value of κ in the simulation. This lead to a marginally wider transfer function, and thus a higher capacity. There is an oscillatory nature to the capacity as the blocking terminal scans along the strip. This is due to the fact that the terminal couples to the waveguide more strongly when it is directly above an element. Thus when the blocking terminal's coupling to the waveguide is weakest, the strip observes its highest throughput. Figure 4.42 compares the $|s_{21}|$ of the unperturbed case with the $|s_{21}|$ in the presence of a blocking terminal above the first element and halfway between the first and second element.

It can be seen that the average strip throughput, with a blocking terminal, is only $\approx$13 Mbps or $\approx$8% less than the unperturbed case. In addition, there is only a variation of $\approx$5 Mbps in the strip throughput when the blocking terminal is scanned along the strip. This means that a one-dimensional structure could be able to support multiple terminals without a significant penalty to its performance.

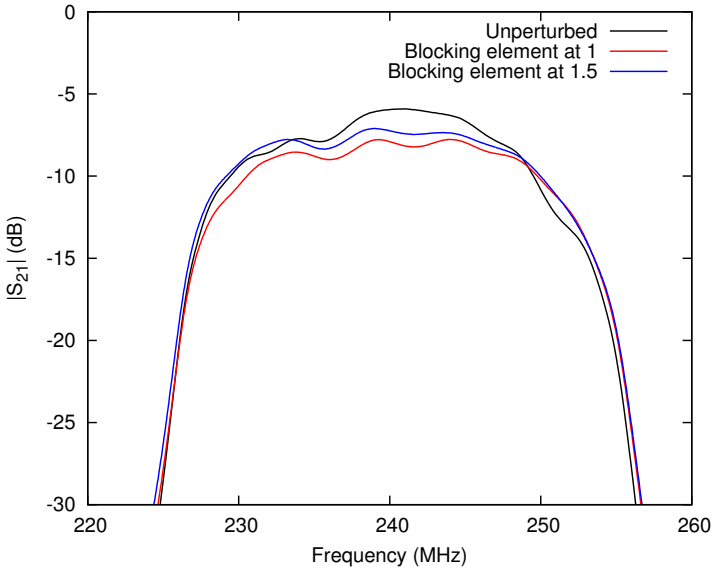


Figure 4.42 – Comparison of $|s_{21}|$ vs frequency for a 10-element one-dimensional MI waveguide with terminals at h = 4.3 mm (black), and with a blocking terminal present at h = 4.3 mm over the first (red) and midway between the first and second element (blue).

4.2.2.2 TWO-DIMENSIONAL

In this section, the performance of the 6-by-6 two-dimensional MI waveguide, as shown and characterized by Section 4.2, is assessed by seeing the effect of a third "blocking" terminal on the data capacity between two terminals. Figure 4.43 illustrates the experimental layout.

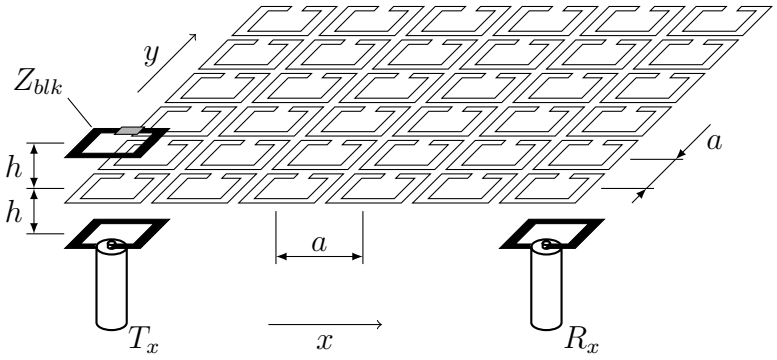


Figure 4.43 – Diagram of system layout. The position of the two terminals, T_x, R_x, are fixed during an experiment whilst the "blocking" terminal, Z_{blk}, is free to scan in the x and y directions above the 6-by-6, square-element, array. All terminals are at a height, h, above (Z_{blk}) or below (T_x,R_x) the array. The array's period, a is the same in both x and y directions.

Sections 4.2.1.3 and 4.2.1.4 had shown that the highest and lowest transmission of all T_x-R_x configurations tested were when the terminals were at opposite corners and opposite ends of the same edge of the waveguide respectively. Thus it was decided that two configurations would

be tested, one where T_x and R_x were at opposite corners of the waveguide, and one where they were at opposite ends of the same edge.

T_x and R_x were connected to port 1 and 2 respectively of a HP 8753ES VNA, which was used to measure the complex s_{21} at 1601 points between 150–350 MHz.

The terminal height h was chosen to be 2.4 mm, as this was the h at which the majority of configurations attained maximum experimentally derived capacity. An SNR of 10^2 was assumed, the bandwidth taken was 215–300 MHz. This is larger than in the previous sections simply to ensure the entire MI passband was included, areas outside of the passband are sufficiently low in magnitude that they will not affect the capacity determined using this bandwidth. The transmitter and receiver were assumed to be below the plane of the array, whilst the blocking terminal was free to move over the top. The adjusted R of 0.200 Ω was used as this has resulted in a better correspondence with experiments in previous sections.

Figure 4.44 shows the comparison between experiment, Figures 4.44a and 4.44c, and simulation, Figures 4.44b and 4.44d, for the configurations considered. There is good agreement between experiment and simulation with the simulated data-rates for the unperturbed capacity being within 6% of the experimental values. The spread of relative capacity when terminals are in opposite corners (Figures 4.44a and 4.44b) and at the ends of a common edge (Figures 4.44c and 4.44d) of the array are in good agreement, with the difference in the amount of spread being approximately negligible and 4% respectively. The spatial variation in data capacity for both experiment and simulation is also very similar.

The difference in capacity between the two different configurations highlights the anisotropic MI bandwidth as described in Section 2.3.1. In the case where T_x and R_x are in opposite corners (Figures 4.44a and 4.44b), the reduction in capacity is greatest when the blocking terminal is directly above any element. This is due to the fact that the blocking terminal is most strongly coupled and absorbing the most power at these points.

For all configurations, the blocking terminal appears to have a minimal effect on the data transfer between T_x and R_x. This is true even when the blocking terminal is on the direct signal

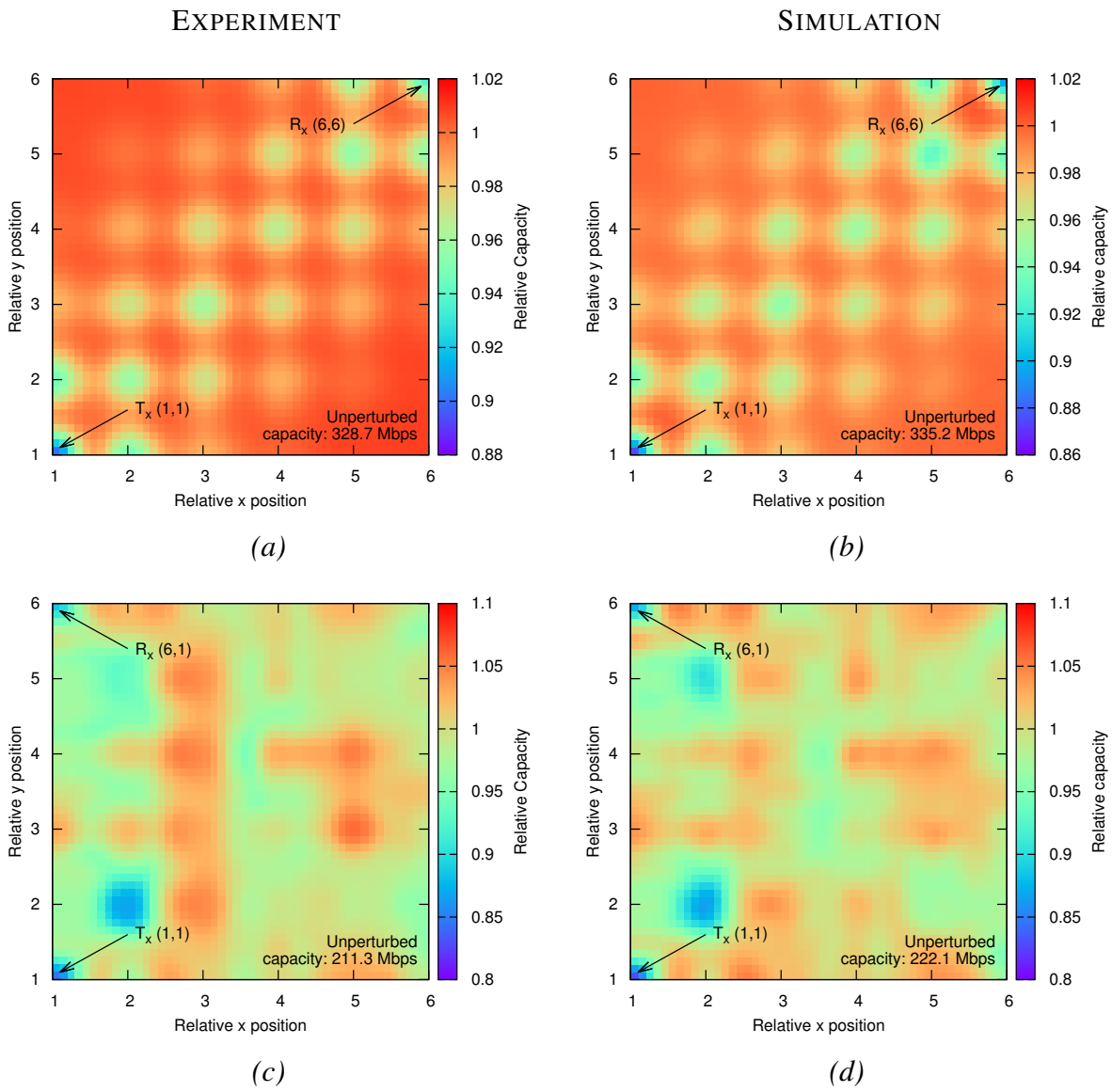
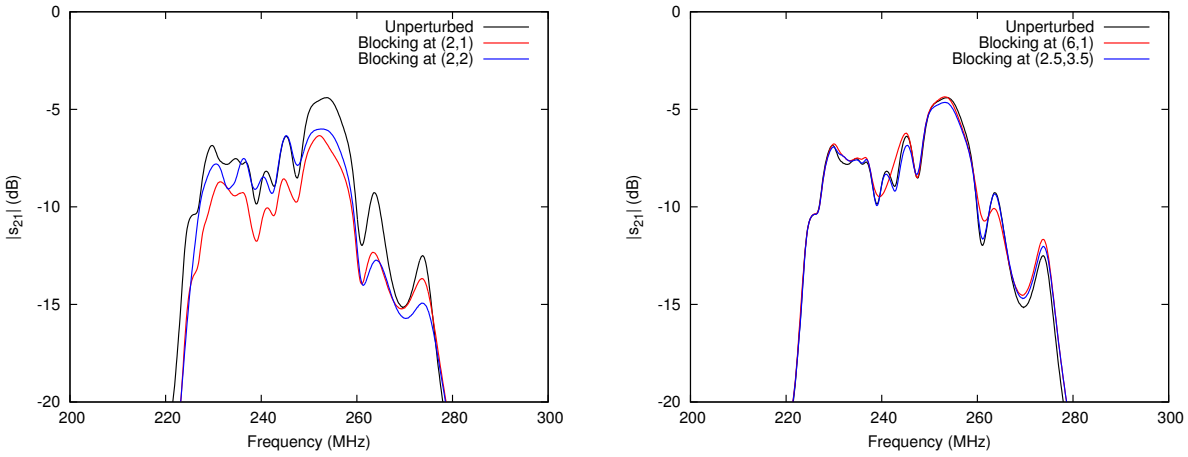


Figure 4.44 – Colour-maps of data capacity, with an assumed SNR of 100, between two terminals with a terminal height of 2.4 mm, T_x and R_x, whilst a blocking terminal was scanned above the array in 1 mm steps in the x and y directions relative to the case where there was no blocking terminal, termed as the "unperturbed capacity". In (a) and (b), T_x and R_x were placed at (1,1) and (6,6) respectively; in (c) and (d), T_x and R_x were placed at (1,1) and (6,1) respectively. (a) and (c) show the experimentally derived data capacities, whilst (b) and (d) show simulated data capacities. The position of the blocking terminal is displayed as being relative to element positions within the array.

path between T_x and R_x, implying that the signal is distributed over multiple paths and/or that reflections contribute strongly to data capacity.

Interestingly, on-element positions that are adjacent to T_x or R_x seem to affect capacity negatively also. When T_x and R_x are at opposite ends of the waveguide, aside from the obvious

effect the blocking terminal has on the direct signal path, it also affects transmission when on the off-diagonal as Figure 4.45 shows. Especially when the blocking terminal is on the adjacent element in the x or y direction to T_x (Figure 4.45a). It would seem that even though the signal path is evidently diagonal, it's possible that this signal is in fact carried in the vertical and horizontal directions. This would make some sense as the coupling between elements purely in the x and y directions is much higher than the coupling between diagonally adjacent elements. Figure 4.45b provides the $|s_{21}|$ of two positions whereby the capacity was enhanced by the presence of a blocking terminal. As the increase is less than 2% there is a minimal difference between the $|s_{21}|$ curves.



(a) *(b)*

Figure 4.45 – The $|s_{21}|$ response when T_x and R_x are at (1,1) and (6,6) respectively without the presence of a blocking terminal (black), with a blocking terminal at (2,1) and (2,2) (a), and with a blocking terminal at (6,1) and (2.5,3.5) (b).

When T_x and R_x share corners of a common edge (Figures 4.44c and 4.44d), the blocking terminal has a greater, yet still not severe, effect. Interestingly, the capacity is again barely affected when the blocking terminal is on the direct signal path. Unexpectedly, capacity is most affected when the blocking terminal is on the 45° diagonals from T_x or R_x. Though there is a strip on the third column, lasting until just over half-way to the fourth column, where the data capacity has increased due to the blocking terminal's position. This effect suggests that the main signal path, even for purely horizontal or vertical configurations, is via a 45° diagonal and that the blocking terminal may even enhance the capacity when adjacent to the signal path. When the blocking terminal was placed at (3,3) or (4,3) in Figures 4.44c and 4.44d, it may

have reflected the signal from T_x towards R_x. This suggests that a blocking terminal may help data transfer between two terminals when they are not at 45° to each other by supplying an alternate path with more bandwidth. Curiously, there is also a patch futher away from the line of transmission between the (3,5) and (4,5) positions that appears to increase the capacity the most, even when compared to the large patch in the third column.

Again, due to the anisotropic bandwidth and referring to the dispersion diagram for a negatively coupled two-dimensional MI waveguide in Figure 2.5b, one would expect that should the blocking terminal be reflecting any signals at the locations where capacity was increased between T_x and R_x, that it would boost the response in the lower frequencies as this is the "extra" bandwidth that would be afforded on the diagonal. Figure 4.46 compares the unperturbed case to two different capacity-enhancing blocking terminal placements.

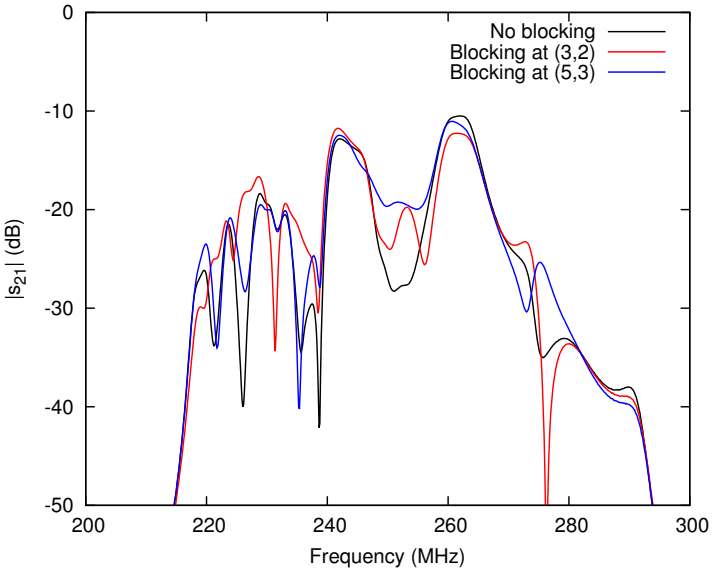


Figure 4.46 – The $|s_{21}|$ response when T_x and R_x are at (1,1) and (6,1) respectively without the presence of a blocking terminal (black), with a blocking terminal at (3,2) (red), and with a blocking terminal at (5,3) (blue).

Curiously, frequencies below 240 MHz see little improvement, however the trough of the unperturbed case between 240–260 MHz sees an appreciable increase in transmission. This implies that actually, the blocking terminal is most likely removing the destructive interefence of certain frequencies.

Interestingly, when T_x and R_x share corners of a common edge, it would seem that capacity is reduced the most, after being placed directly upon T_x or R_x, when on the elements

diagonally adjacent to T_x or R_x. Figure 4.47 shows that this is due to absorbtion of frequencies below 240 MHz by the blocking terminal.

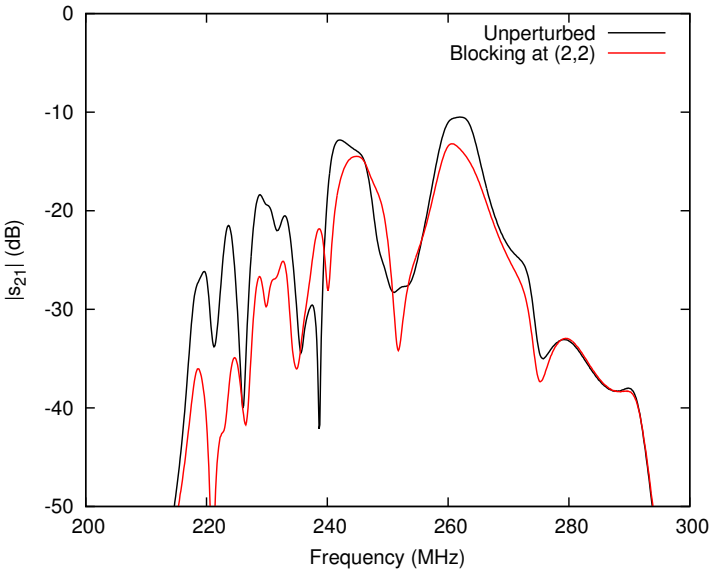


Figure 4.47 – The $|s_{21}|$ response when T_x and R_x are at (1,1) and (6,1) repsectively without the preseence of a blocking terminal (black), with a blocking terminal at (2,2) (red).

The capacity was expected to scale appropriately with the change to two dimensions due to the expected doubling of bandwidth. Looking at equation (2.30), it can be seen that if the bandwidth doubles, the capacity should also double if the transfer function has the same magnitude. This would equate to an unperturbed capacity of 340 Mbps. However, this is not achieved; it may be that the two-dimensional transfer functions are not sufficiently broad and smooth, or that there are some reflections that reduce the transfer functions.

4.3 BANDWIDTH EXPANSION

In this section, knowledge from Section 2.4 is used to create two methods for increasing the given bandwidth of a MI waveguide, one for increasing the bandwidth of a one-dimensional MI waveguide, and the other for increasing the bandwidth of a two-dimensional MI waveguide.

4.3.1 PSEUDO ONE-DIMENSIONAL STRUCTURE

In Section 4.2.2.2, it was seen that a blocking terminal barely affected the transmission between two terminals in opposite corners of the array if it was not in the direct signal path. The transmission was affected on the diagonal and the off-diagonals. Thus, to improve the performance of a one-dimensional MI waveguide, one could envisage a structure that is like a two-dimensional MI waveguide, but is only composed of the diagonal, and the first off-diagonals.

A possible explanation for this behaviour is shown in Figure 4.48, where although the principal direction of travel is diagonal the signal itself travels along the x and y directions in a zigzag fashion as these directions have the strongest coupling.

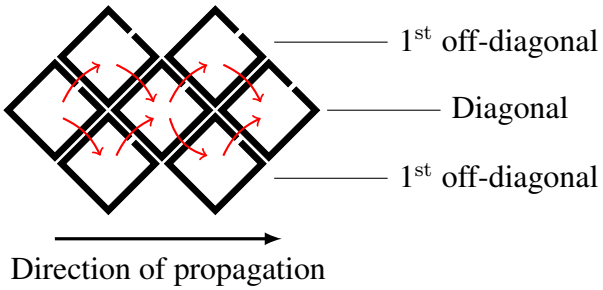


Figure 4.48 – The strongest couplings in the 2-D array are to the elements adjacent to the sides, it could be that the signals reinforce each other on the diagonal due to this. The diagonal and first off-diagonals are labelled.

One could therefore envision a waveguide that is comprised of the diagonal, and a number of off-diagonals of a two-dimensional MI waveguide, but only used for "one-dimensional" data transfer. It was decided that two versions of this waveguide would be made to ascertain the behaviour of such a waveguide. One could reasonably expect a channel of a bandwidth up to that of a two-dimensional MI waveguide, but in a pseudo one-dimensional structure.

The devices made are shown in Figure 4.49, and they are both comprised of the square elements described in Figure 4.7. The spacing between elements was 10 mm in the x and y directions, as in Section 4.2, leading to an inter-element coupling, κ, of -0.130, a κ of -0.150 was used for simulation. Figure 4.49a shows a "tucked" 10-element pseudo one-dimensional structure that is similar to a 10-by-10 two-dimensional MI waveguide, but with only the leading

diagonal and first off-diagonals. Figure 4.49b shows a "flared" structure similar to Figure 4.49a, but including extra elements adjacent to the first and last elements. It was believed that these extra elements might improve transmission compared to the tucked variation.

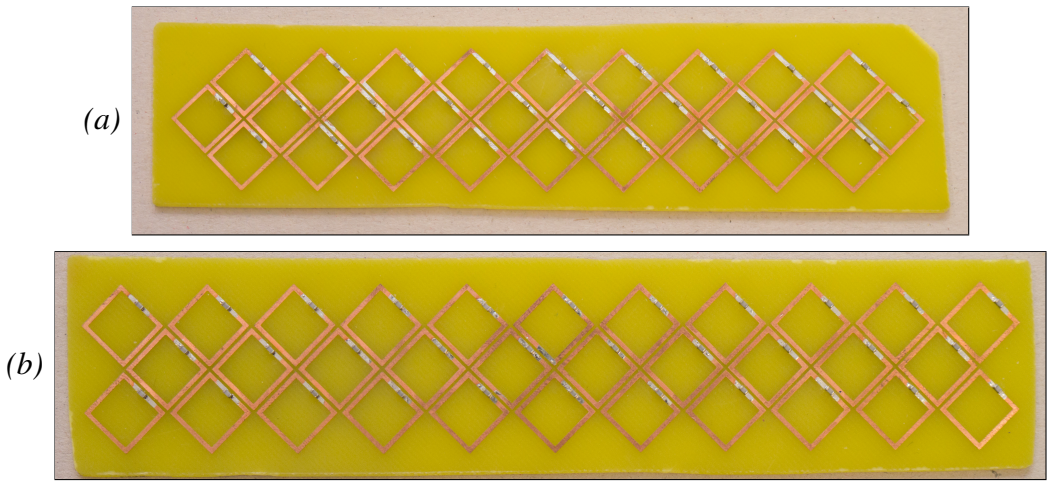


Figure 4.49 – Photograph of pseudo one-dimensional structures, "tucked" variation (a), and "flared" variation (b).

The pseudo one-dimensional structures were also simulated using the impedance matrix method as outlined in Section 3.1, however a new generalized impedance matrix form had to be found. Consider the structure in Figure 4.48, that is composed of three elements on its leading diagonal, and the first off-diagonals, its impedance matrix would be given by (4.8)

$$\begin{pmatrix} Z & j\omega M & j\omega M & j\omega M_1 & 0 & 0 & 0 \\ j\omega M & Z_{aux1} & j\omega M_1 & j\omega M & j\omega M_1 & 0 & 0 \\ j\omega M & j\omega M_1 & Z_{aux2} & j\omega M & 0 & j\omega M_1 & 0 \\ j\omega M_1 & j\omega M & j\omega M & Z & j\omega M & j\omega M & j\omega M_1 \\ 0 & j\omega M_1 & 0 & j\omega M & Z_{aux1} & j\omega M_1 & j\omega M \\ 0 & 0 & j\omega M_1 & j\omega M & j\omega M_1 & Z_{aux2} & j\omega M \\ 0 & 0 & 0 & j\omega M_1 & j\omega M & j\omega M & Z \end{pmatrix}. \tag{4.8}$$

Whilst all the elements have the same impedance, those with impedance Z are those on the leading diagonal, and Z_{aux1} and Z_{aux2} belong to the off-diagonals. This is not as simple as generating the impedance matrix for a two-dimensional waveguide but one can see that a form can be obtained and that the impedance matrix for the "tucked" pseudo one-dimensional structure of Figure 4.48 is made of the sub-matrices outlined in 4.8 but the solid and dashed

rectangles. The sub-matrix described by the solid rectangle is actually the impedance matrix of a 2-by-2 element section, and the sub-matrix described by the dashed rectangle is the coupling between the two solid rectangle sections. There is overlap between the two solid rectangles as they share an element in the centre.

If such a structure has n elements on its leading diagonal, it would have $3n-2$ elements in total as the off diagonals each contain $n-1$ elements. The impedance matrix of such a structure with n elements on its leading diagonal would then be made in simulation by first creating a $(3n-2,3n-2)$ matrix of zeroes filled in the following manner: the solid rectangles would be placed between the coordinates $(3t-2,3t-2)$ to $(3t+1,3t+1)$, where t takes integer values between 1 and $n-1$; the dashed rectangles would be placed between the coordinates $(3u-1,3u+2)$ to $(3u,3u+3)$ for the boxes above the leading diagonal, and between $(3u,3u+3)$ to $(3u-1,3u+2)$ for the boxes below the leading diagonal, where u takes integer values between 1 and $n-2$.

This particular method of matrix construction was used as a pattern, and is suitable even for the smallest possible pseudo one-dimensional structure of the form in Figure 4.48. Another method exists that is similar to the method used in Section 3.1 that determines the general form of the impedance matrix of a two-dimensional MI waveguide, where the general form is composed of sub-matrices that describe each row of a waveguide, and the interactions between rows. However a general form can only be seen with a pseudo one-dimensional structure with at least four elements on its leading diagonal.

For the "flared" variation, the method used was to create a matrix of the "tucked" variation, but one that had two extra elements on the leading diagonal of the structure, then to create a smaller matrix from this by deleting the first and last row and column. This was seen as the simplest method given that the general form for the impedance matrix for a near-identical structure had already been derived, and that the first and last elements on the leading diagonal of a tucked structure are associated with the first and last elements on the leading diagonal of its impedance matrix.

The new structures will first have their optimal heights determined via experiment and simulation, and then compared to each other and to conventional one- and two-dimensional structures.

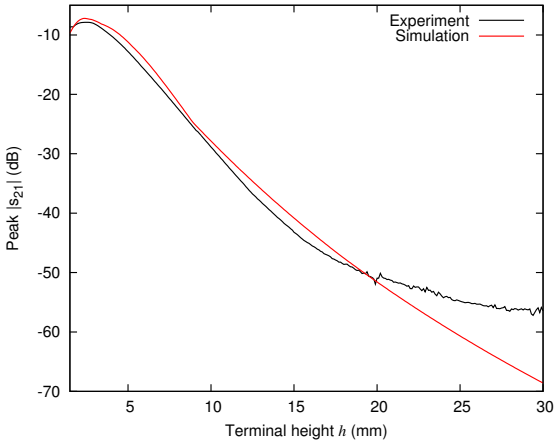
4.3.1.1 Optimal Height

For the experiments, a slightly different approach was taken to the previous sections in so much as the terminals were kept stationary, but the pseudo one-dimensional structures were attached to the stage mover. This method was used as it was easier to align the terminals to the chosen elements. One terminal, named T_x, was attached to port 1 of a HP 8753ES VNA and centred above the element at one end of the diagonal, and the second terminal, R_x, was at the opposite end of the diagonal and attached to port 2. Like previous optimal height experiments, the terminal height, h, was varied from 30 mm to 1.5 mm, and at each h the complex s_{21} was measured at 1601 points between the frequencies of 150–350 MHz.

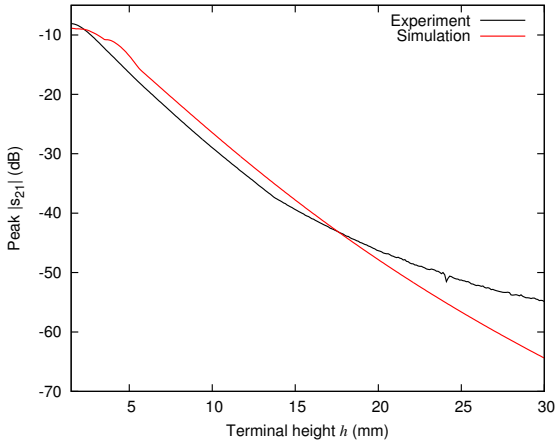
In simulation, all the elements were assumed to have the same characteristics for simplicity, and assumed to have a resonant frequency, f_0, of 239.46 MHz as this was the average of the f_0 of the elements in the one-dimensional 10-element MI waveguide as shown in Section 4.2. The elements were taken to have a resistance, R, of 0.2 Ω as this was the value found in Section 4.2.1 that was deemed to give the best agreement between experiment and simulation.

Figures 4.50a and 4.50b shows good agreement between experiment and simulation, however in simulation the peak $|s_{21}|$ curves show a slight kink for both the tucked and flared variations when h was around 3 mm. Whilst it would seem that the flared structure had not reached its peak $|s_{21}|$ even at the lowest h, the tucked structure however had a peak $|s_{21}|$ of -7.87 dB at 2.4 mm.

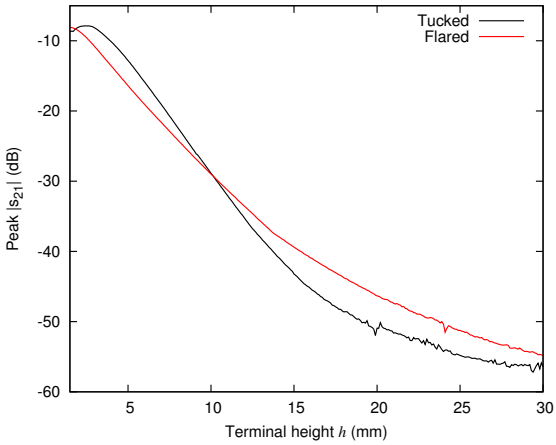
Figure 4.51 shows the comparison between experimental and simulated $|s_{21}|$ for both the tucked, Figure 4.51a, and flared, Figure 4.51b, variations of the pseudo one-dimensional structure. The height at which the $|s_{21}|$ are shown were chosen as this is height at which both structures had the same peak $|s_{21}|$ according to Figure 4.50c. For both the tucked and flared



(a)

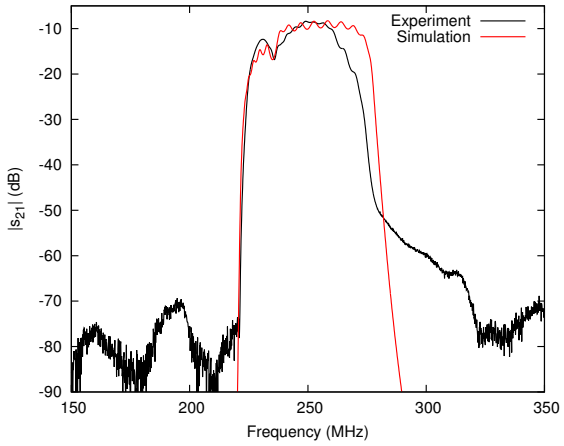


(b)

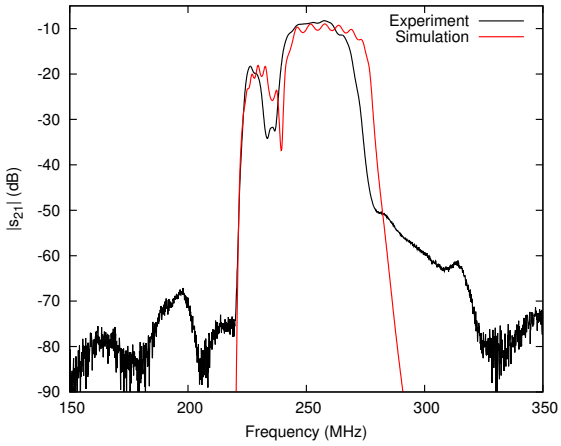


(c)

Figure 4.50 – Comparison of the peak $|s_{21}|$ versus terminal height h between experiment and simulation of the tucked structure (a), of the flared structure (b), and comparison between the experimental peak $|s_{21}|$ versus h of the tucked and flared structures (c).



(a)



(b)

Figure 4.51 – Comparison between experiment and simulation of the end-end $|s_{21}|$ of the tucked structure (a), and the flared structure (b) both at a terminal height of 1.8 mm.

structures, the simulated $|s_{21}|$ width is narrower in comparison to experiment due to the slightly higher value of κ used compared to experiment.

For the flared structure, there is good agreement between experiment and simulation, however for the tucked structure, the experimental response shows a drop off towards the higher frequencies which is not seen in simulation. In experiments, it is likely that the difference in the responses between the two structures is due to how the MI waves travel in them. The flared structure shows a noticeable trough in the passbands in both experiment and simulation. It is believed that this is caused by the extra two elements added at either end of the structure compared to the tucked structure. A small trough exists for the tucked structure also at roughly the same frequency. The difference between the two structures is most likely caused by the location of the extra elements, compared to the tucked structure, that the flared structure has, leading to more destructive interference at the elements below T_x and R_x. It is also possible that the tucked structure has some flaw in one of the elements that causes the drop off in $|s_{21}|$ towards the end of the passband.

4.3.1.2 Comparison to Conventional One- and Two-Dimensional Structures

In this section, the performance of the pseudo one-dimensional structures are compared to conventional one- and two-dimensional MI waveguides. Figure 4.52 compares the end to end $|s_{21}|$ of the 10-element tucked structure, 10-element one-dimensional structure, and the leading diagonal of the 6-by-6 structure at the terminal height h at which the structures attained their peak $|s_{21}|$.

Here one can see that the tucked pseudo one-dimensional structure lies approximately halfway between the one- and two-dimensional structures in terms of bandwidth. Whilst an increase in bandwidth was anticipated, it was hoped that the bandwidth would be closer to that of the two-dimensional structure.

Of course, this then begs the question of how many diagonals one must include before the pseudo one-dimensional structure reaches the same bandwidth as a two-dimensional structure. Figure 4.53 shows the $|s_{21}|$ with a terminal height of 2.4 mm. The pseudo one-dimensional structure with one off-diagonal has roughly 70% of the bandwidth of a fully fledged

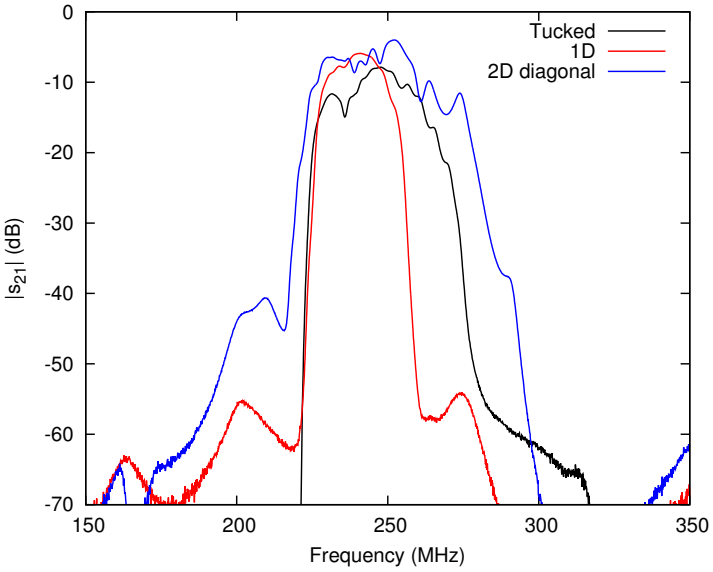


Figure 4.52 – $|s_{21}|$ versus frequency for the tucked 10-element pseudo one-dimensional structure at a terminal height, h, of 2.4 mm (black), 10-element one-dimensional structure at $h = 4.3$ mm (red), the leading diagonal of the 6-by-6 two-dimensional structure at $h = 2.7$ mm (blue). The heights chosen are those at which the peak $|s_{21}|$ occurred for their respective structures.

two-dimensional structure, with two off-diagonals, this increases to nearly 90%, thereafter the improvements are somewhat minimal, moving to three off-diagonals increases the bandwidth to 95% but with five off-diagonals, the bandwidth available is 99% of a two-dimensional MI waveguide.

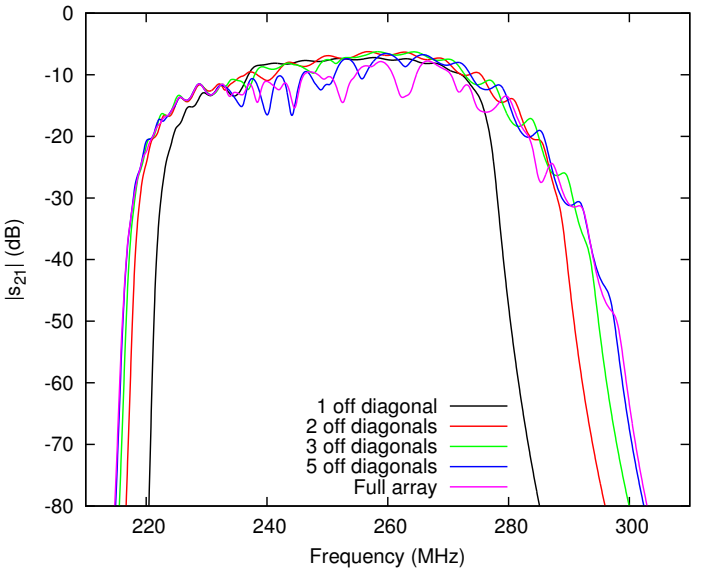


Figure 4.53 – $|s_{21}|$ versus frequency for a 10-by-10 two-dimensional MI waveguide, and 10-element pseudo one-dimensional structures with one, two, three, and 5 off-diagonals with a terminal height of 2.4 mm.

4.3.2 THE METAMATERIAL "FLOWER"

The aim of using square versus circular elements was to increase the inter-element coupling and thus the bandwidth; the aim of the pseudo one-dimensional structure was also to increase the bandwidth available, albeit for the purpose of one-dimensional data transfer.

It has always been possible to achieve a higher inter-element coupling with an axial configuration compared to a planar configuration, however, Syms et al. [50] devised a one-dimensional MI waveguide which was physically planar, but whose elements were axially coupled. Would it be possible to create a similar structure that was two-dimensional in nature? Figure 4.54 shows the construction of an element from such a novel structure.

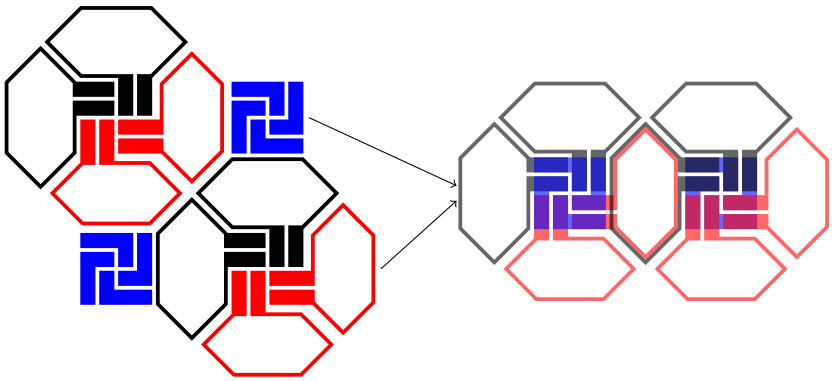


Figure 4.54 – Illustration of the "flower" element's design. On the left is one layer of the design, the right shows when both upper and lower parts are put on separate layers and overlaid. Where each element is composed of two "big" loops (black), two "small" loops (red), and L-shaped plates that help form the self-capacitance of the structure with the pads at the ends of the loops (blue).

As one can see from Figure 4.54, each element is dual layered by design, and its self-capacitance is dominated by the geometry of the areas that overlap. The capacitance of such areas can be easily calculated using the formula for parallel plate capacitors given by (4.9), whereby C is the capacitance, ϵ_0 the permittivity of free space, ϵ_r the relative permittivity, A is the area of the overlap, and d the distance between the areas,

$$C = \frac{\epsilon_0 \epsilon_r A}{d}. \tag{4.9}$$

The nature of this design allows the cells to be tiled into a two-dimensional structure.

FastHenry was used to calculate the structure's self inductance; the square element of Section 4.2 is evidently quite simple to construct out of parallelepipeds, and the resultant object would be the element. The "flower" element, however would be constructed of several objects, each with their own inductance and mutual inductances to other objects within the element. As the element is dual layered, some asymmetry between the sizes of the loops was desired as in the case of the dual layered design used by Syms et al., the parts of the element that would overlap should the element be symmetrical would also generate some capacitance between elements. As such, two of the four loops should be smaller to prevent such a capacitance being generated. Figure 4.55 gives an overview of the geometry of each type of loop and the L-shaped plates that join these loops via a capacitance, the detailed geometry is given in Appendix A.

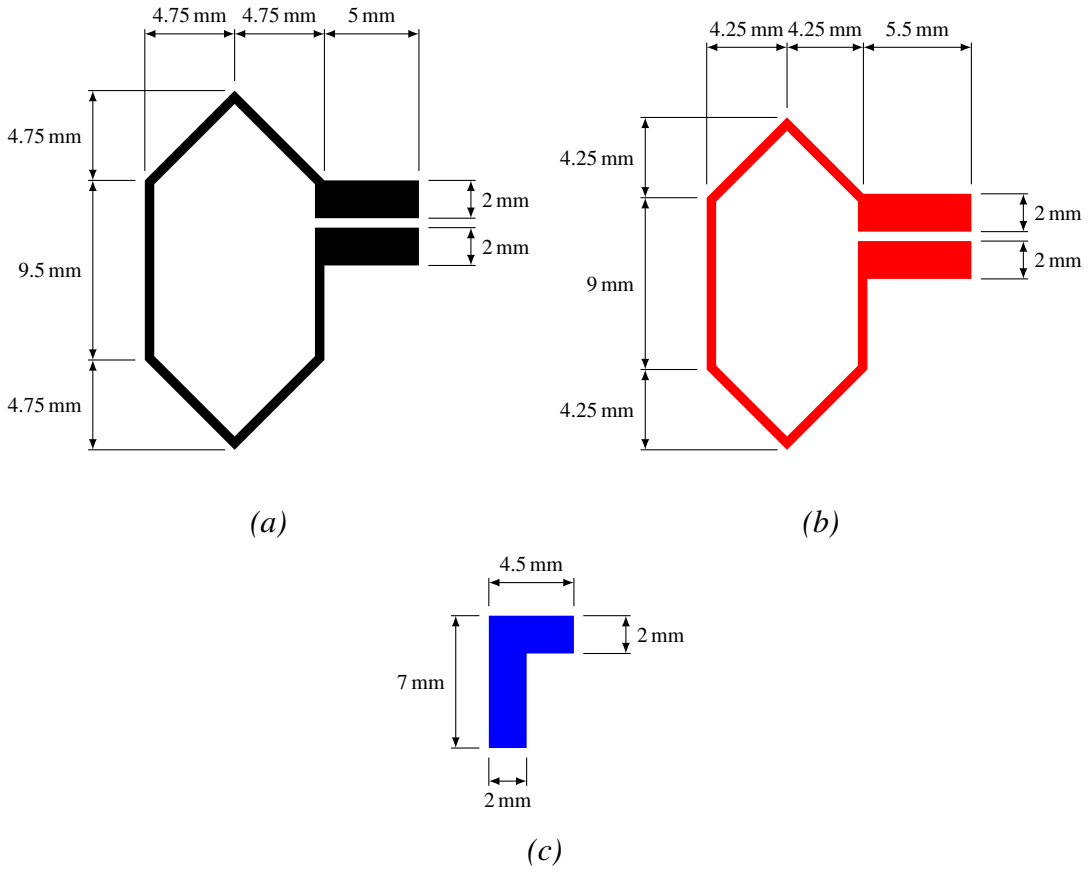


Figure 4.55 – The approximate geometry of the bigger loop (a), smaller loop (b), and the L-shaped capacitive plate (c) that make up the elements in Figure 4.54. Unless stated otherwise, the track width is 0.5 mm. All components are centred on coordinates of choice, and rotated into their requisite positions. Detailed geometry given in Appendix A.

The substrate upon which this "flower" structure was to be constructed was evidently an important factor to be considered as this controls the capacitance and thus the resonant fre-

quency, f_0, and also the quality factor, Q, dependent on both the dielectric loss and skin effect. It was decided that Espanex MB18-25-18FRG would be used, this is an adhesive-less copper clad laminate with 25 μm of polyimide sandwiched between 18 μm of copper foil. An adhesive-less flexible substrate was desired as the capacitance would be dependent on the distance between the layers, the smaller this distance, the greater the capacitance and thus the lower the f_0. A rigid substrate would likely have a thickness that would give rise to a very small capacitance, and a flexible substrate with adhered copper layers would lead to a lower Q as the adhesives used have a much higher dielectric loss than the substrate alone. One might think that a lower f_0 would be undesirable, however, the element shown in Figure 4.55 is much larger than the previously used square elements (29 mm across versus 9.5 mm), and thus should f_0 be too high, the element would no longer be considered electrically small and thus the effects of retardation would have to be considered.

Per element, there are eight sections where tracks overlap to form the element's capacitance, and each has an area of 9 mm^2, the ϵ_r of Espanex MB18-25-18FRG is 3, and with its thickness of 25 μm this gives a total capacitance of 1.195 pF. The calculated inductance of a single element is 129.01 nH giving an expected f_0 of 405.29 MHz. The estimated coupling is 0.160, giving expected one- and two-dimensional bandwidths of 65.82 MHz and 138.53 MHz respectively.

To test the behaviour of a structure composed of such elements, a single element was constructed so that an individual element's characteristics, f_0 and Q, could be measured. As the characteristics of the element are entirely determined from the geometry and the properties of the substrate, it was assumed that when the elements were used in a waveguide, that their properties would have a sufficiently low variance that it could be ignored. A double element was also fabricated to measure the coupling between two elements. An 8-element one-dimensional waveguide and an 8-by-8 two-dimensional waveguide were also made. Whilst each element would be 29 mm across, the distance between the centres of adjacent elements would be 20 mm due the fact that one loop of one element would overlap one loop of the other to provide the coupling between elements. The substrate was fabricated by P.W.Circuits Ltd. and the largest

area that could be used had a width of 7” (177.8 mm) and height of 11” (279.4 mm), and that is the reason for the sizes of the waveguides as the length of an 8-element strip would be 169 mm.

To ascertain the qualities of the elements, a clamp, shown in Figure 4.56, was made to house the flexible substrate. Two 2 mm plates of acrylic sandwich the substrate with a visible area of 180 mm by 180 mm. This is clamped together by two 6 mm sheets of Polyvinyl chloride (PVC) with a 180 mm by 180 mm cut out in the centre with 12 ISO M4 nylon bolts and nuts. This is then attached to the perspex back board of the electronic stage mover set up, using a bracket also made of PVC such that the clamp would stand upright within the electronic stage mover.

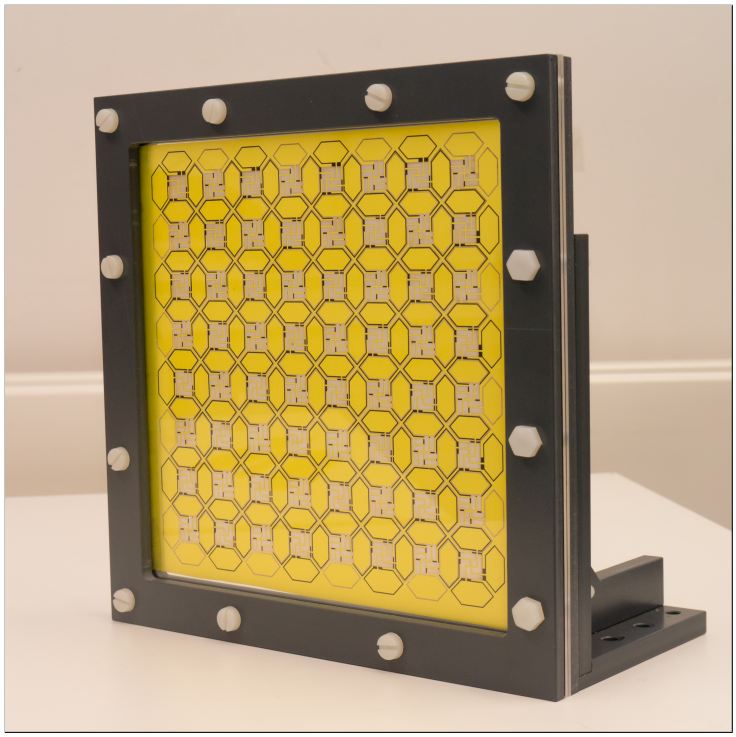


Figure 4.56 – Photograph of the clamp used to hold samples, with an 8-by-8 two-dimensional MI waveguide formed of “flower” type elements within.

To measure the characteristics of an element, it was placed inside the clamp and two hexagonal loops probes, as shown in Figure 4.57, were used to both excite and measure the response of the element. The hex probes were 12 mm away from the surface of the element with both probes centred above the same loop in the element, and 1601 points of complex $|s_{21}|$ data were taken in the 320–520 MHz range by a HP 8753ES VNA.

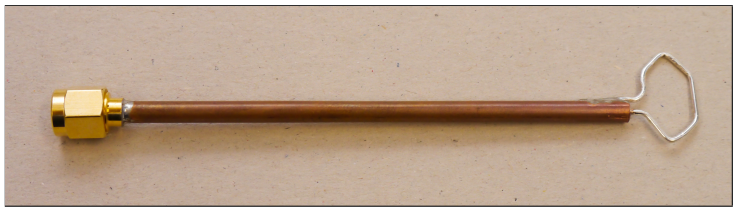
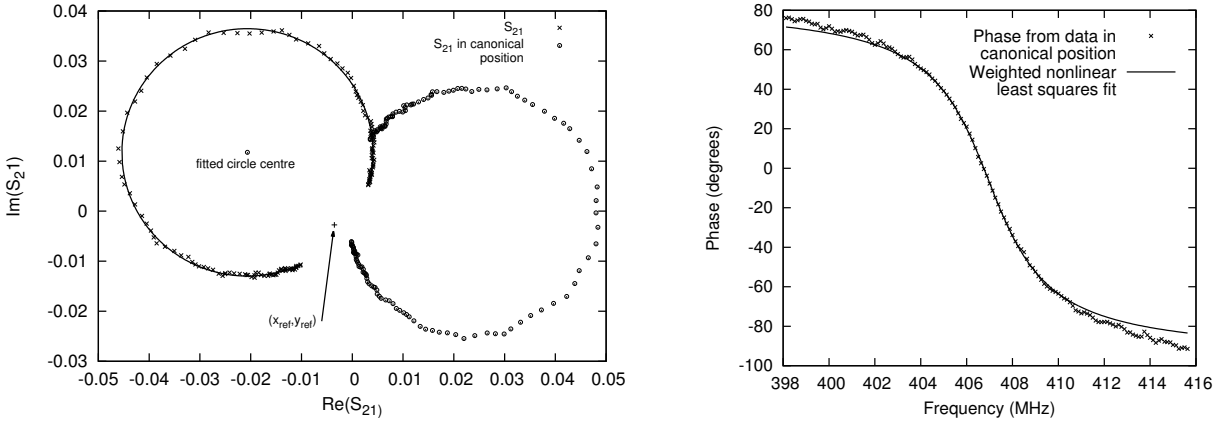


Figure 4.57 – Example of a hexagonal loop probe, the loop is formed from the inner conductor of RG402/U semi-rigid coaxial cable. The hexagonal loop has the same dimensions as the larger hexagonal loop of the "flower" element.

The circle and phase fit method described in Section 4.1 were used to find the resonant frequency, f_0, and the quality factor, Q, of the element shown in Figure 4.60a. This method yielded a f_0 of 406.96 MHz and Q of 104.68. Given the self capacitance of the "flower" element, this would lead to an experimentally derived inductance of 127.96 nH.



(a) *(b)*

Figure 4.58 – The complex s_{21} data for the single "flower", with the fitted circle centre, the fitted circle, and the data in the canonical position (a), and the phase versus frequency points from the data in the canonical position with the non-linear least squares fit (b).

A similar method was used to measure the coupling between elements, the arrangement shown in Figure 4.60b, however there are evidently many positions for the loop probes to occupy. The probe that excites the element, connected to port 1 of the VNA, could be placed on any four of the loops of an element, symmetry means that it would not be necessary to place it on the loops of the other element. The second probe, connected to port 2 of the VNA, could be placed upon any of the loops of both elements, although two of these loops would overlap providing the coupling between the elements. However, measurements in all possible configurations yielded the same coupling of $\kappa = 0.244$, and would thus give a bandwidth of 103.17 MHz

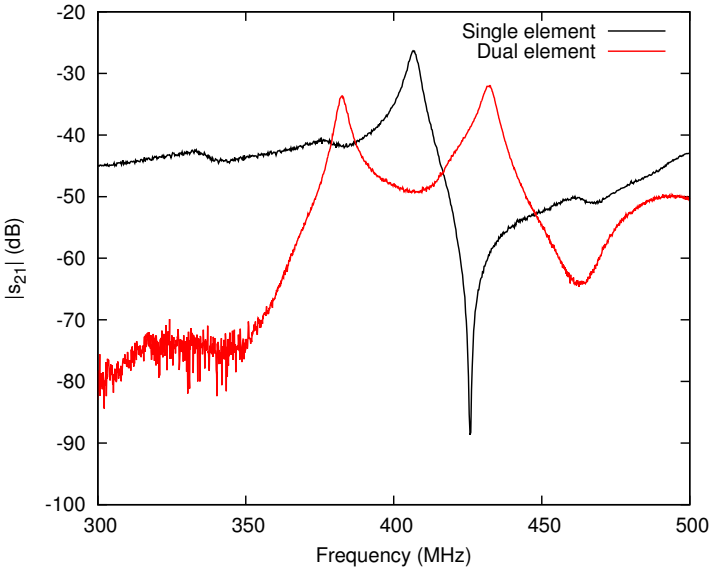
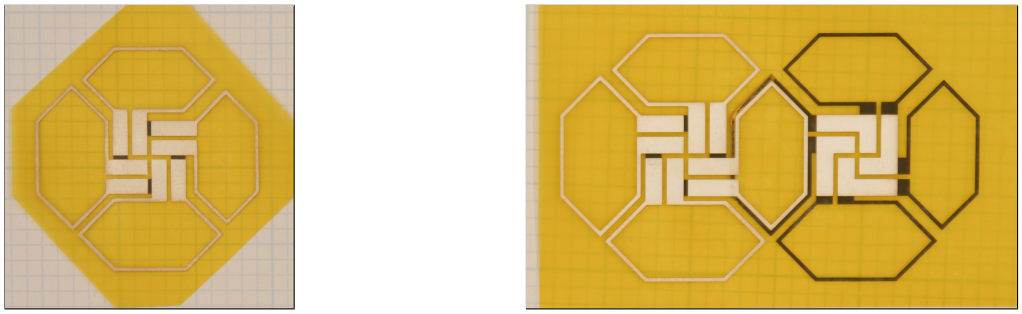


Figure 4.59 – $|s_{21}|$ versus frequency for the single "flower" (black), and for the dual "flower" (red).



(a) *(b)*

Figure 4.60 – Photograph of a single "flower" element with a resonant frequency, f_0 of 406.96 MHz and a quality factor, Q, of 104.68 (a), and a photograph of a two "flower" elements coupled together with a coupling of 0.244 (b).

and 235.12 MHz for a one- and two-dimensional waveguide respectively.

Interestingly, the calculated inter-element coupling is much less than that derived from experiment, 0.160 versus 0.244. It is probable that the most likely cause for this would be potential capacitive coupling between adjacent elements as this has not been accounted for in the model. It's also possible that the areas that make up the elements' self-capacitance, could also behave like a ground plane. This limits the paths that the flux lines that link the elements together can take and thus increase the magnetic coupling.

4.3.2.1 ONE-DIMENSIONAL

The method of testing the "flower" based structures was somewhat challenging, as each element is composed of several loops. The rightmost element was labelled element 1, and the leftmost element 8, and with this orientation, each of the loops in the "flower" element were simply named the "top", "right", "bottom", and "left" loop when looking at the loop with the waveguide in the aforementioned orientation.

Resonant hexagonal loop probes were used, pictured in Figure 4.61. As these probes are expected to have approximately a quarter of the inductance of a "flower" element, to have the same resonant frequency, one would have to add a capacitance four times that of the element, and the closest standard capacitor to this had a value of 4.7 pF. In Section 2.4, a relation between the terminal-waveguide coupling and the inter-element coupling was given (2.33). Thus, for this one-dimensional MI waveguide, it would be desirable for the terminal-waveguide coupling to be double that of the inter-element coupling. However the inter-element coupling of 0.244 was achieved across the 25 μm flexible substrate, and as such it would be difficult to provide the optimum coupling for the "flower" based structure when installed in the clamp. Thus it was decided that the probes would be placed at a convenient distance from the MI waveguide, for the purposes of ascertaining the bandwidth, and comparison to simulation.

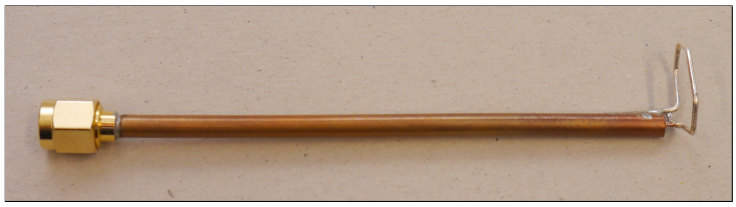


Figure 4.61 – An example of a resonant hexagonal loop probe with a capacitor soldered at the base of the loop.

The 8-element one-dimensional MI waveguide produced is shown in Figure 4.62. Whilst each element is 29 mm across, the overlap between adjacent element means that they are spaced 20 mm apart, giving the 8-element waveguide a total length of 169 mm.

As one might imagine, when using hexagonal loop probes such as those in Figure 4.61 and Figure 4.57, where one desires the highest coupling at a given height to the elements in the

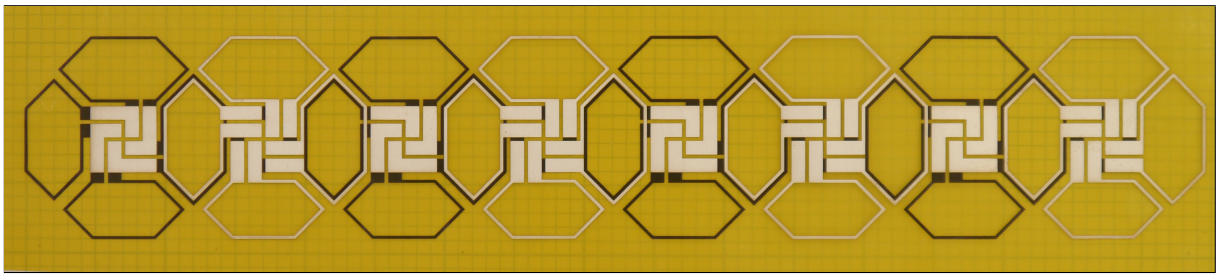


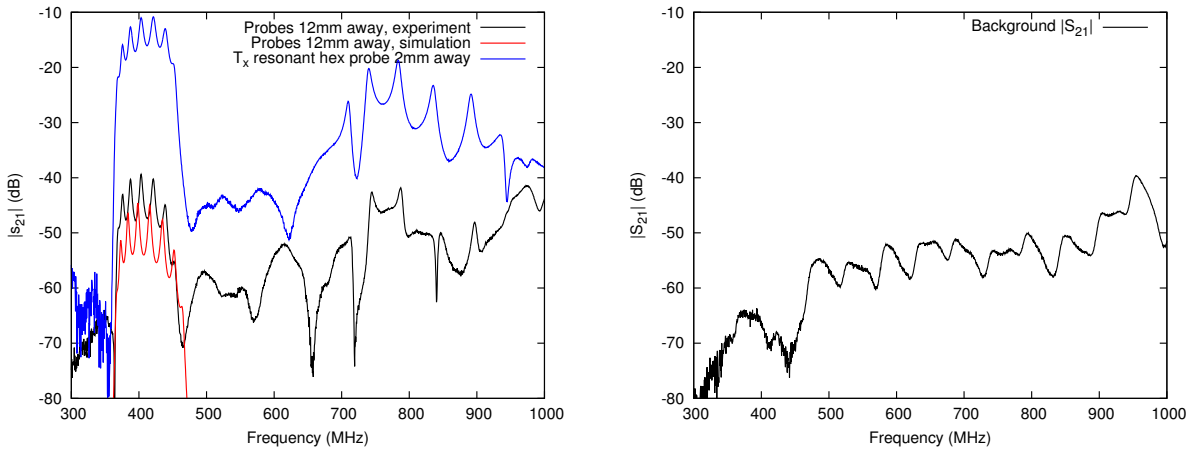
Figure 4.62 – Photograph of a "flower" based 8-element one-dimensional MI waveguide.

waveguide, that the probes would have to be aligned with one of the four loops in an element. However, there would be some situations where the probe would be strongly coupled to two adjacent elements as those places are also where the elements couple to adjacent elements.

With this in mind, when it comes to simulating such a structure, it was decided that a simple approach was most appropriate whereby each element was only composed of a single inductance, capacitance, and resistance. Whilst it might be possible to couple the probe to two adjacent elements in simulation, it was decided that this should be avoided and to only use comparisons with experiments where the probe was predominantly coupled to one element.

As in previous experiments, the probe referred to as "T_x" was connected to port 1 of the HP 8753ES, and "R_x" connected to port 2. For the responses shown in Figure 4.63, T_x and R_x were at opposite ends of the waveguide, with the black and red lines showing experiment and simulation respectively for having both probes as hexagonal resonant probes 12 mm away from the surface, and the blue line when the probes were 2 mm from the surface. The expected coupling of a probe to an element with one loop aligned 12 mm away from it was calculated using FastHenry as 1.826×10^{-2}. T_x was above the right loop of the first element, and R_x above the left loop of the eighth element. When the probes were 2 mm away this increased to 9.475×10^{-2}, and the coupling to the adjacent element was calculated as -8.306×10^{-3}. The background was also measured and subtracted, Figure 4.63b gives an example.

The bandwidth that each of the response curves displays is in line with the expected bandwidth for this structure of 103.17 MHz. There is a moderate difference of 5 dB between experiment and simulation when the probes are 12 mm away from the waveguide. This is believed to be caused by an underestimation of the terminal-waveguide coupling. One can also



(a) *(b)*

Figure 4.63 – Comparison of $|s_{21}|$ versus frequency for end-to-end transmission with resonant hexagonal probes 12 mm from the MI waveguide, experiment (black), simulation (red), and with resonant hexagonal probes 2 mm away from the MI from the waveguide (a). Background $|s_{21}|$ for two hexagonal resonant probes as if they were at either ends of the waveguide with the clamp still present (b).

clearly see a higher level of transmission above 600 MHz, rivalling the magnitude of the MI passband. When T_x is moved much closer to the waveguide, overall transmission increases greatly, especially within the passband by 30 dB, however the relatively high level of transmission after 600 MHz persists. It is believed that, due to the size of the waveguide itself, that there was some radiation coupling at higher frequencies.

Evidently, the overall end-to-end transmission when the probes were 12 mm away was poor due to the low terminal-waveguide coupling. Whilst this improved drastically when moved to 2 mm from the waveguide, it is not possible to provide optimum coupling in a practical situation to the waveguide due to the proximity required.

4.3.2.2 TWO-DIMENSIONAL

Figure 4.64 shows the 8-by-8 element "flower" based two-dimensional MI waveguide. One can see that an element could also couple to elements that are diagonal to them as well as those that share loops with it. As such, it was decided that the second nearest-neighbour coupling was also to be included in simulations, but as a physical version was not fabricated, FastHenry was

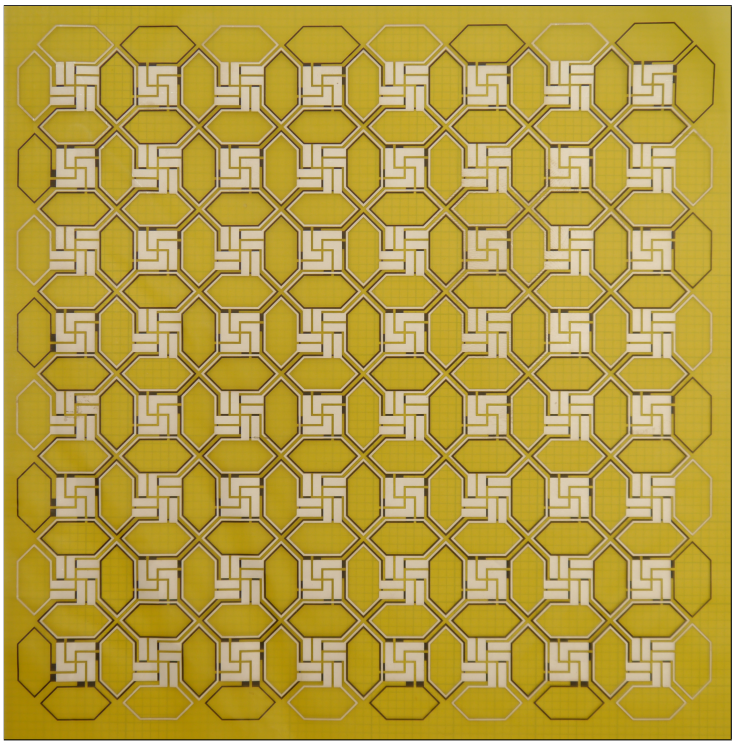


Figure 4.64 – Photograph of the 8-by-8 two-dimensional "flower" based MI waveguide.

called upon to provide an estimate of the coupling. The apparent coupling between elements diagonal to each other is -7.007×10^{-2}.

The array was numbered (1,1) at the bottom right and (8,8) in the top left following the matrix (row,$column$) notation. Two T_x-R_x configurations were considered, transmission along one edge and along the diagonal and do T_x was fixed above the right lobe of (1,1) and R_x on the left lobe of (1,8) for the edge configuration and the left lobe of (8,8) for the diagonal configuration.

Whilst the experiments for the two-dimensional "flower" based waveguide were also carried out with the two terminal heights used during the one-dimensional experiments, two resonant probes 12 mm from the waveguide and at 2 mm from the waveguide, the results presented in this section will only include those with the latter configuration.

From Figure 4.65b, one could say that the observed bandwidth is approximately 200 MHz, not the 235.12 MHz as predicted earlier. However, in the edge transmission case shown in Figure 4.65a, the bandwidth appears to stretch from 400–800 MHz in experiment, though is this is likely not attributed to MI waves and possibly due to radiation after 600 MHz. For both cases,

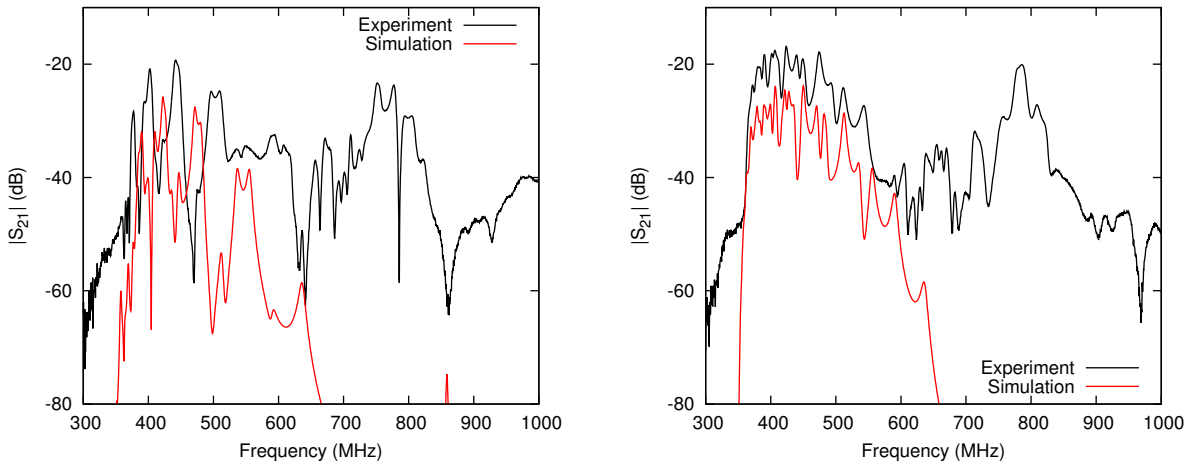


Figure 4.65 – Comparison of experiment and simulation when T_x is a resonant hexagonal probe and is 2 mm from the waveguide, and R_x is a loop probe of 9 mm outer diameter 22 mm from the waveguide with T_x at (1,1) and R_x at (1,8) (a), and at (8,8) (b).

there's a difference of approximately 7 dB between simulation and experiment within the MI band. Again, this is believed to be caused by an underestimation of the coupling between the probe and the waveguide.

Compared to the experiments on the MI waveguides composed of the square elements, both of the "flower" based waveguides in this Chapter have been fabricated of a comparable length. However, for the two-dimensional "flower" based waveguide, peak $|s_{21}|$, both along its edge and along the diagonal, were noticeably worse than the one-dimensional waveguide (-19.287 dB and -16.878 dB respectively versus -10.814 dB). It is believed to be caused from the expansion from one to two dimensions as now, the resistance of the waveguide, as seen from the transmitter has been greatly increased due to the addition of many extra elements. Figure 4.66 shows how the impedance changes between one- and two-dimensional "flower" waveguides.

In Figure 4.65b, the transmission within the passband appears to decrease towards its end, this is believed to be caused by the comparatively narrow response of the terminals. In contrast to the passband of the square-element MI waveguide in Section 4.2, and even that of the one-dimensional "flower" element waveguide, the two-dimensional "flower" waveguide's passband is significantly wider.

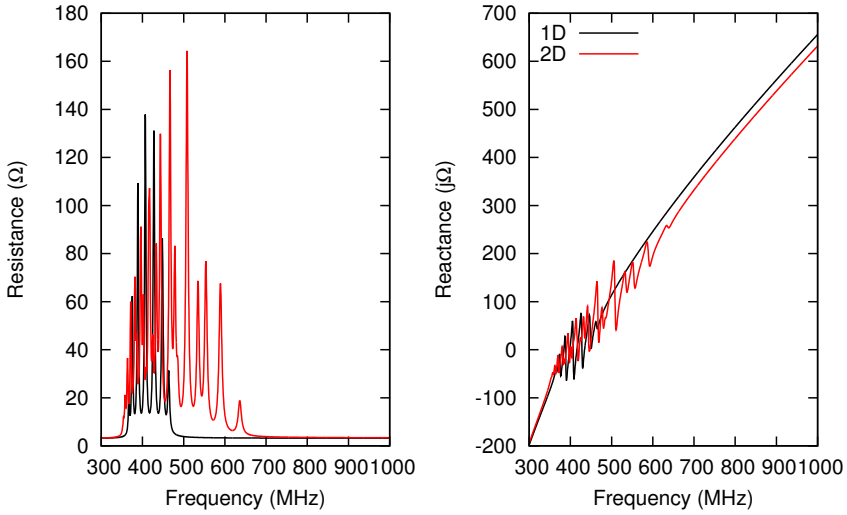


Figure 4.66 – Graphs of resistance versus frequency (left), and reactance versus frequency (right), for both one- and two-dimensional MI waveguides composed of "flower" elements. Impedance as seen through the first element in a one-dimensional waveguide of 8 elements, and in the corner of a 8-by-8 two-dimensional waveguide.

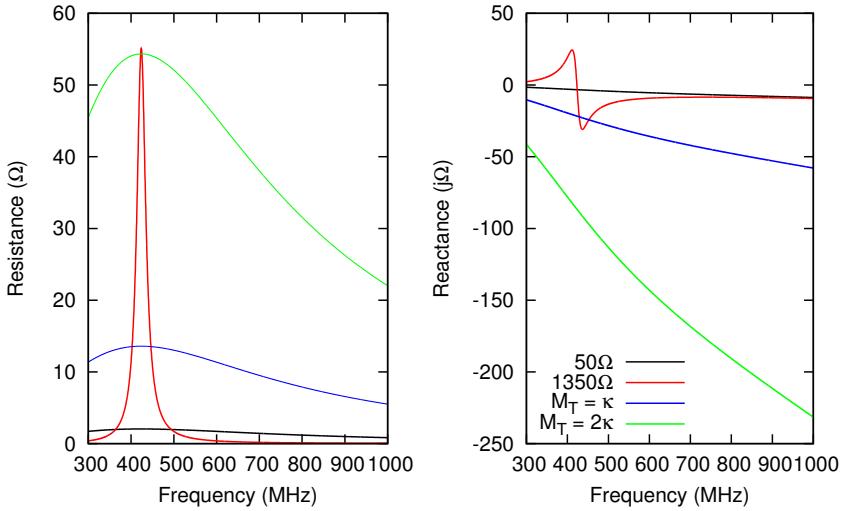


Figure 4.67 – Graphs of resistance versus frequency (left), and reactance versus frequency (right), for a parallel type terminal with $L = 30\,nH$ and $C = 4.7\,pF$ and a load of $50\,\Omega$ as used in experiments (black), with a $1350\,\Omega$ load (red), with a $50\,\Omega$ load and a terminal-waveguide coupling of κ (blue), and a terminal-waveguide coupling of 2κ (green).

Figure 4.67 shows a comparison of the impedance of various parallel-type terminal configurations. The method used is described in Section 3.2.4, whereby the terminal is converted into an impedance within the element it is coupled to. This is so that it can be compared with the apparent impedance presented by the waveguide as shown in Figure 4.66. The black line shows the impedance of the terminal used in experiments as shown in Figure 4.61, at the terminal-waveguide separation of 2 mm. One can clearly see that it is a poor match for its placement

in the waveguide. This is not just due to the difference in resistance, but according to Sydoruk [53] there will be no reflection from the load if it is the complex conjugate of the waveguide's characteristic impedance.

If the load attached to the terminal were to be increased to 1350 Ω, shown by the red line in Figure 4.67, its peak resistance would approach that of resistance presented when in the corner of the two-dimensional waveguide. However the shape of this curve as well as the reactance of this configuration is clearly a poor match for the waveguide.

Another factor to consider is the coupling between terminal and waveguide found by our previous work [21], and confirmed by Sections 4.2.1.1 and 4.2.1.2, that the optimum terminal-waveguide coupling occurs when $|\kappa_x| \approx 2\eta_x|\kappa|$. The terminal-waveguide coupling was limited in experiment due to the 2 mm layer of acrylic either side of the waveguide. As the terminal used was a similar shape to a loop of the "flower" element, the terminal-waveguide separation would have to be less than the thickness of the substrate of the waveguide itself to achieve optimum coupling.

However, if the terminal used in experiments could've gotten closer to the waveguide, the green and blue lines in Figure 4.67 show the cases whereby $\kappa_x = \kappa$ (green) and $\kappa_x = 2\kappa$. Evidently when the terminal-waveguide coupling improves, both the shape and magnitude of the resistive part of the load are more similar to that of the waveguide. However the magnitude of the reactive element of the load is still insufficient even when $\kappa_x = 2\kappa$.

As Figure 4.65 shows, whilst transmission is expected in the MI passband below 570 MHz, there is just as much transmission between 750–850 MHz. This was also the case for the one-dimensional waveguide as Figure 4.63 illustrates. Evidently, this behaviour is not simulated by the simple circuit model.

Figure 4.68 shows how $|s_{21}|$ changes with frequency and position for a slice in the middle of the one-dimensional "flower" based waveguide. In the 350–450 MHz region one can clearly see the MI passband and the forward waves, the number of standing waves increases with frequency, that one would expect from a structure of positive inter-element coupling. Looking

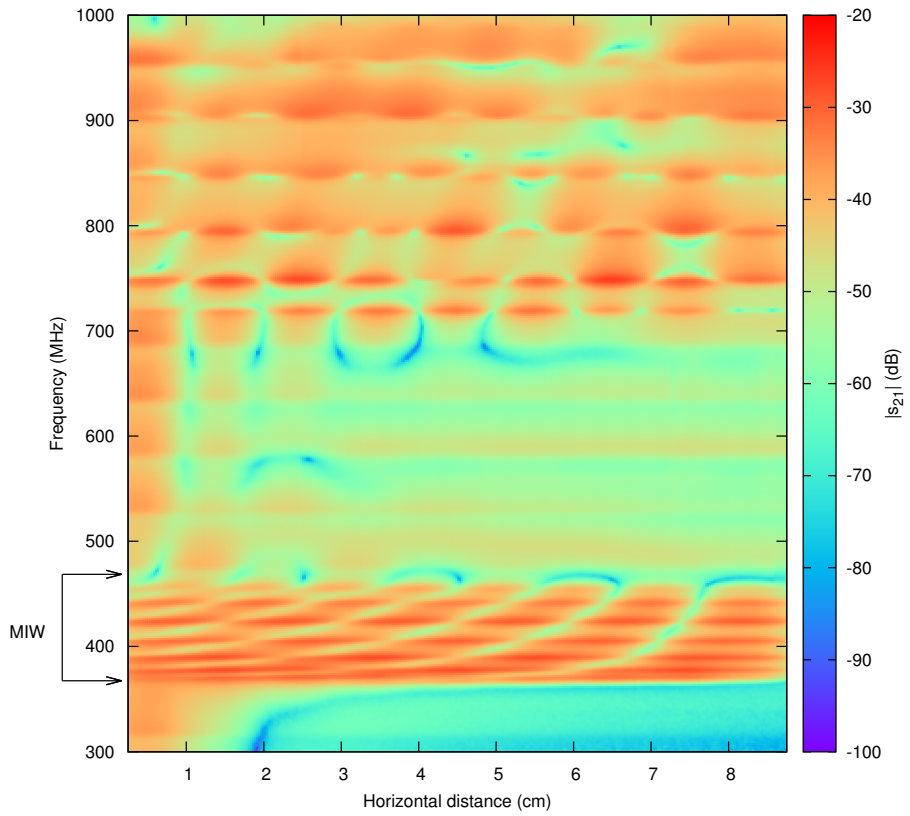


Figure 4.68 – $|s_{21}|$ map for the 8-element one-dimensional "flower" based MI waveguide. This shows the $|s_{21}|$ for frequencies between 300–1000 MHz, for a scan along the midsection of the waveguide. The band where MI waves propagate is labelled "MIW."

at the lines of $|s_{21}|$ at 720 and 750 MHz, the minima actually occur at the centre of each element, that is to say over the section of the element that's responsible for the element's self-capacitance. It's possible the comparatively large amount of metal in these areas behave like a distributed ground plane [66].

Another possibility is that elements behave in a way that cannot be predicted by using a simple circuit model, perhaps there are other characteristics that are unknown such as the interactions between the individual parts that make up an element, or how these parts interact with an adjacent element's constituent parts.

Figure 4.69 supports this to an extent as one can clearly see that within the MI band, Figure 4.69a, there are clear vertical separations between waves and it would appear that elements behave as individuals. However in the region where transmission was not expected, Figure 4.69b, one can clearly see that there would likely be differences in the current within an element's constituent parts as the minima now actually coincide with the middle of an element.

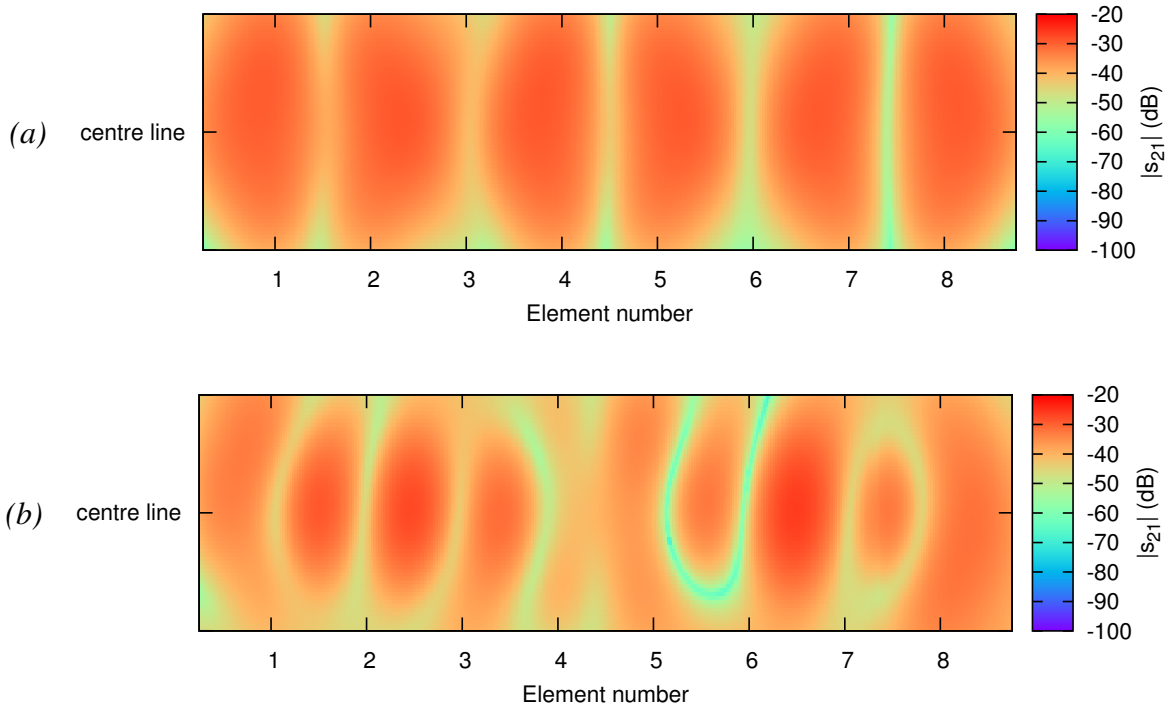


Figure 4.69 – A raster scan of $|s_{21}|$ of the area occupied by the one-dimensional "flower" based waveguide at the frequencies of 424.6875 MHz (a) and 749.75 MHz (b). T_x, a hexagonal loop probe, was above 2 mm above the left most loop, and R_x, a loop probe of 9 mm outer diameter, was scanned in 0.5 mm steps in both the x and y directions.

CHAPTER 5

CONCLUSIONS AND FUTURE WORK

The ultimate aim of this work is to enable the use of MI waves as a means to perform contactless data communication. In Chapter 1, a potential application for MI waveguides was presented along with a brief history of the research into MI waves for data and power transfer and the origins of contactless data transfer in the form of RFID.

In Chapter 2, a brief history of the MI waveguide was covered. The characteristics of the elements that make up a MI waveguide were covered along with the origins of the MI wave in both one and two dimensions. This led to the generic dispersion curves for both positively and negatively coupled MI waveguides.

In Section 2.3.1, it was shown that bandwidth for a two-dimensional MI waveguide was expected to be double that of a one-dimensional one. Also the bandwidth is anisotropic, and whilst the maximum bandwidth remains the same for both positively and negatively coupled MI waveguides, the variation of bandwidth with angle is greatest for the former.

A greater bandwidth is an attraction of moving from a one- to a two-dimensional MI waveguide as this would allow for a greater data capacity through it. However, as discussed in Section 2.4, bandwidth is one of many variables that can affect the capacity of a MI waveguide. Some of these variables are inherent to the waveguide, such as the coupling, the quality factor,

and element variation, however external factors such as terminal design and terminal-waveguide coupling are also important.

Chapter 3 covers how MI waveguides and terminals can be modelled for the purposes of simulation and discusses some of the issues involved in the process.

With the knowledge gained in the previous chapters, Section 4.2 investigated a MI waveguide based on square elements that aimed to improve upon attempts previously based on circular elements [21], and to further the understanding of the MI waveguide environment. By using square elements that are more space filling, and also of a higher resonant frequency, the bandwidth rises from 6 MHz [21] to just over 36 MHz for a one-dimensional waveguide. Expanding this to two dimensions, the available bandwidth increased to just over double at 75 MHz.

In Section 4.2.1, it was found that peak capacity and peak transmission through a MI waveguide do not necessarily occur at the same height due to shape of the $|s_{21}|$ curves. For the two-dimensional waveguide studied, and the various terminal configurations considered, there was evident symmetry in both the shape and magnitude of the $|s_{21}|$ curves for equivalent terminal configurations. Also peak capacity occurred at approximately the same height for the configurations considered. Evidently this is a convenient property as one would be able to use the same height for any terminal configuration and achieve a near optimal capacity through the waveguide.

Having considered how the terminal-waveguide separation might affect the performance of a MI data transfer channel, Section 4.2.2 sought to assess the effect of a third "blocking" terminal upon the transmission between two other terminals. As a MI waveguide is composed of several elements, and as each element would be capable of coupling to a terminal as well as the adjacent elements, one might reasonably expect a system incorporating such a waveguide to be capable of supporting multiple terminals. For a one-dimensional system, one might initially think that a third terminal would intercept the transmission between two terminals, however it was shown that it only affected the end-end capacity of a 10-element waveguide by $\approx 8\%$. In addition, when the "blocking" terminal was in between two elements, the capacity between the

two other terminals was at its highest as the "blocking" terminal was most weakly coupled to the waveguide at that point.

In Section 4.2.2.2 the affect of a third "blocking" terminal on the capacity between two-terminals on a 6-by-6 element two-dimensional MI waveguide was studied. Two cases were considered, where the terminals were at opposite ends of the same edge, and in opposite corners as it was shown in Sections 4.2.1.3 and 4.2.1.4 that these were the configurations of lowest and highest transmission. It was found that the transmission was most affected when the "blocking" terminal was on the same positions as the other two terminals. However, taking those configurations aside, the capacity was negatively impacted by up to 10%, but in some positions, the capacity was increased. Interestingly, the "blocking" terminal appeared to either be absorbing certain frequencies or removing destructive interference when the capacity was negatively or positively affected respectively.

Having studied the behaviour of MI wave data transfer systems with regards to the interaction between waveguide and terminals, Section 4.3 looks to improve the capacity of such systems via the expansion of bandwidth. The first method, studied in Section 4.3.1, was to create a pseudo one-dimensional MI waveguide by taking an equivalent two-dimensional waveguide, but preserving only the leading diagonal and the first two off-diagonals. This increased the bandwidth of a "one-dimensional" structure, however its bandwidth did not approach that of a two-dimensional structure. It was found that this pseudo one-dimensional structure had 70% of the bandwidth of a fully fledged two-dimensional waveguide and that by adding more diagonals, the bandwidth would approach that of a full array.

The second method was to simply increase the inter-element coupling and this was done in Section 4.3.2 by an element geometry with a dual layer design. This was done as it was not deemed possible to increase the inter-element coupling with a design confined to a single layer. This lead to a near doubling of the coupling constant (κ) compared to the square element waveguide in Section 4.2. Though this did come with its problems, as the inter-element coupling was so high and achieved over a very small distance, the terminal-waveguide coupling would need to be even greater and this was not achieved during experiment due to the physical constraints

of the set up. These devices also displayed some unexpected behaviour at higher frequencies perhaps due to the significantly more complicated nature of the elements themselves, or that the simple circuit model was not sufficient to model this design of element.

The key discoveries of this work are that the bandwidth of a two-dimensional MI waveguide is anisotropic, that there are several factors, including element characteristics and terminal design and coupling, that affect the capacity of an MI waveguide. Peak capacity and peak transmission do not necessarily occur at the same terminal-waveguide height, as it is the broadness, along with the magnitude of the transfer function that leads to a greater capacity. Having a third "blocking" terminal does not affect the capacity between two terminals severely and, in some situations, can improve the capacity, meaning that MI waveguides are indeed suitable for multiple terminal systems. Building a pseudo one-dimensional structure, by truncating a two-dimensional structure does provide a larger bandwidth than a purely one-dimensional structure. It is possible to increase the bandwidth of a two-dimensional MI waveguide compared to previous attempts by utilizing an element with a dual-layered design.

This work has clearly improved the capacity of MI wave communications systems compared to previous attempts, and has also begun the investigation into the behaviour of such a system with multiple terminals. However, there is evidently more that could be done to better understand the system and ascertain its suitability as a data communications channel.

With regards to the behaviour of terminals in such a system, a limitation of the environments studied within this work was the scale of the environments. All the waveguides studied are sufficiently small so as to allow standing waves via reflections from the ends or edges of the waveguide. Whilst not necessarily a problem in of itself, but it is possible that the system would behave differently were the waveguides sufficiently large such that reflections were suppressed via absorption. One could also consider the use of absorbing regions surrounding the waveguide to minimise reflections.

The affect of a "blocking" terminal has only been assessed between terminals that are on the edges of the waveguide. Perhaps, in a confined environment the "blocking" terminal

would also act to reduce destructive interference between two terminals that were located more centrally. Were the terminals not on the edges of the waveguide, this would no doubt change how the system behaved in a fashion, even with two terminals only, that has not been covered in this work.

This work has also highlighted the importance of terminals in the MI wave data communications system. There was an evident optimum level of coupling which, in terms of capacity, fortunately didn't vary too much for the two-dimensional system studied. However, although not immediately obvious, it is possible that as the terminals used weren't efficient even at optimum coupling which lead to the relatively small effect that the "blocking" terminal had on the systems studied. Although the optimizations of terminals has already been studied to an extent[52, 53], this has been limited to their desired application whereby the terminal was coupled to the waveguide at the ends only and the terminal-waveguide coupling was equal to the inter-element coupling and this coupling was compartively high, $\kappa \approx 0.7$. The methods used could certainly aid in finding the optimal coupling transducer, however this would have to vary on depending on the position of the terminal for both one- and two-dimensional systems. This is due to the impedance that a terminal would see in different positions along the array. Take a one-dimensional waveguide, with its characteristic impedance (2.18), $Z_T = j\omega M \mathrm{e}^{-jkd}$, as covered in Section 2.3. However this impedance would terminate one end of a one-dimensional MI waveguide, if one were to couple in the middle of an infinite waveguide, the element it couples to would have the equivalent of two of these terminating impedances. A characteristic impedance for two-dimensional waveguides has not yet been determined, and of course, would change for different positions.

The discrepancy between the measured and calculated coupling should be investigated, either through experimentation, to determine whether there is capacitive coupling between elements, or through the use of an electromagnetic simulator. The root of the unexpected behaviour of the "flower" element would have to be ascertained as its high inter-element coupling for a two-dimensional structure, compared to a single layer design, would evidently prove useful to a system where higher capacity is desired. Use of an electromagnetic simulator may lead to

further insight on the issue. One could also measure the electromagnetic field at a distance from the waveguide to check for far-field radiation.

The most obvious direction for future work would be to develop a simple system in order to transmit data over already existing terminals and waveguides. Perhaps to also assess the effect of the dispersive nature of MI waves and its effects on data streams, and to counteract any issues that arise. Of course then, one would ask, what are realistic data rates that one could achieve with a MI wave data communications system? Perhaps there may be a trade off of dispersion versus bandwidth, or possibly even physical size and bandwidth as the device must remain sufficiently electrically small.

PUBLISHED WORK

C. J. Stevens, C. W. T. Chan, K. Stamatis, and D. J. Edwards, "Magnetic Metamaterials as 1-D Data Transfer Channels: An Application for Magneto-Inductive Waves," *IEEE Transactions on Microwave Theory and Techniques*, vol. 58, no. 5, pp. 1248–1256, May 2010.

C. W. T. Chan, and C. J. Stevens, "Two-Dimensional Magneto-Inductive Wave Data Structures," *Proceedings of the 5th European Conference on Antennas and Propagation*, April 2011, pp. 1071–1075.

Y. Li, C. W. T. Chan, and C. J. Stevens, "Two-Dimensional Capacitor-Connected Grids Metamaterial Waveguide for UWB Contactless Data Transfer Channels," *2013 International Conference on Electromagnetics in Advanced Applications*, Septemeber 2013, pp. 1437–1441.

Y. Li, C. W. T. Chan, and C. J. Stevens, "Capacitor-Connected Grids as One-Dimensional UWB Data Transfer Channels," *7th International Congress on Advanced Electromagnetic Materials in Microwaves and Optics – Metamaterials 2013*, September 2013, pp. 19–21.

Y. Li, C. W. T. Chan, and C. J. Stevens, "Dispersion Characteristics of Two-Dimensional Capacitor-Connected Grids," *7th International Congress on Advanced Electromagnetic Materials in Microwaves and Optics – Metamaterials 2013*, September 2013, pp. 337–339.

Y. Li, C. J. Stevens, C. W. T. Chan, "Waveguide," GB1316011.4 lodged 9 Sept 2013 (Patent).

APPENDIX A

FLOWER ELEMENT GEOMETRY

As shown in Section 4.3.2, each metamaterial "flower" is composed of three components, dubbed the "big" loop, the "small" loop, and the L-shaped plate. These are shown in Figure A.1a, Figure A.1b, and Figure A.1c respectively. Assuming that these components are centred around a coordinate, the element can be composed of the aforementioned components with the appropriate rotation applied to the coordinates specified in Table A.1. The coordinate numbers in Table A.1a–c correspond to the numbered vertices of Figures A.1a–c respectively.

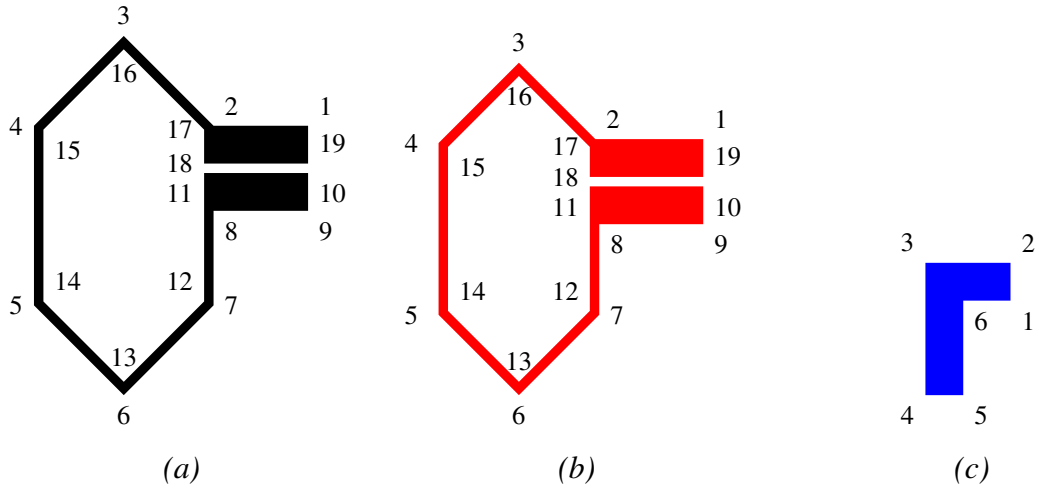


Figure A.1 – The geometry of the bigger loop (a), smaller loop (b), and the L-shaped capacitive plate (c) that make up the elements in Figure 4.54. All components are centred on coordinates of choice, and rotated into their requisite positions.

Coordinate number	**Position** (x, y)
1	$(-0.25, 4.75)$
2	$(-5.25, 4.75)$
3	$(-10, 9.5)$
4	$(-14.75, 4.75)$
5	$(-14.75, -4.75)$
6	$(-10, -9.5)$
7	$(-5.25, -4.75)$
8	$(-5.25, 0.25)$
9	$(-0.25, 0.25)$
10	$(-0.25, 2.25)$
11	$(-5.75, 2.25)$
12	$(-5.75, -4.543)$
13	$(-10, -8.793)$
14	$(-14.25, -4.543)$
15	$(-14.25, 4.543)$
16	$(-10, 8.793)$
17	$(-5.75, 4.543)$
18	$(-5.75, 2.75)$
19	$(-0.25, 2.75)$

(a)

Coordinate number	**Position** (x, y)
1	$(-0.25, 4.75)$
2	$(-5.957, 4.75)$
3	$(-10, 8.793)$
4	$(-14.25, 4.543)$
5	$(-14.25, -4.543)$
6	$(-10, -8.793)$
7	$(-5.75, -4.543)$
8	$(-5.75, 0.25)$
9	$(-0.25, 0.25)$
10	$(-0.25, 2.25)$
11	$(-6.25, 2.25)$
12	$(-6.25, -4.336)$
13	$(-10, -8.086)$
14	$(-13.75, -4.336)$
15	$(-13.75, 4.336)$
16	$(-10, 8.086)$
17	$(-6.25, 4.336)$
18	$(-6.25, 2.75)$
19	$(-0.25, 2.75)$

(b)

Coordinate number	**Position** (x, y)
1	$(-0.25, 0.25)$
2	$(-0.25, 2.25)$
3	$(-4.75, 2.25)$
4	$(-4.75, -4.75)$
5	$(-2.75, -4.75)$
6	$(-2.75, 0.25)$

(c)

Table A.1 – Coordinates of bigger loop (a), coordinates of smaller loop (b), and in coordinates of the Figure A.1. All positions given in millimetres.

BIBLIOGRAPHY

[1] N. Miura, D. Mizoguchi, T. Sakurai, and T. Kuroda, "Analysis and design of inductive coupling and transceiver circuit for inductive inter-chip wireless superconnect," *IEEE Journal of Solid-State Circuits*, vol. 40, no. 4, pp. 829–837, Apr. 2005.

[2] N. Miura, D. Mizoguchi, M. Inoue, K. Niitsu, Y. Nakagawa, M. Tago, M. Fukaishi, T. Sakurai, and T. Kuroda, "A 1Tb/s 3W inductive-coupling transceiver for inter-chip clock and data link," in *2006 IEEE International Conference Digest of Technical Papers Solid-State Circuits*. IEEE, 2006, pp. 1676–1685.

[3] K. Niitsu, Y. Shimazaki, Y. Sugimori, Y. Kohama, K. Kasuga, I. Nonomura, M. Saen, S. Komatsu, K. Osada, N. Irie, T. Hattori, A. Hasegawa, and T. Kuroda, "An inductive-coupling link for 3D integration of a 90nm CMOS processor and a 65nm CMOS SRAM," in *2009 IEEE International Solid-State Circuits Conference - Digest of Technical Papers*. IEEE, Feb. 2009, pp. 480–481,481a.

[4] S. Mick, J. Wilson, and P. Franzon, "4 Gbps high-density AC coupled interconnection," in *Proceedings of the IEEE 2002 Custom Integrated Circuits Conference (Cat. No.02CH37285)*. IEEE, 2002, pp. 133–140.

[5] R. J. Drost, R. D. Hopkins, and I. E. Sutherland, "Proximity communication," *IEEE Journal of Solid-State Circuits*, vol. 39, no. 9, pp. 469–472, Sep. 2004.

[6] K. Kanda, D. D. Antono, K. Ishida, H. Kawaguchi, T. Kuroda, and T. Sakurai, "1.27Gb/s/pin 3mW/pin wireless superconnect (WSC) interface scheme," in *2003 IEEE*

International Solid-State Circuits Conference, 2003. Digest of Technical Papers. ISSCC. IEEE, 2003, pp. 186–487.

[7] R. Canegallo, L. Ciccarelli, F. Natali, A. Fazzi, R. Guerrieri, and P. Rolandi, "3D Contactless communication for IC design," in *2008 IEEE International Conference on Integrated Circuit Design and Technology and Tutorial*. IEEE, Jun. 2008, pp. 241–244.

[8] N. Tesla, "Apparatus for transmitting electrical energy," U.S. Patent 1 119 732, Dec. 1, 1914.

[9] A. Esser and H.-C. Skudelny, "A new approach to power supplies for robots," *IEEE Transactions on Industry Applications*, vol. 27, no. 5, pp. 872–875, 1991.

[10] A. Esser, "Contactless charging and communication for electric vehicles," *IEEE Industry Applications Magazine*, vol. 1, no. 6, pp. 4–11, 1995.

[11] J. M. Fernandez and J. A. Borras, "Contactless battery charger with wireless control link," U.S. Patent 6 184 651, Feb. 6, 2001.

[12] G. Scheible, B. Smailus, M. Klaus, K. Garrels, and L. Heinemann, "System for wirelessly supplying a large number of actuators of a machine with electrical power," U.S. Patent 6 597 076, Jul. 22, 2003.

[13] L. Ka-Lai, J. Westwood, and P. G. W. Beart, "Contact-less power transfer," U.S. Patent 7 042 196, May 9, 2006.

[14] T. A. Vanderelli, J. G. Shearer, and J. R. Shearer, "Method and apparatus for a wireless power supply," U.S. Patent 7 027 311, Apr. 11, 2006.

[15] Y. Yuan, Y. Yoshida, and T. Kuroda, "Non-contact 10% efficient 36mW power delivery using on-chip inductor in 0.18-μm CMOS," in *2007 IEEE Asian Solid-State Circuits Conference*. IEEE, Nov. 2007, pp. 115–118.

[16] A. Kurs, A. Karalis, R. Moffatt, J. D. Joannopoulos, P. Fisher, and M. Soljačić, "Wireless power transfer via strongly coupled magnetic resonances." *Science (New York, N.Y.)*, vol. 317, no. 5834, pp. 83–6, Jul. 2007.

[17] A. Karalis, J. D. Joannopoulos, and M. Soljačić, "Efficient wireless non-radiative mid-range energy transfer," *Annals of Physics*, vol. 323, no. 1, pp. 34–48, Jan. 2008.

[18] A. Esser and A. Nagel, "Contactless high speed signal transmission integrated in a compact rotatable power transformer," *Power Electronics and Applications, 1993., Fifth European Conference on*, pp. 409–414, 1993.

[19] A. Kawamura, K. Ishioka, and J. Hirai, "Wireless transmission of power and information through one high-frequency resonant AC link inverter for robot manipulator applications," *IEEE Transactions on Industry Applications*, vol. 32, no. 3, pp. 503–508, 1996.

[20] J. Hirai, T.-W. Kim, and A. Kawamura, "Wireless transmission of power and information and information for cableless linear motor drive," *IEEE Transactions on Power Electronics*, vol. 15, no. 1, pp. 21–27, Jan. 2000.

[21] C. J. Stevens, C. W. T. Chan, K. Stamatis, and D. J. Edwards, "Magnetic metamaterials as 1-D data transfer channels: An application for magneto-inductive waves," *IEEE Transactions on Microwave Theory and Techniques*, vol. 58, no. 5, pp. 1248–1256, May 2010.

[22] E. Shamonina, V. A. Kalinin, K. H. Ringhofer, and L. Solymar, "Magneto-inductive waveguide," *Electronics Letters*, vol. 38, no. 8, pp. 371–372, Apr. 2002.

[23] G. V. Eleftheriades and K. G. Balmain, *Negative-Refraction Metamaterials: Fundamental Principles and Applications*, G. V. Eleftheriades and K. G. Balmain, Eds. Hoboken, NJ: John Wiley, 2005.

[24] R. Cardu, M. Scandiuzzo, S. Cani, L. Perugini, E. Franchi, R. Canegallo, and R. Guerrieri, "Chip-to-chip communication based on capacitive coupling," in *2009 IEEE International Conference on 3D System Integration*. IEEE, Sep. 2009, pp. 1–6.

[25] K. Onizuka, H. Kawaguchi, M. Takamiya, T. Kuroda, and T. Sakurai, "Chip-to-chip inductive wireless power transmission system for SiP applications," in *IEEE Custom Integrated Circuits Conference 2006*. IEEE, Sep. 2006, pp. 575–578.

[26] Y. Li, C. W. T. Chan, and C. J. Stevens, "Dispersion characteristics of two-dimensional capacitor-connected grids," in *2013 7th International Congress on Advanced Electromagnetic Materials in Microwaves and Optics*. IEEE, Sep. 2013, pp. 337–339.

[27] ——, "Capacitor-connected grids as one-dimensional UWB data transfer channels," in *2013 7th International Congress on Advanced Electromagnetic Materials in Microwaves and Optics*. IEEE, Sep. 2013, pp. 19–21.

[28] ——, "Two-dimensional capacitor-connected grids metamaterial waveguide for UWB contactless data transfer channels," in *2013 International Conference on Electromagnetics in Advanced Applications (ICEAA)*. IEEE, Sep. 2013, pp. 1437–1441.

[29] J. Landt, "Shrouds of time—the history of RFID," *RFID Connections*, no. 2, 2002.

[30] H. Stockman, "Communication by means of reflected power," *Proceedings of the IRE*, vol. 36, no. 10, pp. 1196–1204, Oct. 1948.

[31] K. Finkenzeller, *RFID handbook: Radio-frequency fundamentals and applications*. Chichester: John Wiley, 1999.

[32] M. C. K. Wiltshire, J. B. Pendry, I. R. Young, D. J. Larkman, D. J. Gilderdale, and J. V. Hajnal, "Microstructured magnetic materials for RF flux guides in magnetic resonance imaging." *Science (New York, N.Y.)*, vol. 291, no. 5505, pp. 849–851, Feb. 2001.

[33] A. A. Radkovskaya, M. Shamonin, C. J. Stevens, G. Faulkner, D. J. Edwards, E. Shamonina, and L. Solymar, "Resonant frequencies of a combination of split rings: Experimental, analytical and numerical study," *Microwave and Optical Technology Letters*, vol. 46, no. 5, pp. 473–476, Sep. 2005.

[34] W. N. Hardy and L. A. Whitehead, "Split-ring resonator for use in magnetic resonance from 200–2000 MHz," *Review of Scientific Instruments*, vol. 52, no. 2, p. 213, Feb. 1981.

[35] W. Froncisz and J. S. Hyde, "The loop-gap resonator: a new microwave lumped circuit ESR sample structure," *Journal of Magnetic Resonance (1969)*, vol. 47, no. 3, pp. 515–521, May 1982.

[36] S. O'Brien and J. B. Pendry, "Magnetic activity at infrared frequencies in structured metallic photonic crystals," *Journal of Physics: Condensed Matter*, vol. 14, no. 25, pp. 6383–6394, Jul. 2002.

[37] M. Shamonin, E. Shamonina, V. A. Kalinin, and L. Solymar, "Properties of a metamaterial element: Analytical solutions and numerical simulations for a singly split double ring," *Journal of Applied Physics*, vol. 95, no. 7, pp. 3778–3784, 2004.

[38] E. Shamonina, V. A. Kalinin, K. H. Ringhofer, and L. Solymar, "Magnetoinductive waves in one, two, and three dimensions," *Journal of Applied Physics*, vol. 92, no. 10, pp. 6252–6261, Nov. 2002.

[39] O. Sydoruk, "Tailoring the properties of metamaterials for linear and nonlinear applications," Ph.D. dissertation, Universität Osnabrück, 2007.

[40] R. R. A. Syms, L. Solymar, and E. Shamonina, "Absorbing terminations for magneto-inductive waveguides," *IEE Proceedings - Microwaves, Antennas and Propagation*, vol. 152, no. 2, p. 77, 2005.

[41] M. C. K. Wiltshire, E. Shamonina, I. R. Young, and L. Solymar, "Dispersion characteristics of magneto-inductive waves: comparison between theory and experiment," *Electronics Letters*, vol. 39, no. 2, pp. 215–217, Jan. 2003.

[42] R. R. A. Syms, O. Sydoruk, E. Shamonina, and L. Solymar, "Higher order interactions in magneto-inductive waveguides," *Metamaterials*, vol. 1, no. 1, pp. 44–51, Mar. 2007.

[43] M. Eleftheriou, N. Lazarides, and G. P. Tsironis, "Magnetoinductive breathers in metamaterials," *Physical Review E*, vol. 77, no. 3, p. 036608, Mar. 2008.

[44] R. R. A. Syms, E. Shamonina, and L. Solymar, "Positive and negative refraction of magnetoinductive waves in two dimensions," *The European Physical Journal B*, vol. 46, no. 2, pp. 301–308, Aug. 2005.

[45] O. Sydoruk, O. Zhuromskyy, E. Shamonina, and L. Solymar, "Phonon-like dispersion

curves of magnetoinductive waves," *Applied Physics Letters*, vol. 87, no. 7, p. 072501, Aug. 2005.

[46] A. A. Radkovskaya, O. Sydoruk, M. Shamonin, E. Shamonina, C. J. Stevens, G. Faulkner, D. J. Edwards, and L. Solymar, "Experimental study of a bi-periodic magnetoinductive waveguide: comparison with theory," *IET Microwaves, Antennas & Propagation*, vol. 1, no. 1, pp. 80–83, Feb. 2007.

[47] O. Sydoruk, A. A. Radkovskaya, O. Zhuromskyy, E. Shamonina, M. Shamonin, C. J. Stevens, G. Faulkner, D. J. Edwards, and L. Solymar, "Tailoring the near-field guiding properties of magnetic metamaterials with two resonant elements per unit cell," *Physical Review B*, vol. 73, no. 22, p. 224406, Jun. 2006.

[48] A. A. Radkovskaya, O. Sydoruk, M. Shamonin, C. J. Stevens, G. Faulkner, D. J. Edwards, E. Shamonina, and L. Solymar, "Transmission properties of two shifted magnetoinductive waveguides," *Microwave and Optical Technology Letters*, vol. 49, no. 5, pp. 1054–1058, May 2007.

[49] O. Sydoruk, M. Shamonin, A. A. Radkovskaya, O. Zhuromskyy, E. Shamonina, R. Trautner, C. J. Stevens, G. Faulkner, D. J. Edwards, and L. Solymar, "Mechanism of subwavelength imaging with bilayered magnetic metamaterials: Theory and experiment," *Journal of Applied Physics*, vol. 101, no. 7, p. 073903, 2007.

[50] R. R. A. Syms, L. Solymar, I. R. Young, and T. Floume, "Thin-film magneto-inductive cables," *Journal of Physics D: Applied Physics*, vol. 43, no. 5, p. 055102, Feb. 2010.

[51] K. Stamatis, "Short range communication system using metamaterials," University of Oxford, Oxford, PRS Transfer Report, 2009.

[52] R. R. A. Syms, L. Solymar, and I. R. Young, "Broadband coupling transducers for magneto-inductive cables," *Journal of Physics D: Applied Physics*, vol. 43, no. 28, p. 285003, Jul. 2010.

[53] O. Sydoruk, "Coupling transducers for magnetoinductive waveguides: Minimising reflection over the whole pass band," *Metamaterials*, vol. 5, no. 1, pp. 42–48, Apr. 2011.

[54] A. A. Radkovskaya, M. Shamonin, C. J. Stevens, G. Faulkner, D. J. Edwards, E. Shamonina, and L. Solymar, "An experimental study of the properties of magnetoinductive waves in the presence of retardation," *Journal of Magnetism and Magnetic Materials*, vol. 300, no. 1, pp. 29–32, May 2006.

[55] P. Lorrain, D. R. Corson, and F. Lorrain, *Electromagnetic Fields and Waves*, 3rd ed. New York: Freeman, 1988.

[56] E. Tatartschuk, N. Gneiding, F. Hesmer, A. Radkovskaya, and E. Shamonina, "Mapping inter-element coupling in metamaterials: Scaling down to infrared," *Journal of Applied Physics*, vol. 111, no. 9, p. 094904, May 2012.

[57] V. Lomanets, O. Zhuromskyy, G. Onishchukov, O. Sydoruk, E. Tatartschuk, E. Shamonina, G. Leuchs, and U. Peschel, "Interacting waves on chains of split-ring resonators in the presence of retardation," *Applied Physics Letters*, vol. 97, no. 1, p. 011108, Jul. 2010.

[58] P. J. Petersan and S. M. Anlage, "Measurement of resonant frequency and quality factor of microwave resonators: Comparison of methods," *Journal of Applied Physics*, vol. 84, no. 6, p. 3392, Sep. 1998.

[59] J. Zhu, "Design and Application of Novel Metamaterial Elements and Configurations," Doctorate Thesis, University of Oxford, 2011.

[60] Z. Ma, "RF properties of high temperature superconducting materials," Ph. D., Stanford University, 1995.

[61] M. Kamon, M. Ttsuk, and J. White, "FASTHENRY: A multipole-accelerated 3-D inductance extraction program," *IEEE Transactions on Microwave Theory and Techniques*, vol. 42, no. 9, pp. 1750–1758, 1994.

[62] R. R. A. Syms, I. R. Young, and L. Solymar, "Low-loss magneto-inductive waveguides," *Journal of Physics D: Applied Physics*, vol. 39, no. 18, pp. 3945–3951, Sep. 2006.

[63] M. J. Freire, R. Marqués, F. Medina, M. A. G. Laso, and F. Martín, "Planar magnetoinductive wave transducers: Theory and applications," *Applied Physics Letters*, vol. 85, no. 19, p. 4439, Nov. 2004.

[64] M. C. K. Wiltshire, E. Shamonina, I. R. Young, and L. Solymar, "Experimental and theoretical study of magneto-inductive waves supported by one-dimensional arrays of "swiss rolls"," *Journal of Applied Physics*, vol. 95, no. 8, pp. 4488–4493, 2004.

[65] C. W. T. Chan, "Near field contactless connectors using metamaterial systems," University of Oxford, Oxford, 4^{th} Year Report, 2009.

[66] D.-W. Duan, B. Rubin, and J. Magerlein, "Distributed effects of a gap in power/ground planes," in *IEEE 8th Topical Meeting on Electrical Performance of Electronic Packaging (Cat. No.99TH8412)*. IEEE, 1999, pp. 207–210.